공학박사 학위논문

Study on Supramolecular Chirality of Organic Semiconductors and Its Optoelectronic Applications

유기반도체의 초분자 키랄성 및 광전자적 응용 연구

2023 년 2 월

서울대학교 대학원

화학생물공학부

안재용

Study on Supramolecular Chirality of Organic Semiconductors and Its Optoelectronic Applications

지도 교수 오 준 학

이 논문을 공학박사 학위논문으로 제출함
2023 년 1 월

서울대학교 대학원
화학생물공학부
안 재 용

안재용의 공학박사 학위논문을 인준함
2023 년 1 월

위 원 장 _____ 이 종 찬 _____ (인)

부위원장 _____ 오 준 학 _____ (인)

위 원 _____ 유 동 원 _____ (인)

위 원 _____ 김 소 연 _____ (인)

위 원 _____ 박 종 혁 _____ (인)

Abstract

Circularly polarized light has chirality according to the direction of rotation of the vector of electromagnetic waves. It has received great attention because it can be used in various fields such as three-dimensional display, polarization imaging, encrypted optical communication, and quantum computation. In order to emit or detect the circularly polarized light conventionally, various optics such as linear polarizer quarter-wave plate have been used which reduces the performance of the device and have great limitations in terms of miniaturization and process simplification. For these reasons, studies have been conducted on the devices that can directly detect or emit circularly polarized light, which are based on organic materials that have advantages such as tunability, lightness, process simplification, and flexibility. However, research on organic-based chiral optoelectronics is still in its infancy, and most of the studies reported so far have difficulties in low performance. The supramolecular chirality represents the range of chirality beyond the molecular level, which exhibits amplified chirality through self-assembly and alignment. In order to solve the preceding problems, this paper focuses on the study of the supramolecular chirality of organic semiconductors and its optoelectronic applications.

In **Chapter 1**, I briefly introduced the research background, and the purpose of this paper, including basic information on organic electronics, supramolecular chirality, and chiral optoelectronics.

In **Chapter 2**, novel bay-substituted chiral perylene diimides (PDIs) were synthesized and self-assembled into one-dimensional nanowires. Through the circular dichroism spectrum analysis of the prepared nanowires, it was confirmed that the substitution in the bay position is an effective way to control the supramolecular chirality. In addition, the performance of optoelectronic devices according to the bay substitution effect was investigated by fabrication of

phototransistors based on nanowires. At this time, the CN-substituted nanowires exhibited the best performance, which is in agreement with the crystal structure analysis and computational calculation results. The improvement of electron injectability and π-overlapping area increased the optoelectronic performances.

In **Chapter 3**, novel chiral PDIs and insulating polymer polylactic acid (PLA) were blended and used as the active layer of an organic field-effect transistor-based photodetector. At this time, it was confirmed that the amplified supramolecular chirality appeared in the thin film in which the polymer was blended. In addition, by comparing the performance of optoelectronic devices according to the blending ratio between chiral PDIs and PLA in the fabricated photodetectors, I confirmed that the charge trap effect induced from the existence of PLA enhanced photo-sensing performance of the devices. In addition, the effect of chirality on the optoelectronic performance was analyzed through the comparison in the case of using racemate and enantiomer of chiral PDIs.

In **Chapter 4**, based on the previous research, a simple yet powerful method to fabricate chiroptical flexible layers via supramolecular helical ordering of conjugated polymer chains using transient chiral templating by volatile enantiomers was presented. Through the analysis of the structure, morphology, composition, and functional group of the active layer, it was confirmed that the chiral dopant sublimes under thermal annealing, resulting in exciton coupling of chromophores in the formed helical structure. In addition, diode-based circularly polarized light detectors were fabricated based on the chiroptical active layer, and excellent optoelectronic properties were reported along with remarkable g factor of 1.2 through the optimization of the device structure and study of the charge transport mechanisms. By analyzing the optical activities of the active layers and fabricated devices, it was confirmed that the axial direction of polarization and the incident angle of the beam did not affect to the performance of the devices. Therefore, these devices are capable to detect the degree of circular polarization and highly promising in optical

communication. Finally, prototypes of circularly polarized light based optical communication and imaging were fabricated and investigated by array based devices.

Keyword : semiconductor, organic electronics, supramolecular chirality, circularly polarized light, photodetector

Student Number : 2019-30718

Table of Contents

List of Figure and Tables

Chapter 1

Introduction and Motivation

1.1. Study Background

1.1.1. Organic Electronics

Organic compounds, which contain bonds between carbons in their chemical structure, are of central importance due to the carbon's ability to bond with each other and the characteristics granted from it. They form the basis of all living things, with infinite possibilities to be. Among them, organic semiconductors (OSCs), which can be used as the active layer in diverse electronic devices have drawn great attention due to their unique features such as tunability, intense optical absorption and emission, solution processability, lightweightness, mechanical flexibility, and stretchability.[1] Since the discovery of conductive polyacetylene in 1977, intensive researches in both industry and academia achieved tremendous progress in this field.[2] It is no doubt that significant improvement in performance has been driven comparable to existing platform (e.g. silicon), however, there still remain a lot of challenges to pioneer a new generation with respect to problems such as stability, cost effectiveness, and difficultness in process.[3]

Organic light-emitting diodes (OLEDs), organic field-effect transistors (OFETs), organic photovoltaics (OPVs), and organic photodetectors (OPDs) are the key devices in organic electronics. OLEDs, which emit the light in response to electric current through radiative recombination of electron and hole between two electrodes, are the most advanced devices which reached to a commercialized level mainly used in smart phone and TV displays.[4-5] OFETs, featured by current regulation through a third gate electrode separated from the channel, are the essential building blocks to realize the future flexible and stretchable electronics. OPVs utilizing photovoltaic effect which generates voltage upon exposure to light, are making the first steps into markets, but still suffered from their relatively low power conversion efficiencies and short lifetime.[5-6] Organic semiconductors have great potential in light sensing applications due to their tunable spectral sensitivity from ultra-violet to infrared region and intense optical absorption. Therefore, OPDs can be diversely applied to

optical communications, environmental monitoring, biomedical imaging, and sensing, overcoming the intrinsic demerits of brittleness and complicated manufacturing process of inorganic photodetectors.[7]

Various strategies have been investigated to improve OPDs through different structures. Generally, OPDs can be categorized into photoconductors-based OPDs, photodiodes-based OPDs, and phototransistors-based OPDs (**Figure 1.1**). In photoconductors-based OPDs, two electrodes are located horizontally on the opposite ends of the active layer by Ohmic contact. Major charge carriers recirculate the device many times before recombination, while minor charge carriers trapped in the active layer. In case of photodiodes-based OPDs, incident photons generate electron-hole pairs through photoelectric effect and they diffuse to the cathode and anode with the help of transporting layer, respectively. Phototransistors-based OPDs have an ability to adjust the channel resistance by applying gate voltage, which resulted in high photocurrent and high responsivity.

In order to investigate the performance for OPDs, photoresponsivity (R) and photosensitivity (P) were calculated from transfer curves in case of transistors, and current-voltage curves in case of diodes, coupled with light illumination. The R and P values are typically defined by the following equations:

$$R = \frac{I_{\mathrm{ph}}}{P_{\mathrm{inc}}} = \frac{I_{\mathrm{light}} - I_{\mathrm{dark}}}{P_{\mathrm{inc}}} \tag{1}$$

$$P = \frac{I_{\mathrm{light}} - I_{\mathrm{dark}}}{I_{\mathrm{dark}}} \tag{2}$$

where I_{ph} is the photocurrent, P_{inc} the incident illumination power, I_{light} the drain current under illumination, and I_{dark} the drain current in the dark condition, respectively. In addition, the external quantum efficiency (EQE) (η) of OPTs which can be defined as the ratio of number of photogenerated carriers to the number of photons incident onto the OPT channel area, was calculated using the following equation:

$$\eta = \frac{(I_{light} - I_{dark})hc}{eP_{int}A\lambda_{peak}} \tag{3}$$

where h is the plank constant, c the speed of light, e the fundamental unit of charge, P_{int} the incident light intensity (i.e., the incident optical power density), A the area of the OPD channel, and λ_{peak} the peak wavelength of the incident light, respectively. Detectivity usually describes the minimum detectable signal, which allows comparisons of photodetector devices with different configurations and areas. The specific detectivity (D^*) can be thought of as the the signal to noise ratio generated by a photodetector with an active area (A) of 1 cm^2 at 1 W of incident power when the electrical bandwidth (Δf) is 1 Hz: D^* was evaluated in this study using the following equations:

$$D^* = \frac{\sqrt{A}}{NEP} \tag{4}$$

$$NEP = \frac{I_n}{R\sqrt{\Delta f}} \tag{5}$$

In these equations, NEP the noise equivalent power, I_n the measured noise current, and Δf the bandwidth. If the major limit to detectivity is shot noise from the drain current under dark condition, D^* can be simplified as:

$$D^* = \frac{R}{\sqrt{(2e \cdot I_{dark}/A)}} \tag{6}$$

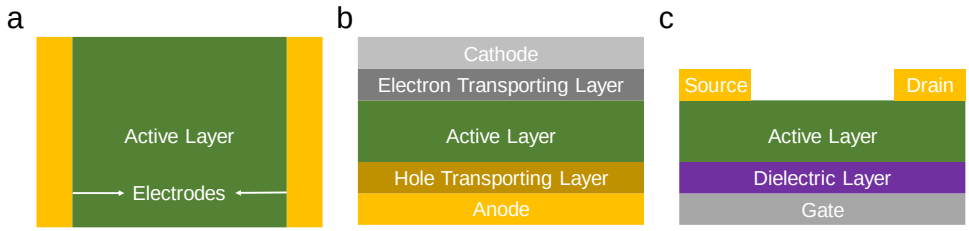

Figure 1.1. Device configurations of various organic photodetectors. a–c, Device structures of photoconductor (**a**), photodiode (**b**), and phototransistor (**c**).

1.1.2. Supramolecular Chirality

Chirality is one of the fundamental characteristics of living matter and nature, which represents the asymmetry that cannot be superimposed to mirror image. It is universal and can be observed at various hierarchical levels from subatomic to galactic scales.[8] Therefore, study on chirality is of great importance to understand from parity conversion in neutrinos to our galaxy system including chemical synthesis, catalysis, pharmaceutics, and fundamental physics.[9-10] At a molecular level, there are several series of chirality. If there is a chiral carbon which is a sp^3 carbon atom that four different types of atoms or groups attached, (i.e. if stereocenter exists), the chirality in the molecules is termed point chirality. There are two other types of chirality which termed axial chirality and planar chirality, if stereogenic axis and stereogenic plane give rise to chirality, respectively. Helicity, as a special form of axial chirality, obtain chirality from the inherent curvature of a molecule, which is very common in the supramolecular systems.

The *R*/*S* system is the most general nomenclature system to distinguish enantiomers. Each chiral center can be labeled *R* (right-handed) or *S*(left-handed) depending on the sequence how its substituents are assigned according to the Cahn-Ingold-prelog priority rules. Since chiral molecules interact with light, substance that can rotate plan-polarized light clockwise are said to be dextrorotatory, and levorotatory for the anticlockwise rotation. The *P/M* chirality generally refers to a supramolecular system or the axial or planar molecular chirality. The system has *P* helicity if the rotation is clockwise viewing from either end of a molecule, and has *M* helicity, vice versa.

Supramolecular chirality is the chirality beyond the molecular scales generated by intermolecular noncovalent interactions. Among the various levels of chirality, it is of vital importance since it is strongly related to chemistry, physics, biology, materials, and nano-science which handle the scales from atomic to supramolecular.[8, 11] Self-assembly, defined as the autonomous organization of components into

patterns or structures without human intervention, is one of the powerful methods to originate supramolecular structures.[12-13] Chirality can be transferred from single molecules via various noncovalent interactions to form supramolecular chirality. Hydrogen bonding and π–π stacking interactions are often play key role in self-assembly of molecules.[14] The strength and distance of both interactions are quite similar, and directionality exists in each types of interactions, respectively.[15]

Amplification of chirality is well-known phenomenon in supramolecular systems. Green and co-workers defined two effects that influence the amplification of chirality named "sergeants-and-soldiers" principle and the "majority-rules".[16] "Sergeants-and-soldiers" principle stands for the situations where a small initial chiral component induces a high degree of chirality in the whole system by the control of the movements of large numbers of cooperative achiral units.[17] On the other hand, "majority-rules" implies a slight enantiomeric excess of one enantiomer dictates the overall system. The key challenges in both rules are how small can the amount of chiral sergeant molecules or bias control the entire system.[18]

1.1.3. Chiral Optoelectronics

Chirality can be applied to the optoelectronics, with respect to the devices that can detect or emit the circularly polarized light (CPL), which consists of two perpendicular electromagnetic plane waves of equal amplitude and 90° difference that cannot be overlapped. Due to its rich optical information and lack of angle dependence, CPL is central to many photonic technologies, such as spin optical communication, circular dichroism spectroscopy, magnetic recording, and quantum computation.[19-23] Since inorganic semiconductors (e.g. silicon and III–V semiconductors) do not have intrinsic chirality, multiple optical elements and complex processing methods were needed to realize CPL emission and detection which hinder to achieve the miniaturization, integration, and high performance.[24] Therefore, the development of devices capable of directly detecting or emitting CPL has been an innovative target for future generation optoelectronics.

To quantify the interactions of chiral sample with left and right CPL beams, circular dichroism (CD) is defined as the difference between absorption of opposite CPL beams by following equation:[20]

$$CD = A^L - A^R \tag{7}$$

where A^L and A^R are the absorptions of each CPL handedness. For historical reasons, the output of CD instruments is generally measured as ellipticity in millidegree as follows,[20]

$$\theta = 32980\ \ CD \tag{8}$$

However, since the CD value only compares between the difference between the absorbance depending on CPL handedness, direct comparison between the samples under different condition is difficult. Therefore, a quantity that independent of the concentration and of the pathlength was derived, named as anisotropy or dissymmetry factor *g*, by following equation:

$$g_{abs} = \frac{A^L - A^R}{A} \tag{9}$$

where A represents the conventional absorbance of non-polarized light. In the field related to chiral optoelectronics, the figure of merits is shown in analogy to g_{abs}, as follows,

$$g_{EL} = 2\frac{I^L - I^R}{I^L + I^R} \tag{10}$$

where I^L and I^R intensity of emitted left-handed CPL (LCPL) and right-handed CPL (RCPL) respectively, in CPL emitting devices. Similarly, in CPL photodetectors, it is defined as

$$g_{ph} = 2\frac{{I_{Ph}}^L - {I_{Ph}}^R}{{I_{Ph}}^L + {I_{Ph}}^R} \tag{11}$$

where ${I_{Ph}}^L$ and ${I_{Ph}}^R$ are measured photocurrent under LCPL and RCPL illumination, respectively.

Chiral organic molecules provide an opportunity to emit or detect CPL intrinsically, without additional optics and complex process. However, chirality originated from the chiral molecule itself is mostly not enough to detect or emit the CPL efficiently. Therefore, organic chiral supramolecules are promising candidates of building blocks in chiral optoelectronics due to their amplified supramolecular chirality. In addition, they have advantages such as high solubility, and tunable self-assembly and optical bandgap. Recently, study about self-assembled perylene diimides used in CPL sensing was reported and demonstrated the feasibility of supramolecular chirality for high-performance chiroptical sensing.[25]

1.2. Purpose of Research

Although study about chiral optoelectronics is emerging research field for their fascinating applicability in future technologies, there are only few studies on chiral optoelectronics based on chiral supramolecules. Investigation about supramolecular chirality of organic semiconductors and its optoelectronic applications are still in its infancy. Many things remain unknown, such as how molecular chirality is transferred to supramolecular chirality, which factors affect the degree of amplification in chirality, and methods efficient to amplify supramolecular chirality.

In this study, I mainly set a research goal as contribute to resolve these vulnerabilities. The purpose of this study is to find the effective strategies to utilize supramolecular chirality on chiral optoelectronics. I investigated the supramolecular chirality *via* molecular design of chiral organic semiconductors and their self-assembly to single crystals. In addition, I conducted a research about how chirality affects to the performance of electronic devices and how blending system affects to the supramolecular chirality. Finally, I presented an effective strategy to obtain outstanding chiroptical properties in supramolecular systems and thoroughly studied their mechanism and applications.

1.3. References

(1) Fahlman, M.; Fabiano, S.; Gueskine, V.; Simon, D.; Berggren, M.; Crispin, X. Interfaces in Organic Electronics. *Nature Reviews Materials* **2019,** *4*, 627-650.

(2) Shirakawa, H.; Louis, E. J.; MacDiarmid, A. G.; Chiang, C. K.; Heeger, A. J. Synthesis of Electrically Conducting Organic Polymers: Halogen Derivatives of Polyacetylene, (Ch). *J. Chem. Soc., Chem. Commun.* **1977**, 578-580.

(3) Dong, H.; Fu, X.; Liu, J.; Wang, Z.; Hu, W. 25th Anniversary Article: Key Points for High-Mobility Organic Field-Effect Transistors. *Adv. Mater.* **2013,** *25*, 6158-6183.

(4) Zou, S.-J.; Shen, Y.; Xie, F.-M.; Chen, J.-D.; Li, Y.-Q.; Tang, J.-X. Recent Advances in Organic Light-Emitting Diodes: Toward Smart Lighting and Displays. *Mater. Chem. Front.* **2020,** *4*, 788-820.

(5) Lüssem, B.; Keum, C.-M.; Kasemann, D.; Naab, B.; Bao, Z.; Leo, K. Doped Organic Transistors. *Chem. Rev.* **2016,** *116*, 13714-13751.

(6) Chen, L. X. Organic Solar Cells: Recent Progress and Challenges. *ACS Energy Letters* **2019,** *4*, 2537-2539.

(7) Ren, H.; Chen, J.-D.; Li, Y.-Q.; Tang, J.-X. Recent Progress in Organic Photodetectors and Their Applications. *Adv. Sci.* **2021,** *8*, 2002418.

(8) Liu, M.; Zhang, L.; Wang, T. Supramolecular Chirality in Self-Assembled Systems. *Chem. Rev.* **2015,** *115*, 7304-7397.

(9) Bouchiat, M.-A.; Bouchiat, C. Parity Violation in Atoms. *Rep. Prog. Phys.* **1997,** *60*, 1351.

(10) Hembury, G. A.; Borovkov, V. V.; Inoue, Y. Chirality-Sensing Supramolecular Systems. *Chem. Rev.* **2008,** *108*, 1-73.

(11) Bai, C.; Liu, M. From Chemistry to Nanoscience: Not Just a Matter of Size. *Angew. Chem. Int. Ed.* **2013,** *52*, 2678-2683.

(12) Yang, Y.; Zhang, Y.; Wei, Z. Supramolecular Helices: Chirality Transfer from Conjugated Molecules to Structures. *Adv. Mater.* **2013,** *25*, 6039-6049.

(13) Whitesides, G. M.; Boncheva, M. Beyond Molecules: Self-Assembly of Mesoscopic and Macroscopic Components. *Proc. Natl. Acad. Sci. USA* **2002,** *99*, 4769-4774.

(14) Hoeben, F. J. M.; Jonkheijm, P.; Meijer, E. W.; Schenning, A. P. H. J. About Supramolecular Assemblies of Π-Conjugated Systems. *Chem. Rev.* **2005,** *105*, 1491-1546.

(15) Yan, Y.; Wang, R.; Qiu, X.; Wei, Z. Hexagonal Superlattice of Chiral Conducting Polymers Self-Assembled by Mimicking B-Sheet Proteins with Anisotropic Electrical Transport. *J. Am. Chem. Soc.* **2010,** *132*, 12006-12012.

(16) Lifson, S.; Green, M. M.; Andreola, C.; Peterson, N. C. Macromolecular Stereochemistry: Helical Sense Preference in Optically Active Polyisocyanates. Amplification of a Conformational Equilibrium Deuterium Isotope Effect. *J. Am. Chem. Soc.* **1989,** *111*, 8850-8858.

(17) Prins, L. J.; Timmerman, P.; Reinhoudt, D. N. Amplification of Chirality: The "Sergeants and Soldiers" Principle Applied to Dynamic Hydrogen-Bonded Assemblies. *J. Am. Chem. Soc.* **2001,** *123*, 10153-10163.

(18) Shang, X.; Song, I.; Han, M.; Lee, J. H.; Ohtsu, H.; Choi, W.; Kim, J. C.; Ahn, J.; Kwak, S. K.; Oh, J. H. "Majority-Rules" Effect on Supramolecular Chirality and Optoelectronic Properties of Chiral Tetrachloro-Perylene Diimides. *Adv. Opt. Mater.* **2021,** *9*, 2001911.

(19) Farshchi, R.; Ramsteiner, M.; Herfort, J.; Tahraoui, A.; Grahn, H. T. Optical Communication of Spin Information between Light Emitting Diodes. *Appl. Phys. Lett.* **2011,** *98*, 162508.

(20) Berova, N.; Bari, L. D.; Pescitelli, G. Application of Electronic Circular Dichroism in Configurational and Conformational Analysis of Organic Compounds. *Chem. Soc. Rev.* **2007,** *36*, 914-931.

(21) Stanciu, C. D.; Hansteen, F.; Kimel, A. V.; Kirilyuk, A.; Tsukamoto, A.; Itoh, A.; Rasing, T. All-Optical Magnetic Recording with Circularly Polarized Light. *Phys. Rev. Lett.* **2007,** *99*, 047601.

(22) Togan, E.; Chu, Y.; Trifonov, A. S.; Jiang, L.; Maze, J.; Childress, L.; Dutt, M. V. G.; Sørensen, A. S.; Hemmer, P. R.; Zibrov, A. S.; Lukin, M. D. Quantum Entanglement between an Optical Photon and a Solid-State Spin Qubit. *Nature* **2010,** *466*, 730.

(23) Wagenknecht, C.; Li, C.-M.; Reingruber, A.; Bao, X.-H.; Goebel, A.; Chen, Y.-A.; Zhang, Q.; Chen, K.; Pan, J.-W. Experimental Demonstration of a Heralded Entanglement Source. *Nat. Photon.* **2010,** *4*, 549.

(24) Zhang, C.; Wang, X.; Qiu, L. Circularly Polarized Photodetectors Based on Chiral Materials: A Review. *Frontiers in Chemistry* **2021,** *9*.

(25) Shang, X.; Song, I.; Ohtsu, H.; Lee, Y. H.; Zhao, T.; Kojima, T.; Jung, J. H.; Kawano, M.; Oh, J. H. Supramolecular Nanostructures of Chiral Perylene Diimides with Amplified Chirality for High-Performance Chiroptical Sensing. *Adv. Mater.* **2017,** *29*, 1605828.

Chapter 2

Studies on Bay-Substitution Effect of Self-Assembled Nanostructures on Supramolecular Chirality and Optoelectronic Properties

2.1. Introduction

Chirality is ubiquitous in nature and can be observed in single molecules to entire galaxies. Among the hierarchical levels of chirality, supramolecular chirality has attracted a great deal of attention in the field of optoelectronics.[1-4] In particular, one-dimensional (1D) single-crystalline organic nanomaterials, which exhibit small physical dimensions, large surface area, and a defect-free nature, can be used to fabricate high-performance, miniaturized electronic, and optoelectronic devices.[5, 6] Introducing chirality into such nanostructures can potentially lead to more advanced applications.[7] However, applications involving chiral nanostructures, particularly those that incorporate chiral organic nanomaterials into optoelectronic devices, are in their infancy.[1, 8, 9]

OFETs are widely used in large-area, flexible, low-cost, and printable electronic devices. Organic phototransistors (OPTs) are organic transistors in which incident light intensity modulates charge-carrier density in the conduction channel. The light-detection sensitivity of OPTs can be controlled as a means of manipulating photo-signals.[10] Single-crystalline nanowires (NWs), particularly based on *n*-channel materials, have not been frequently used in OPTs, although they are useful for implementing complementary logic circuits. The performance of *n*-channel systems lags behind that of their *p*-type counterparts.[1, 9, 11, 12] However, OPTs-based on single-crystalline NWs may yield very high light sensitivity due to lack of grain boundaries. In addition, their nature of structural perfection will allow a deeper understanding of the fundamental mechanisms of charge generation and separation in the devices.[13]

PDIs exhibit high thermal stability and photostability under ambient conditions, and have been studied extensively for use in organic optoelectronic devices such as organic solar cell and OFETs.[14-20] Although PDI-based supramolecular nanomaterials have been incorporated into OPTs,[10, 13] research on chiral PDI molecules in OPTs is rare and most chiral PDI-based materials only focus on *N*-substituted groups at the imide position.[1, 8] Structural modification through the bay

position can be used to tune solubility and the electronic and optical properties of PDIs.[21] However, relatively few reports describe the self-assembly of bay-substituted PDIs into well-defined 1D nanomaterials, especially chiral bay-substituted PDIs. In addition, bay-substituted PDIs are very sensitive to solvent effects. Therefore, precise molecular design and suitable solvents are required to achieve desired morphologies with bay-substituted PDIs.[2]

Herein, I describe the self-assembly into 1D nanomaterials of various bay-substituted PDIs such as (*R*)-2F-CPDI-Ph, (*R*)-2Br-CPDI-Ph, and (*R*)-CN-CPDI-Ph (All PDIs were synthesized by Prof. Xiaobo Shang in Xi'an Jiaotong University). The effects of bay-substitution on supramolecular chirality and optoelectronic performance were investigated through crystal structure analysis and computational calculation results. Each of the synthesized nanomaterials exhibited unique CD spectra due to differences in the atoms and substitution locale relative to the bay position of the PDI core, indicating that modification of bay-substitution has a significant effect on supramolecular chirality. (*R*)-CN-CPDI-Ph NWs, in particular, exhibited more desirable electronic performance than that of (*R*)-2F-CPDI-Ph or (*R*)-2Br-CPDI-Ph NWs. The crystal structure of (*R*)-CN-CPDI-Ph was suitable for charge transport and the excellent electron injectability of (*R*)-CN-CPDI-Ph enabled a high electron mobility of up to 0.17 $cm^2 V^{-1}s^{-1}$ and a low threshold voltage of −1 V. In addition, (*R*)-CN-CPDI-Ph NW-based OPTs exhibited a high photoresponsivity of up to 209 A W^{-1}. Compared to other PDI derivatives, all three bay-substituted NWs exhibited a relatively fast rise time of less than 0.45 s, indicating that bay-substitution can be used to tune response time.[8, 13] These findings demonstrate that the bay-substitution effect plays an important role in the supramolecular chirality and optoelectronic devices.

2.2. Results and Discussion

2.2.1. Characterization of bay-substituted PDI NWs.

The molecular structures of bay-substituted PDIs are shown in **Figure 2.1a**. Self-assembled NWs of bay-substituted (*R*)-2Br-CPDI-Ph, (*R*)-2F-CPDI-Ph, and (*R*)-CN-CPDI-Ph were fabricated using a nonsolvent-mediated recrystallization method. **Figure 2.1b** shows ultraviolet-visible (UV-vis) spectra of bay-substituted PDI materials in chloroform (1.0×10^{-5} M). Each compound exhibited four main absorption peaks: 528 nm, 492 nm, 461 nm, and 433 nm for (*R*)-2Br-CPDI-Ph; 512 nm, 475 nm, 446 nm, and 420 nm for (*R*)-2F-CPDI-Ph; and 532 nm, 495 nm, 465 nm, and 436 nm for (*R*)-CN-CPDI-Ph, corresponding to the 0–0, 0–1, 0–2, and 0–3 vibronic transitions of the individual molecules. The UV-vis spectra of self-assembled NWs of (*R*)-2Br-CPDI-Ph, (*R*)-2F-CPDI-Ph, and (*R*)-CN-CPDI-Ph showed a red-shift of ~50 nm relative to the solution spectra due to strong π–π stacking in the aggregated state (**Figure 2.1b**). Density functional theory (DFT) calculations and cyclic voltammetry (CV) measurements were applied to determine the energy levels of each system (**Figure 2.2, 2.3** and **Table 2.1**). CV measurements yielded a highest occupied molecular orbital (HOMO) energy of −6.25 eV and a LUMO energy of −3.99 eV for (*R*)-CN-CPDI-Ph. The low-lying LUMO levels of these bay-substituted PDIs indicate a high probability of *n*-type semiconducting performance.

CD measurements were performed to characterize the chiroptical response of enantiopure molecules in solution and with NWs that had been drop-cast onto a quartz plate. (*R*)-2Br-CPDI-Ph, (*R*)-2F-CPDI-Ph, and (*R*)-CN-CPDI-Ph in chloroform (10^{-5} M) did not exhibit any discernible CD signals at wavelengths greater than 400 nm, implying that these materials cannot inherit chirality from their pendant chiral phenylethylamine (**Figure 2.1c**). However, during self-assembly into nanomaterials, the chiral or spatial nonsymmetric arrangement was prone to be

adopted by the chromophores in order to lower the overall energy of the supramolecular system. Therefore, the chirality in the suparmolecular nanomaterials was amplified and CD spectroscopy could be used to detect their supramolecular chirality.[22] The CD features and dimensionless dissymmetry factor spectra of NWs were clearly observed between 400 nm and 650 nm, which indicates the chirality was transferred from the pendant to the supramolecular nanomaterials successfully (**Figure 2.1c**). However, (*R*)-2Br-CPDI-Ph, (*R*)-2F-CPDI-Ph, and (*R*)-CN-CPDI-Ph NWs exhibited bisignate Cotton effects with different chiral responses. For example, the main positive and negative peaks in the CD spectrum of (*R*)-2Br-CPDI-Ph were located at 498 nm and 564 nm. These shifted to 415 nm and 552 nm for (*R*)-2F-CPDI-Ph, and to 443 nm and 545 nm for (*R*)-CN-CPDI-Ph NWs. These data suggest that the supramolecular chirality of PDI NWs can be tuned by bay-substitution engineering. Intramolecular interactions dominate the monomeric state while the summed effects of intra- and intermolecular interactions may contribute to the significant enhancement of CD signals after assembly into NWs.[22] The morphologies of self-assembled bay substituted PDIs were shown in **Figure 2.1d** measured by scanning electron microscopy (SEM).

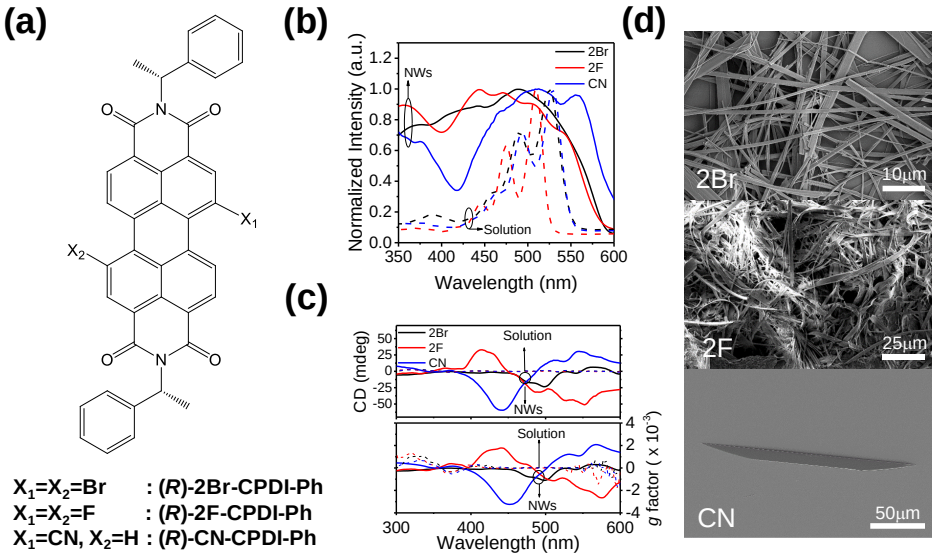

Figure 2.1. Characterization of bay substituted PDIs. **a**, Chemical Structures of bay-substituted PDIs. **b**, **c**, UV-vis spectra (**b**), and CD & dissymmetry factor spectra (**c**) of bay-substituted PDIs in chloroform solution (10^{-5} M) and their self-assembled NWs on quartz plate. **d**, SEM images of bay-substituted PDI NWs.

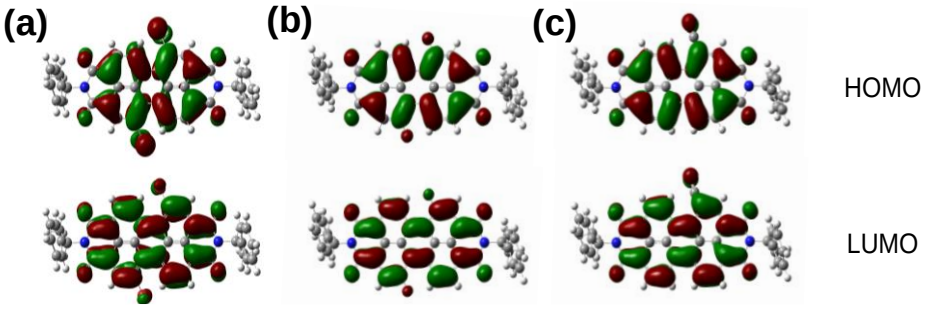

Figure 2.2. DFT calculation results of bay-substituted PDIs. a–**c**, HOMO and LUMO electron distributions of (*R*)-2Br-CPDI-Ph (**a**), (*R*)-2F-CPDI-Ph (**b**), and (*R*)-CN-CPDI-Ph (**c**).

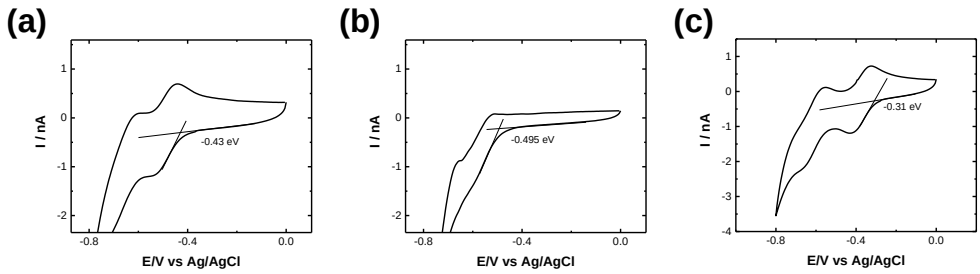

Figure 2.3. CV measurements results of bay substituted PDIs. **a**–**c**, Results of CV measurements from (*R*)-2Br-CPDI-Ph (**a**), (*R*)-2F-CPDI-Ph (**b**), (*R*)-CN-CPDI-Ph (**c**) in chloroform solutions (10^{-4} M).

Table 2.1. Energy level of bay-substituted PDI materials from CV measurements and DFT calculations.

	Material	Orbital	Energy level (eV)
DFT	(*R*)-2Br-CPDI-Ph	LUMO	–3.90
		HOMO	–6.40
	(*R*)-2F-CPDI-Ph	LUMO	–3.84
		HOMO	–6.37
	(*R*)-CN-CPDI-Ph	LUMO	–4.07
		HOMO	–6.54
CV	(*R*)-2Br-CPDI-Ph	LUMO	–3.87
		HOMO	–6.12
	(*R*)-2F-CPDI-Ph	LUMO	–3.81
		HOMO	–6.17
	(*R*)-CN-CPDI-Ph	LUMO	–3.99
		HOMO	–6.25

2.2.2. Single Crystal Analysis of Bay-Substituted PDIs. (conducted by Prof. Hiroyoshi Ohtsu in Tokyo Institute of Technology and Dr. Wanuk Choi in Korea Institute of Energy Research)

Crystals of bay-substituted PDIs were investigated using synchrotron single crystal X-ray diffraction (SXRD) analyses (**Figure 2.4**). The bay-substituted PDIs in each structure were π–π stacked along one direction and the shortest intermolecular contact distance between aromatized carbon atoms varied insignificantly: 3.28, 3.22, and 3.32 Å in 2F-, 2Br-, and CN-substituted PDIs, respectively (**Figure 2.5**). However, the effectiveness of π–π interactions differed significantly among these crystals. Crystals of (*R*)-2F-CPDI-Ph showed an offset from the mean plane of the center PDI core with a slipped stacking such that π–π interactions were relatively ineffective; only a part of the PDI molecule experiences π–π interactions (**Figure 2.4a**). The (*R*)-2Br-CPDI-Ph crystal contains a twisted center PDI core because of steric repulsion between Br atoms with a small slip stacking. Thus, only a small part of the PDI core can partake in π–π interactions (**Figure 2.4e**). In contrast, the (*R*)-CN-CPDI-Ph crystal shows no offset or twisting with only a small slip stacking. Therefore, the entire PDI core can contribute to π–π interactions (**Figure 2.4i**). Furthermore, the longitudinal displacement/roll angle of molecule by stacking is 1.3/140, 1.5/120 and 1.0/60 Å/° 2F-, 2Br-, and CN-substituted PDIs, respectively, indicating good overlap for CN-substituted ones. These interactions in the (*R*)-CN-CPDI-Ph crystal significantly differentiate the electrical properties of the (*R*)-CN-CPDI-Ph assembly from those of the other materials.

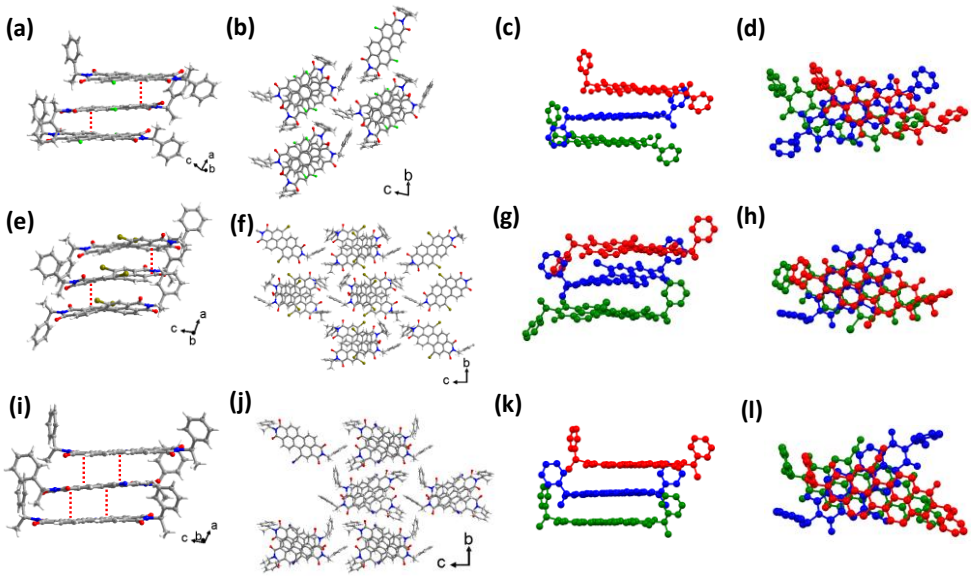

Figure 2.4. Crystal structures of bay substituted PDI NWs. a–c, Crystal strucrures of (*R*)-2F-CPDI-Ph; π–π stacking sequence (**a**), packing view down *a*-axis (**b**), π–π stacking sequence with colored molecules (**c**), overlapping view of the **c** molecules (**d**), **e**–**h**, (*R*)-2Br-CPDI-Ph; π–π stacking sequence (**e**), packing view down *a*-axis (**f**), π–π stacking sequence with colored molecules (**g**), overlapping view of the **g** molecules (**h**), and **i**–**l**, (*R*)-CN-CPDI-Ph; π–π stacking sequence (**i**), packing view down *a*-axis (**j**), π–π stacking sequence with colored molecules (**k**), overlapping view of the **k** molecules (**l**). C, gray; N, blue; O, red; Hydrogen atoms and solvent molecules are omitted for clarity.

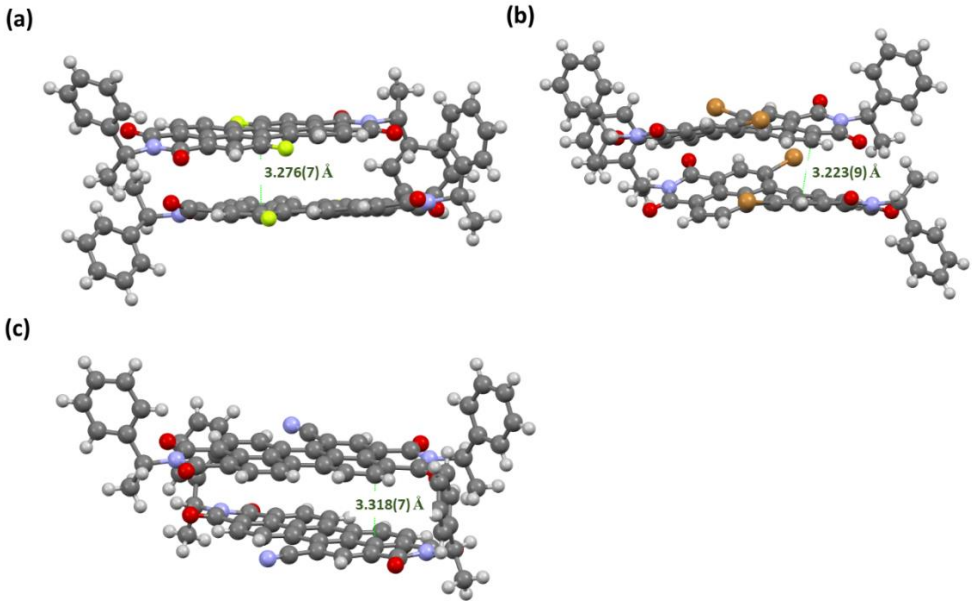

Figure 2.5. Crystal structures showing shortest C…C distances for π–π stacking. **a**–**c**, (*R*)-2F-CPDI-Ph (**a**), (*R*)-2Br-CPDI-Ph (**b**), (*R*)-CN-CPDI-Ph (**c**). Color code: C, gray; N, blue; O, red; H, white.

2.2.3. Bay-Substitution Effect on Optoelectronic Properties of Chiral PDI-based Nanomaterials

To investigate the optoelectrical properties of bay-substituted PDI NWs, OPTs with a bottom-gate top-contact configuration were fabricated. Optical images of individual bay-substitued PDI NWs-based devices are shown in **Figure 2.6**. The active channel dimensions were estimated from the width and length of an individual NW spanning the source and drain electrodes. **Figures 2.7a–c** and **Figure 2.8** illustrate the typical transfer and output characteristics of individual (*R*)-2Br-CPDI-Ph, (*R*)-2F-CPDI-Ph, and (*R*)-CN-CPDI-Ph NW-based OFETs in a nitrogen atmosphere, respectively. All three bay-substituted NWs exhibited typical *n*-type characteristics. The electrical performance of these devices is summarized in **Table 2.2**. The estimated on- and off-current ratios (I_{on}/I_{off}) of all bay-substituted NWs were in the range of 10^3 to 10^4. **Figure 2.7d** shows a graph comparing the mobility and threshold voltage of each bay-substituted NW-based device. Due to the bay-substitution effect, (*R*)-2Br-CPDI-Ph, (*R*)-2F-CPDI-Ph, and (*R*)-CN-CPDI-Ph exhibited different average electron mobilities of 0.019, 0.038, and 0.074 $cm^2\ V^{-1}s^{-1}$ in the saturation regime, respectively. (*R*)-CN-CPDI-Ph yielded the highest electron mobility of 0.17 $cm^2\ V^{-1}s^{-1}$. (*R*)-2Br-CPDI-Ph and (*R*)-2F-CPDI-Ph showed V_T values of 24.1 and 28.1 V, respectively. In contrast, (*R*)-CN-CPDI-Ph exhibited a V_T of −1 V, indicating outstanding electrical performance in terms of both electron mobility and threshold voltage. To our knowledge, reports on mono-substituted PDI supramolecular nanomaterials as chiral semiconductors are relatively rare. The higher mobility of (*R*)-CN-CPDI-Ph NW is a function of its crystal structure. As mentioned above, among the crystals examined, the effectiveness of π-π interactions was highest with (*R*)-CN-CPDI-Ph crystals because of efficient π-plane overlap and resulted in higher mobility.

A 520 nm monochromic light source was used to characterize photoresponsivity of NW-OPT devices. **Figure 2.9a** shows the transfer characteristics of (*R*)-CN-

CPDI-Ph NW-OPTs as a function of illumination intensity. The current in the NW-OPTs increased significantly while threshold voltage became increasingly negative. This corresponds to an easier device turn-on. The elimination of trap sites by the photo-generated charge carrier contributes to the "*n*-doping effect".

R, *P*, EQE (η), and D^* are important figures of merit when comparing OPTs and are determined from the transfer characteristics of the device under illumination. *R*, *P*, EQE, and D^* are typically defined according to the equations provided in the Supporting Information. Each of these figures of merit was determined for (*R*)-CN-CPDI-Ph NW-OPTs under illumination intensities of 10 and 90 μW cm^{-2}, and are plotted as a function of gate voltage in **Figures 2.9b** and **c**. Similar graphs show the transfer characteristics of (*R*)-2Br-CPDI-Ph and (*R*)-2F-CPDI-Ph in **Figures 2.10** and **2.11**. I observed that both photocurrent and dark current were affected by an applied positive gate bias, demonstrating that an induced field-effect enhances the optoelectronic performance of these devices. **Figures 2.9e** and **f** compare the optoelectronic performance of devices made with each of our NW materials. (*R*)-2Br-CPDI-Ph and (*R*)-2F-CPDI-Ph NWs showed maximum *R*, *P*, EQE, and D^* values of 49 A W^{-1}, 2.0, 11,749%, and 2.7×10^{12} Jones and 50 A W^{-1}, 16, 11,955%, and 1.8×10^{12} Jones, respectively, under 30 μW cm^{-2} illumination. In comparison, the maximum *R*, *P*, EQE, and D^* values for (*R*)-CN-CPDI-Ph NWs were 209 A W^{-1}, 51, 49,680%, and 4.1×10^{12} Jones (**Table 2.3**). Note that the *R* and EQE of (*R*)-CN-CPDI-Ph NWs were four-fold higher than those of (*R*)-2Br-CPDI-Ph and (*R*)-2F-CPDI-Ph NWs. The enhanced OPTs performance of (*R*)-CN-CPDI-Ph NWs may be related to their crystal structures and better charge transport characteristics.

Real-time photoswitching of (*R*)-2Br-CPDI-Ph, (*R*)-2F-CPDI-Ph, and (*R*)-CN-CPDI-Ph NWs was performed under pulsed incident light (90 μW cm^{-2}) using a V_{GS} of −10 V for (*R*)-CN-CPDI-Ph and 20 V for the others. These voltages correspond to values where maximum photosensitivities were observed. A plot of experimental photoswitching ratios with a bi-exponential fit for the calculated photoresponse time

of a (*R*)-CN-CPDI-Ph-based OPT are shown in **Figure 2.9d**. The estimated rise (t_r) and decay times (t_d) were 0.44 and 2 s for (*R*)-CN-CPDI-Ph NWs, 0.2 and 0.54 s for (*R*)-2Br-CPDI-Ph (**Figure 2.10**), and 0.24 and 0.76 s for (*R*)-2F-CPDI-Ph (**Figure 2.11**), respectively. The response times are much lower than those of previous PDI-based nanomaterials,[8, 13] indicating that bay substitution is an effective means of obtaining short photoresponse times relative to those typically obtained with *N*-substituted PDI NWs with twisted π-planar backbone structures.

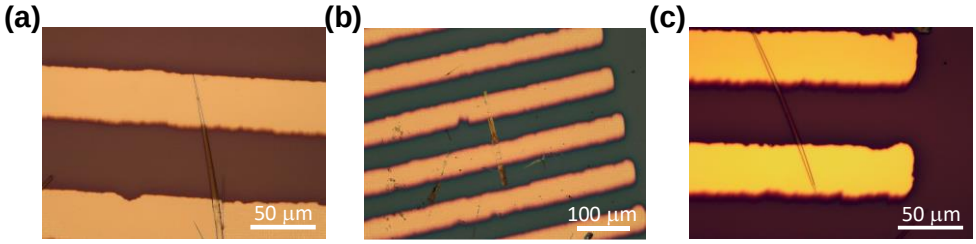

Figure 2.6. Optical microscope images of bay-substituted PDI NWs. a–c, (*R*)-2Br-CPDI-Ph (**a**), (*R*)-2F-CPDI-Ph (**b**), and (*R*)-CN-CPDI-Ph (**c**) NWs.

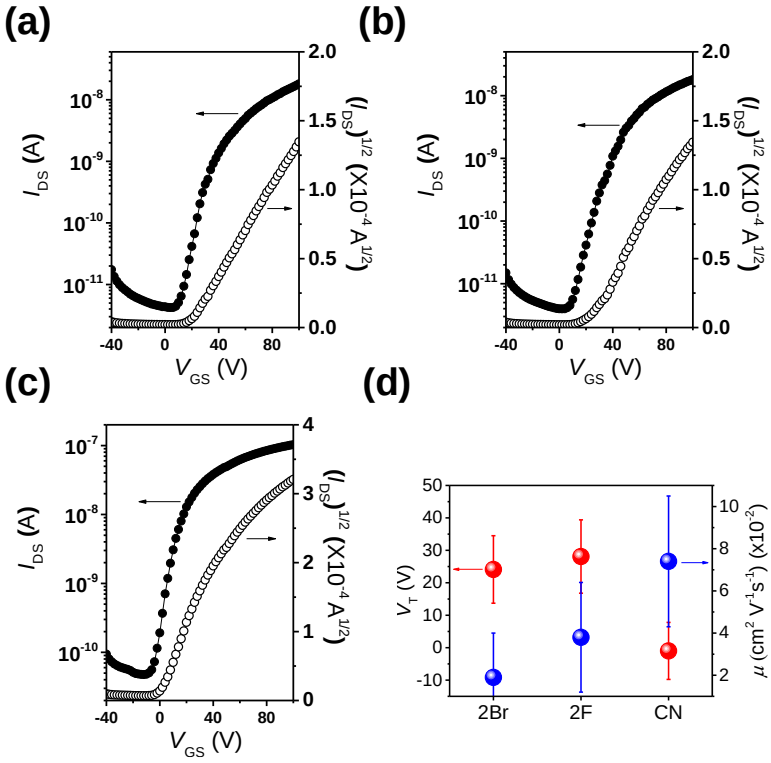

Figure 2.7. Electrical properties of bay-substituted PDI NWs. a–c, I_{DS}–V_{GS} characteristics of based (*R*)-2Br-CPDI-Ph (**a**), (*R*)-2F-CPDI-Ph (**b**), and (*R*)-CN-CPDI-Ph (**c**) NWs-based OFETs. **d**, Mobility and threshold voltage comparison graph which were obtained for at least ten NWs. The measurements were performed in a nitrogen atmosphere.

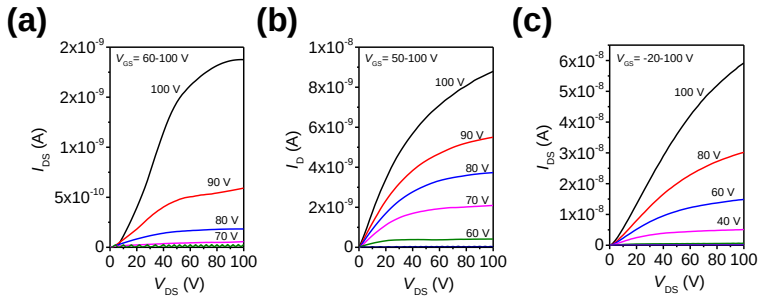

Figure 2.8. Output characteristics of bay-substituted PDI NWs. a–c, (*R*)-2Br-CPDI-Ph (**a**), (*R*)-2F-CPDI-Ph (**b**), and (*R*)-CN-CPDI-Ph (**c**) NWs-based OFET in the dark condition.

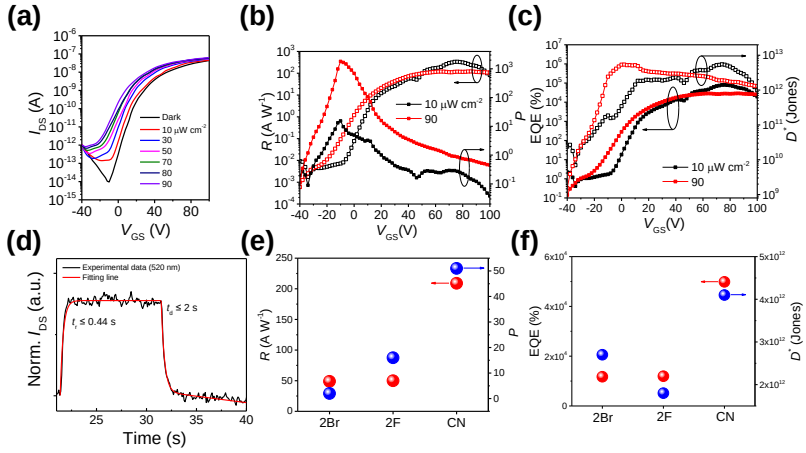

Figure 2.9. Optoelectronic properties of (*R*)-CN-CPDI-Ph NWs and comparison between bay-substituted PDI NWs. a, I_{DS}–V_{GS} characteristics of (*R*)-CN-CPDI-Ph in the dark and under monochromatic light illumination (λ = 520 nm) with various intensities. **b–c**, *R*, *P* (**b**), EQE, and D^* (**c**) of (*R*)-CN-CPDI-Ph NWs-based OPTs under 10 and 90 μW cm^{-2} light intensities. **d**, Bi-exponential fitting result of (*R*)-CN-CPDI-Ph NWs-based OPT for the photoresponse time calculation. **e–f**, Comparison graph of the maximum photoresponsivity and photosensitivity (**e**), EQE and specific detectivity (**f**) values of bay-substituted PDI NWs-based OPTs under monochromatic light illumination (λ = 520 nm) with 30 μW cm^{-2} light intensity.

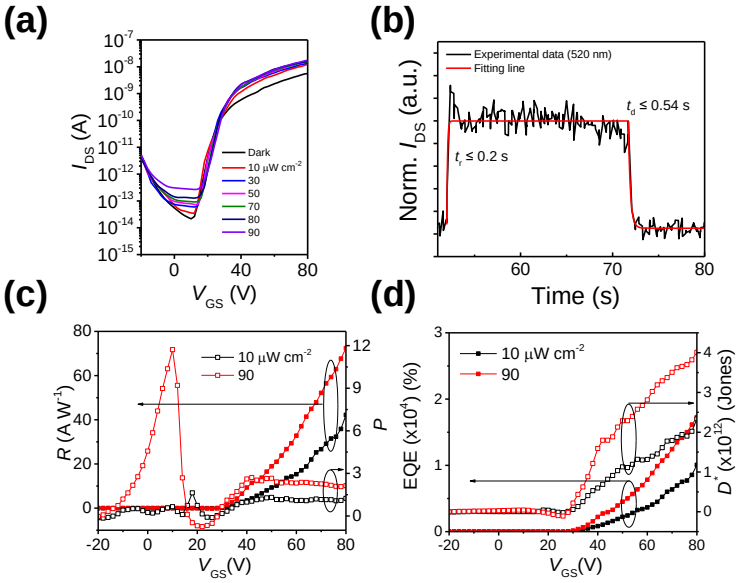

Figure 2.10. Optoelectronic properties of (*R*)-2Br-CPDI-Ph NWs. a, I_{DS}–V_{GS} characteristics of (*R*)-2Br-CPDI-Ph NWs in the dark and under monochromatic light illumination (λ = 520 nm) with various intensities. **b**, Bi-exponential fitting result for the photoresponse time calculation. **c**–**d,** Photoresponsivity, photosensitivity (**c**), EQE, and specific detectivity (**d**) of (*R*)-2Br-CPDI-Ph NW-based OPTs under 10 and 90 μW cm^{-2} light intensities.

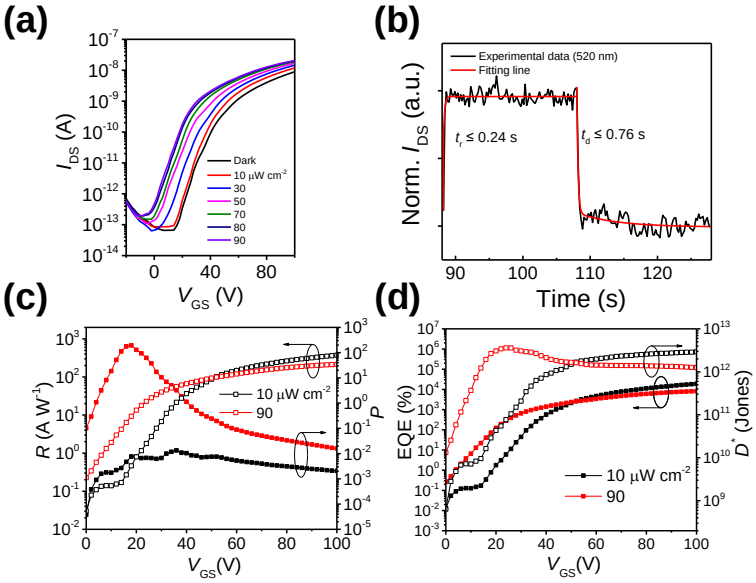

Figure 2.11. Optoelectronic properties of (*R*)-2F-CPDI-Ph NWs. a, I_{DS}–V_{GS} characteristics of (*R*)-2F-CPDI-Ph NWs in the dark and under monochromatic light illumination (λ = 520 nm) with various intensities. **b**, Bi-exponential fitting result for the photoresponse time calculation. **c**–**d**, Photoresponsivity, photosensitivity (**c**), EQE, and specific detectivity (**d**) of (*R*)-2F-CPDI-Ph NW-based OPTs under 10 and 90 μW cm^{-2} light intensities.

Table 2.2. Electrical characteristics of bay-substituted PDI NWs-based OFETs.

Material	I_{on}/I_{off}	V_T (V)	μ^a ($cm^2\ V^{-1}s^{-1}$)
(*R*)-2Br-CPDI-Ph	$>10^3$	24.1 (± 10.4)	0.019 (± 0.021)
(*R*)-2F-CPDI-Ph	$>10^3$	28.1 (± 11.3)	0.038 (± 0.026)
(*R*)-CN-CPDI-Ph	$>10^3$	–1.00 (± 8.78)	0.074 (± 0.031)

[a]Average values extracted from more than ten NWs.

Table 2.3. Optoelectronic characteristics of bay-substituted PDI NWs-based OPTs.

Material	P^a	R ($A\ W^{-1}$)	EQE (%)	D^* (Jones)
(*R*)-2Br-CPDI-Ph	2.0	49	11749	2.7×10^{12}
(*R*)-2F-CPDI-Ph	16	50	11955	1.8×10^{12}
(*R*)-CN-CPDI-Ph	51	209	49680	4.1×10^{12}

[a]Maximum values under monochromic light illumination (λ = 520 nm, 30 $\mu W\ cm^{-2}$)

2.2.4. Computational Studies of Bay-Substitution Eeffect on Electronic Properties of Chiral PDI-based Nanomaterials (conducted by Jeong Hyeon Lee, and Jin Chul Kim under the supervision of Prof. Sang Kyu Kwak in Ulsan National Institute of Science and Technology (UNIST))

DFT calculations were performed to further explain the mechanism responsible for the higher mobility in (*R*)-CN-CPDI-Ph NWs. In a π-stacked system like bay-substituted PDIs, charge carriers are typically transported through a hopping mechanism. Thus, the optoelectronic properties of these materials are closely related to the intermolecular electron hopping rate (*k*). Therefore, to investigate the effects of bay-substitution on electron mobility, Two factors influencing the electron hopping rate, *i.e.*, the electron reorganization energy and the transfer integral were calculated, as described by the Marcus–Hush equation.[25, 26] The calculated electron reorganization energies of isolated (*R*)-2Br-CPDI-Ph, (*R*)-2F-CPDI-Ph, and (*R*)-CN-CPDI-Ph molecules were 298.0, 299.9, and 275.8 meV, respectively, indicating that electron transfer between CN-substituted molecules is more advantageous than in bromine- and fluorine-substituted analogs (**Table 2.4**). Also as indicated by a reverse trend in EA and small bluish region of electron density shown in **Figure 2.9**, electron injection or transfer to neighboring molecules was expected to be more hampered at the CPDI-Ph with halogen substituent, where larger amount of electrons were distributed in the PDI moiety compared to (*R*)-CN-CPDI-Ph. To further identify the factors resulting in the high electron mobility of (*R*)-CN-CPDI-Ph, transfer integrals of several pairs in bay-substituted PDI crystals were estimated (**Figures 2.10a–d, Table 2.5**). The π–π stacked pairs, denoted by l_1 and l_2, had relatively large transfer integrals compared to van der Waals interaction pairs with long intermolecular distances and distorted orientations, denoted by l_3 and l_4. Particularly, among π–π stacked pairs, (*R*)-CN-CPDI-Ph had approximately twice the transfer integral as the

other systems at the l_1 pair. This originates from the well-aligned and flat PDI moieties in the (*R*)-CN-CPDI-Ph assembly. Finally, in considering electron reorganization energies and transfer integrals, the electron hopping rates of each bay-substituted PDI crystal were calculated at room temperature according to the Marcus–Hush equation (**Figure 2.10e**). As expected, the (*R*)-CN-CPDI-Ph crystal showed a higher electron hopping rate than the other halogen-substituted crystals. This result is consistent with the experimentally observed trend in electron mobility. Thus, substitution of CN contributes to a simultaneous increase in electron injectability and structural order, resulting in enhanced charge carrier mobility in the synthesized NWs.

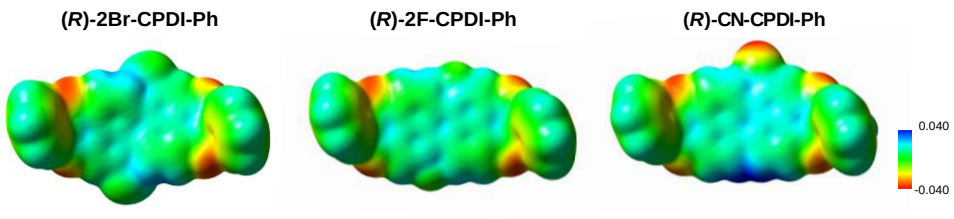

Figure 2.12. Electrostatic potential-mapped electron density of bay-substituted PDI molecules. Red and blue represent the electron rich and deficient regions, respectively.

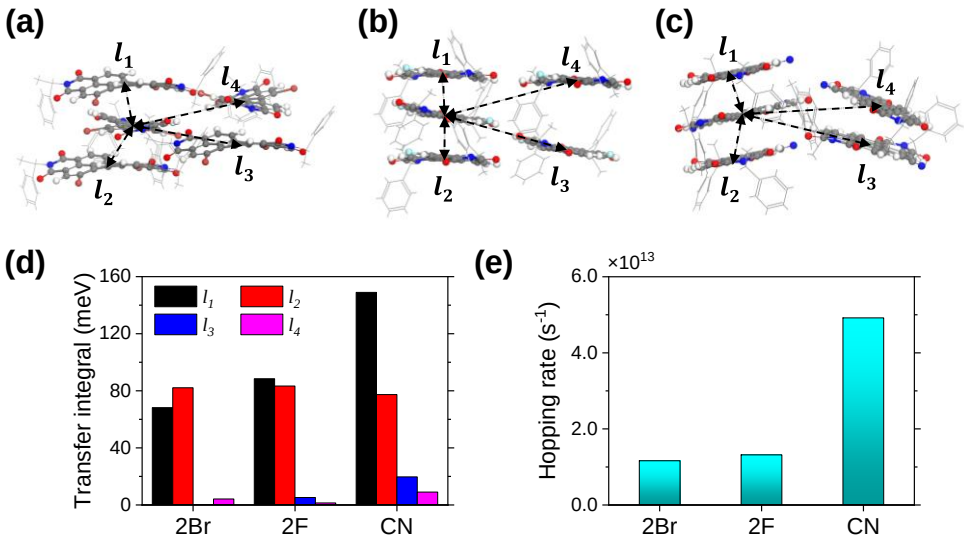

Figure 2.13. DFT Calculation results of bay-substituted PDI NWs. a–c, Stacking configurations and interacting pairs (l_1 – l_4) of interest for calculating transfer integrals in (*R*)-2Br-CPDI-Ph crystal (**a**), (*R*)-2F-CPDI-Ph crystal (**b**), and (*R*)-CN-CPDI-Ph crystal (**c**). PDI moieties and ther other atoms are shown by ball-and-stick and line model, respectively. Carbon, hydrogen, oxygen, nitrogen, bromine, fluorine atoms are colored in grey, white, red, blue, brown, cyan, respectively. **d**, Calculated transfer integrals in bay-substituted PDI crystals. **e**, Maximum electron hopping rate of bay-substituted PDI crystals at room temperature.

Table 2.4. Summary of DFT results for the calculation of electron reorganization energy and electron affinity.

	E_0 (Ha)	E_0^* (Ha)	E_- (Ha)	E_-^* (Ha)	λ_0 (meV)	λ_- (meV)	λ (meV)	EA (eV)
2Br	–7092.796	–7092.791	–7092.904	–7092.898	148.3	149.7	298.0	2.92
2F	–2149.035	–2149.029	–2149.139	–2149.133	148.6	151.3	299.9	2.83
CN	–2042.798	–2042.793	–2042.910	–2042.905	137.2	138.6	275.8	3.34

Table 2.5. Structural information of pairs in DFT-optimized bay-substituted PDI crystals. Center of PDI was defined as center of mass of the central benzene ring. Stacking distance was defined as the distance from one center to the other PDI plane.

		Center-to-center distance (Å)	Stacking distance (Å)	Angle between PDI planes (°)
(*R*)-2Br-CPDI-Ph	l_1	4.47	3.36	9.60
	l_2	4.38	3.52	9.60
	l_3	19.02	0.26	9.60
	l_4	10.33	2.85	6.62
(*R*)-2F-CPDI-Ph	l_1	3.95	3.59	8.87
	l_2	4.41	3.33	8.87
	l_3	12.22	0.88	0.0
	l_4	15.76	3.19	8.87
(*R*)-CN-CPDI-Ph	l_1	4.58	3.32	3.28
	l_2	3.57	3.42	3.28
	l_3	10.67	4.67	32.01
	l_4	11.11	4.35	34.67

2.3. Conclusion

The supramolecular chirality and optoelectronic properties of chiral PDIs with different bay-substituent configurations were investigated. Bay-substituted PDI derivatives (*R*)-2Br-CPDI-Ph, (*R*)-2F-CPDI-Ph, and (*R*)-CN-CPDI-Ph were self-assembled into 1D nanomaterials *via* nonsolvent-mediated recrystallization from mixtures of DCM, DCE, and DMF as good solvents and methanol as a nonsolvent. The morphologies and crystal structures of these materials were characterized by SEM and SXRD, revealing self-assembly of highly ordered NWs. Mono-substituted (*R*)-CN-CPDI-Ph NWs exhibited a higher electron mobility (0.17 $cm^2 V^{-1}s^{-1}$) than (*R*)-2Br-CPDI-Ph and (*R*)-2F-CPDI-Ph. DFT calculations suggested that the electron mobility of (*R*)-CN-CPDI-Ph is caused by simultaneous increases in electron injectability and π-stacking order in the crystal structure. Furthermore, (*R*)-CN-CPDI-Ph NWs showed outstanding optoelectronic performance with maximum *P*, *R*, EQE, and D^* values of 209 A W^{-1}, 51, 49,680%, and 4.1×10^{12} Jones, respectively. The *R* and EQE values were approximately four-fold higher than those of (*R*)-2Br-CPDI-Ph and (*R*)-2F-CPDI-Ph analogs. In addition, bay-substitution reduced the photoswitching rise time of PDI NWs to less than 0.45 s. This is much faster than similar materials with substituents only at the imide positions. Interestingly, the self-assembly and supramolecular chirality characteristics of (*R*)-2Br-CPDI-Ph, (*R*)-2F-CPDI-Ph, and (*R*)-CN-CPDI-Ph NWs were unique and could be tuned by altering the bay substituent. These results show that molecular modulation of organic semiconductor structure *via* the bay-substitution effect can be used to effectively tune the optoelectronic performance and supramolecular chirality, providing an in-depth understanding of structure–chirality–property relationship.

2.4. Experimental Details

2.4.1. Synthesis of Bay-Substituted Chiral PDIs and Fabrication of Single-Crystalline NWs

(*R*)-2Br-CPDI-Ph and (*R*)-2F-CPDI-Ph were synthesized according to a previously reported method.[23] (*R*)-Br-CPDI-Ph was synthesized from monobromo-substituted 6,7,12,13-tetrachloro-3,4,9,10-perylene tetracarboxylic acid dianhydride[24] and (*R*)-1-phenylethylamine. (*R*)-CN-CPDI-Ph was obtained by subsequent cyanation (All three PDIs were synthesized by Prof. Xiaobo Shang in Xi'an Jiaotong University). Two additional analogues (*R*)-2CN-CPDI-Ph and (*R*)-F-CPDI-Ph were also synthesized, but failed to grow suitable nanomaterials for optoelectronic devices via self-assembly. Therefore, I focused on (*R*)-2Br-CPDI-Ph, (*R*)-2F-CPDI-Ph, and (*R*)-CN-CPDI-Ph, which could be fabricated into NWs using a nonsolvent-mediated recrystallization method.[25] For the fabrication of NWs, methanol, as a nonsolvent, was injected into a dichloromethane (DCM) solution of (*R*)-2Br-CPDI-Ph (1 mg mL^{-1}) at a 1:1 ratio (good solvent:nonsolvent), a dichloroethane (DCE) solution of (*R*)-2F-CPDI-Ph (1 mg mL^{-1}) at a 1:2 ratio, and an *N,N*–dimethylformamide (DMF) solution of (*R*)-CN-CPDI-Ph (0.5 mg mL^{-1}) at 1:1 ratio. The concentration of each solution and the amount of methanol were adjusted such that the size and amount of the resulting NWs were suitable for device fabrication (hundreds of nanometers long). Solutions were allowed to form NWs overnight.

2.4.2. Fabrication of Organic Phototransistors

The *n*-octadecyltrimethoxysilane (OTS)-treated wafers were prepared with the same method as the previous report.[19] The fabricated (*R*)-2Br-CPDI-Ph, (*R*)-2F-CPDI-Ph, and (*R*)-CN-CPDI-Ph NWs were filtered under a vacuum with a porous aluminum oxide membrane to remove the uncrystallized solutes. Then NWs

dispersed in ethanol were dropped onto OTS-treated SiO_2/Si wafers. The droplets were rolled in all directions until a sufficient amount of NWs were placed on the wafer, and then they were removed. To evaporate the remaining solvent, the devices were annealed at 60℃ overnight in a vacuum oven. The source and drain electrodes consisted of 150 nm layers of gold and were thermally evaporated at 5×10^{-6} Torr through a shadow mask.

2.4.3. Density Functional Theory Calculations

To investigate the theoretical electron mobility of our bay-substituted PDIs, DFT calculations were conducted using the crystal and molecular structures of bay-substituted PDIs. The electron mobilities of bay-substituted PDIs depended on the intermolecular electron hopping rate (k), which was calculated using the Marcus–Hush equation:

$$k = \frac{V^2}{\hbar}\sqrt{\frac{\pi}{\lambda k_B T}}\exp\left(-\frac{\lambda}{4k_B T}\right) \tag{1}$$

where V is the transfer integral between neighboring PDIs and λ is the reorganization energy of electrons in each PDI molecule.[26, 27] $\hbar$, k_B, and T are Dirac's constant, the Boltzmann constant, and temperature, respectively. The transfer integral value of electrons in two neighboring PDIs, which represents the degree of overlap between two interacting orbitals, is defined as

$$V = \langle \varphi_1 | H | \varphi_2 \rangle \tag{2}$$

where $|\varphi_1\rangle$ and $|\varphi_2\rangle$ are the lowest unoccupied molecular orbitals (LUMOs) of PDI molecules 1 and 2, respectively. Note that in a π–π stacked structure, the energy levels of the LUMO and LUMO+1 states are typically very close to each other. Therefore, when calculating transfer integrals, mixed-state methods were applied as developed by Li *et al*.[28] The electron reorganization energy was calculated using the following equation:[29]

$$\lambda = \lambda_0 + \lambda_- = \left(E_0^* - E_0\right) + \left(E_-^* - E_-\right) \quad (3)$$

Note that high electron mobility in a bay-substituted PDI assembly requires a large transfer integral with a well-stacked configuration, *i.e.*, a high degree of orbital overlap in the crystal structure, in addition to only a minimal reorganization energy of the PDI molecule itself. Electron affinity (EA) was also calculated by subtracting E_- from E_0 to compare the relative stability of the electron accepted state.

To calculate the electron transfer integral of a pair of bay-PDI molecules, unit cell structures obtained from experimental crystallography data were initially optimized using the DFT calculations implemented by the Dmol[3] program[30, 31] using the Perdew–Burke–Ernzerhof exchange-correlation functional and the DNP 4.4 basis set.[32] Van der Waals interactions were corrected via the Tkatchenko–Scheffler method.[33] Since the transfer integral is significantly affected by the separation distance and orientation of an interacting pair, several neighboring pairs around one PDI molecule were identified. Then, for each pair of PDIs, single-point energy calculations were conducted for the pair and each constituting PDI using Gaussian 16[34] with Becke's three-parameter nonlocal exchange,[35] the Lee–Yang–Parr nonlocal correlation[36] functional, and the 6-31+G** basis set. To calculate reorganization energies, the configuration of an isolated bay-substituted PDI molecule was optimized using Gaussian 16 with the same functional and basis set as above.[34]

2.4.4. X-ray Crystallography

X-ray Crystallographic Data for (R)-CN-CPDI-Ph Single Crystal.

$C_{41}H_{25}N_3O_4$ (M = 623.64 g/mol): monoclinic, space group $P2_1$ (no. 4), a = 7.8360(16) Å, b = 21.112(4) Å, c = 18.169(4) Å, β = 101.14(3)°, V = 2949.1(11) Å^3, Z = 4, T = 100(2) K, μ(synchrotron) = 0.054 mm^{-1}, $Dcalc$ = 1.405 g/cm^3, 16784 reflections measured (2.944° ≤ 2θ ≤ 59.886°), 16771 unique

(R_{int} = 0.066, R_{sigma} = 0.0530) which were used in all calculations. The final R_1 was 0.0982 (I > 2σ(I)) and wR_2 was 0.3001 (all data). Flack parameter: –0.1(6); the enantiomer has been assigned by reference to an unchanging chiral center in the synthetic procedure. CCDC: 1889908.

X-ray Crystallographic Data for (R)-2F-CPDI-Ph Single Crystal.

$C_{40.5}H_{25}ClF_2N_2O_4$ (M = 677.07 g/mol): triclinic, space group $P1$ (no. 1), a = 8.3170(17) Å, b = 12.218(2) Å, c = 15.239(3) Å, α = 77.72(3)°, β = 87.35(3)°, γ = 86.42(3)°, V = 1509.3(6) Å^3, Z = 2, T = 100(2) K, μ(synchrotron) = 0.142 mm^{-1}, *Dcalc* = 1.490 g/cm^3, 27301 reflections measured (3.364° ≤ 2θ ≤ 57.298°), 13531 unique (R_{int} = 0.045, R_{sigma} = 0.0646) which were used in all calculations. The final R_1 was 0.0709 (I > 2σ(I)) and wR_2 was 0.2113 (all data). Flack parameter: 0.14(4); The enantiomer has been assigned by reference to an unchanging chiral center in the synthetic procedure and anomalous dispersion of single crystal diffraction. CCDC: 1889911

X-ray Crystallographic Data for (R)-2Br-CPDI-Ph Single Crystal.

$C_{40.5}H_{24.75}Br_2Cl_{0.75}N_2O_4$ (M = 789.78 g/mol): monoclinic, space group $P2_1$(no. 4), a = 8.1830(16) Å, b = 22.095(4) Å, c = 17.827(4) Å, β = 102.33(3)°, V = 3148.8(11) Å^3, Z = 4, T = 100(2) K, μ(synchrotron) = 2.525 mm^{-1}, *Dcalc* = 1.666 g/cm^3, 29705 reflections measured (2.932° ≤ 2θ ≤ 59.748°), 17889 unique (R_{int} = 0.0920, R_{sigma} = 0.0881) which were used in all calculations. The final R_1 was 0.0595 (I > 2σ(I)) and wR_2 was 0.1722 (all data). Flack parameter: 0.013(4); the enantiomer has been assigned by reference to an unchanging chiral center in the synthetic procedure and anomalous dispersion of single crystal diffraction. CCDC: 1889912

2. 5. References

(1) Shang, X.; Song, I.; Ohtsu, H.; Lee, Y. H.; Zhao, T.; Kojima, T.; Jung, J. H.; Kawano, M.; Oh, J. H. Supramolecular Nanostructures of Chiral Perylene Diimides with Amplified Chirality for High-Performance Chiroptical Sensing. *Adv. Mater.* **2017,** *29*, 1605828.

(2) Chen, S.; Slattum, P.; Wang, C.; Zang, L. Self-Assembly of Perylene Imide Molecules into 1d Nanostructures: Methods, Morphologies, and Applications. *Chem. Rev.* **2015,** *115*, 11967-11998.

(3) Shang, X.; Song, I.; Jung, G. Y.; Choi, W.; Ohtsu, H.; Lee, J. H.; Koo, J. Y.; Liu, B.; Ahn, J.; Kawano, M.; Kwak, S. K.; Oh, J. H. Chiral Self-Sorted Multifunctional Supramolecular Biocoordination Polymers and Their Applications in Sensors. *Nat. Commun.* **2018,** *9*, 3933.

(4) Shang, X.; Song, I.; Lee, J. H.; Choi, W.; Ohtsu, H.; Jung, G. Y.; Ahn, J.; Han, M.; Koo, J. Y.; Kawano, M.; Kwak, S. K.; Oh, J. H. Heterochiral Doped Supramolecular Coordination Networks for High-Performance Optoelectronics. *ACS Appl. Mater. Interfaces* **2019,** *11*, 20174-20182.

(5) Yu, H.; Kim, D. Y.; Lee, K. J.; Oh, J. H. Fabrication of One-Dimensional Organic Nanomaterials and Their Optoelectronic Applications. *J. Nanosci. Nanotechnol.* **2014,** *14*, 1282-1302.

(6) Zhang, X.; Jie, J.; Deng, W.; Shang, Q.; Wang, J.; Wang, H.; Chen, X.; Zhang, X. Alignment and Patterning of Ordered Small-Molecule Organic Semiconductor Micro-/Nanocrystals for Device Applications. *Adv. Mater.* **2016,** *28*, 2475-2503.

(7) Wang, Y.; Xu, J.; Wang, Y.; Chen, H. Emerging Chirality in Nanoscience. *Chem. Soc. Rev.* **2013,** *42*, 2930-2962.

(8) Shang, X.; Song, I.; Ohtsu, H.; Tong, J.; Zhang, H.; Oh, J. H. Morphogenesis and Optoelectronic Properties of Supramolecular Assemblies of Chiral Perylene Diimides in a Binary Solvent System. *Sci. Rep.* **2017,** *7*, 5508.

(9) Shang, X.; Song, I.; Lee, J. H.; Han, M.; Kim, J. C.; Ohtsu, H.; Ahn, J.; Kwak, S. K.; Oh, J. H. Tuning the Supramolecular Chirality and Optoelectronic Performance of Chiral Perylene Diimide Nanowires Via N-Substituted Side Chain Engineering. *J. Mater. Chem. C* **2019,** *7*, 8688-8697.

(10) Yu, H.; Bao, Z.; Oh, J. H. High-Performance Phototransistors Based on Single-Crystalline N-Channel Organic Nanowires and Photogenerated Charge-Carrier Behaviors. *Adv. Funct. Mater.* **2013,** *23*, 629-639.

(11) Guo, Y.; Du, C.; Yu, G.; Di, C.-a.; Jiang, S.; Xi, H.; Zheng, J.; Yan, S.; Yu, C.; Hu, W.; Liu, Y. High-Performance Phototransistors Based on Organic Microribbons Prepared by a Solution Self-Assembly Process. *Adv. Funct. Mater.* **2010,** *20*, 1019-1024.

(12) Kim, K. H.; Bae, S. Y.; Kim, Y. S.; Hur, J. A.; Hoang, M. H.; Lee, T. W.; Cho, M. J.; Kim, Y.; Kim, M.; Jin, J.-I.; Kim, S.-J.; Lee, K.; Lee, S. J.; Choi, D. H. Highly Photosensitive *J*-Aggregated Single-Crystalline Organic Transistors. *Adv. Mater.* **2011,** *23*, 3095-3099.

(13) Jung, J. H.; Yoon, M. J.; Lim, J. W.; Lee, Y. H.; Lee, K. E.; Kim, D. H.; Oh, J. H. High-Performance UV–Vis–NIR Phototransistors Based on Single-Crystalline Organic Semiconductor–Gold Hybrid Nanomaterials. *Adv. Funct. Mater.* **2017,** *27*, 1604528.

(14) Li, C.; Wonneberger, H. Perylene Imides for Organic Photovoltaics: Yesterday, Today, and Tomorrow. *Adv. Mater.* **2012,** *24*, 613-636.

(15) Würthner, F.; Saha-Möller, C. R.; Fimmel, B.; Ogi, S.; Leowanawat, P.; Schmidt, D. Perylene Bisimide Dye Assemblies as Archetype Functional Supramolecular Materials. *Chem. Rev.* **2016,** *116*, 962-1052.

(16) Gsänger, M.; Bialas, D.; Huang, L.; Stolte, M.; Würthner, F. Organic Semiconductors Based on Dyes and Color Pigments. *Adv. Mater.* **2016,** *28*, 3615-3645.

(17) Zhan, X.; Facchetti, A.; Barlow, S.; Marks, T. J.; Ratner, M. A.; Wasielewski, M. R.; Marder, S. R. Rylene and Related Diimides for Organic Electronics. *Adv. Mater.* **2011,** *23*, 268-284.

(18) Shang, X.; Song, I.; Lee, J. H.; Choi, W.; Ahn, J.; Ohtsu, H.; Kim, J. C.; Koo, J. Y.; Kwak, S. K.; Oh, J. H. Surface-Doped Quasi-2D Chiral Organic Single Crystals for Chiroptical Sensing. *ACS Nano* **2020,** *14*, 14146-14156.

(19) Song, I.; Ahn, J.; Shang, X.; Oh, J. H. Optoelectronic Property Modulation in Chiral Organic Semiconductor/Polymer Blends. *ACS Appl. Mater. Interfaces* **2020,** *12*, 49926-49934.

(20) Shang, X.; Song, I.; Han, M.; Lee, J. H.; Ohtsu, H.; Choi, W.; Kim, J. C.; Ahn, J.; Kwak, S. K.; Oh, J. H. "Majority-Rules" Effect on Supramolecular Chirality and Optoelectronic Properties of Chiral Tetrachloro-Perylene Diimides. *Adv. Opt. Mater.* **2020,** 2001911

(21) Huang, C.; Barlow, S.; Marder, S. R. Perylene-3,4,9,10-Tetracarboxylic Acid Diimides: Synthesis, Physical Properties, and Use in Organic Electronics. *J. Org. Chem.* **2011,** *76*, 2386-2407.

(32) Liu, M.; Zhang, L.; Wang, T. Supramolecular Chirality in Self-Assembled Systems. *Chem. Rev.* **2015,** *115*, 7304-7397.

(23) Schmidt, R.; Osswald, P.; Könemann, M.; Würthner, F. Synthetic Routes to Core-Fluorinated Perylene Bisimide Dyes and Their Properties. *Z. Naturforsch. B* **2009,** *64*, 735-746.

(24) Jiang, W.; Li, Y.; Yue, W.; Zhen, Y.; Qu, J.; Wang, Z. One-Pot Facile Synthesis of Pyridyl Annelated Perylene Bisimides. *Org. Lett.* **2010,** *12*, 228-231.

(25) Oh, J. H.; Lee, H. W.; Mannsfeld, S.; Stoltenberg, R. M.; Jung, E.; Jin, Y. W.; Kim, J. M.; Yoo, J.-B.; Bao, Z. Solution-Processed, High-Performance N-Channel Organic Microwire Transistors. *Proc. Natl. Acad. Sci. USA* **2009,** *106*, 6065-6070.

(26) Marcus, R. A. On the Theory of Oxidation-Reduction Reactions Involving Electron Transfer. I. *J. Chem. Phys.* **1956,** *24*, 966-978.

(27) Hush, N. S. Adiabatic Rate Processes at Electrodes. I. Energy-Charge Relationships. *J. Chem. Phys.* **1958,** *28*, 962-972.

(28) Li, H.; Brédas, J.-L.; Lennartz, C. First-Principles Theoretical Investigation of the Electronic Couplings in Single Crystals of Phenanthroline-Based Organic Semiconductors. *J. Chem. Phys.* **2007,** *126*, 164704.

(29) Bredas J.-L.; Beljonne D.; Coropceanu, V.; Cornil, J. Charge-Transfer and Energy-Transfer Processes in π-Conjugated Oligomers and Polymers: A Molecular Picture, *Chem. Rev.* **2004**, *104*, 4971-5003.

(30) Delley, B. An All-Electron Numerical Method for Solving the Local Density Functional for Polyatomic Molecules. *J. Chem. Phys.* **1990,** *92*, 508-517.

(31) Delley, B. From Molecules to Solids with the Dmol^3 Approach. *J. Chem. Phys.* **2000,** *113*, 7756-7764.

(32) Perdew, J. P.; Burke, K.; Ernzerhof, M. Generalized Gradient Approximation Made Simple. *Phys. Rev. Lett.* **1996,** *77*, 3865-3868.

(33) Tkatchenko, A.; Scheffler, M. Accurate Molecular Van der Waals Interactions from Ground-State Electron Density and Free-Atom Reference Data. *Phys. Rev. Lett.* **2009,** *102*, 073005.

(34) Frisch, M. J.; Trucks, G. W.; Schlegel, H. B.; Scuseria, G. E.; Robb, M. A.; Cheeseman, J. R.; Scalmani, G.; Barone, V.; Petersson, G. A.; Nakatsuji, H.; Li, X.; Caricato, M.; Marenich, A. V.; Bloino, J.; Janesko, B. G.; Gomperts, R.; Mennucci, B.; Hratchian, H. P.; Ortiz, J. V.; Izmaylov, A. F.; Sonnenberg, J. L.; Williams; Ding, F.; Lipparini, F.; Egidi, F.; Goings, J.; Peng, B.; Petrone, A.; Henderson, T.; Ranasinghe, D.; Zakrzewski, V. G.; Gao, J.; Rega, N.; Zheng, G.; Liang, W.; Hada, M.; Ehara, M.; Toyota, K.; Fukuda, R.; Hasegawa, J.; Ishida, M.; Nakajima, T.; Honda, Y.; Kitao, O.; Nakai, H.; Vreven, T.; Throssell, K.; Montgomery Jr., J. A.; Peralta, J. E.; Ogliaro, F.; Bearpark, M. J.; Heyd, J. J.; Brothers, E. N.; Kudin, K. N.; Staroverov, V. N.; Keith, T. A.; Kobayashi, R.; Normand, J.; Raghavachari, K.; Rendell, A. P.; Burant, J. C.; Iyengar, S. S.; Tomasi, J.; Cossi, M.; Millam, J. M.;

Klene, M.; Adamo, C.; Cammi, R.; Ochterski, J. W.; Martin, R. L.; Morokuma, K.; Farkas, O.; Foresman, J. B.; Fox, D. J. *Gaussian 16 Rev. C.01*, Wallingford, CT, 2016.

(35) Becke, A. D. A New Mixing of Hartree–Fock and Local Density-Functional Theories. *J. Chem. Phys.* **1993,** *98*, 1372-1377.

(36) Lee, C.; Yang, W.; Parr, R. G. Development of the Colle-Salvetti Correlation-Energy Formula into a Functional of the Electron Density. *Phys. Rev. B* **1988,** *37*, 785-789.

Chapter 3

Studies on Modulation of Chirality and Optoelectronic Property in Chiral Organic Semiconductor/Polymer Blends

3. 1. Introduction

As a compelling derivative of organic field-effect transistors OFETs, OPTs have attracted increasing attention due to their various applications, including optical communications, biomedical sensing, and imaging.[1] To develop OPTs with outstanding optoelectronic parameters such as high photoresponsivity, photoswitching ratio, and detectivity, a sophisticated control over both the photoactive layer and process architecture is typically required.[2] In recent years, various OSCs have been developed to control their molecular packing and orientation in solid state toward high performance OPTs. However, the investigation into the effects of chiral OSCs on the optoelectrical performance of OPTs is still in the initial stages. Several studies have attempted to reveal the relationship between the chirality and the molecular orientation in OSC thin films. Helical homochirality and stereoisomerism are known to affect the molecular packing, leading to the change in charge carrier mobility.[3-9] However, most studies have focused on the development of bulky helicene derivatives or organic single crystals, which may not be highly suitable for practical large-scale applications due to their low charge carrier mobilities and complex device fabrication processes. To our knowledge, despite the recent rapid advances in chiral organic electronics, there is no demonstration regarding the relationship between chiral composition and optoelectronic properties in OPT applications based on chiral OSC/polymer blend system.

In order to investigate chirality-property relationship in solution-processable, high performance OSCs, I chose a versatile family of *n*-type semiconductors, PDIs, owing to their handiness for chirality induction as well as their chemical stability, high electron affinity, and tunable optoelectrical properties.[6, 10-12] Our research group reported the amplified chirality of self-assembled supramolecular structures of chiral PDIs for high-performance chiroptical sensing.[6] However, these chiral PDIs suffer from poor air stability. The instability of PDIs is not due to their intrinsic chemical stability, but rather related to their vulnerability of electron charge carriers to the

environmental oxidants, such as moisture and oxygen under ambient conditions (i.e, charge trapping), because of their energetically high-lying LUMO energy levels. Incorporation of strong electron-withdrawing core-substituents, such as chlorine or cyano groups, lowers the LUMO energy levels.[13-15] Therefore, di-cyanated PDIs (PDI-CN2) have received significant attention due to their unique combination of high electron mobility, environmental stability, solution-processability, and self-assembling properties into micro/nano materials.[16-18] PDI-CN2 has been widely used for OFETs by adopting the vacuum evaporated thin films, [16, 19-21] solution-processed thin films,[22-24] or single crystals.[25] However, there has been no systematic study on the relationship between the chiral composition and the optoelectrical property in OFETs based on a PDI-CN2 blend system.

To further enhance the photodetecting perperties of OPTs, one effective strategy is an introduction of charge-trapping effect by using a polar insulating polymer. The use of an insulating polymer via blending or bilayer processing with a photoactive material can improve the photosensitivity by suppressing the dark current effectively due to the efficient charge trapping at the insulating polymer/OSC interface.[1-2] In addition, the introduction of a polar polymer additive may enhance the surface wettability in solution process.[26] The better film-forming properties typically allow the efficient solution processing on various polymer dielectric layers or self-assembled monolayer-treated surfaces and the increase in the crystallinity and uniformity of OSC thin films, leading to the enhanced charge carrier mobility and better optoelectrical performances. By blending polymers and small molecules, fine-tuning of intermolecular interactions and molecular packing can also be achieved, affecting the overall structural characteristics of the OSC thin film, which in turn leads to the fast charge transport.[27-28] However, study on the photophysical behaviors of photogenerated charge carriers and optoelectrical properties in the chiral OSC/polymer blend system is still rare and of great importance in chiral organic electronics.

In this study, considering the aforementioned background, OPTs were fabricated by introducing enantiopure or racemic PDI derivatives (CPDI-CN2-C6) into a blend system with an insulating biopolymer, PLA. OPTs based on the CPDI-CN2-C6/PLA blend films showed greatly enhanced optoelectronic performance due to the charge-trapping effect. In particular, 75 wt% PLA-blended CPDI-CN2-C6 system exhibited a maximum P of 281 and $D^*$of 1.1×10^{12} Jones, 312 and 65 times higher than those of non-hybrid enantiopure PDI systems, respectively. In addition, 75 wt% PLA-blended *n*-type devices could tolerate ambient conditions for > 1000 h, indicating the high potential of these devices for practical applications. Furthermore, the racemic system exhibited a 12-fold increase in D^* (1.3×10^{13} Jones) when compared to the enantiopure system, implying that chiral composition can greatly affect the optoelectronic performance of OSCs. Our results demonstrate an easy and facile strategy to develop high performance *n*-type OPTs for practical applications by incorporating chirality and using various blended systems.

3.2. Results and Discussion

3.2.1. Characterization of Chiral Cyanated PDIs.

Both (*R*)- and (*S*)-CPDI-CN2-C6 were synthesized by Prof. Xiaobo Shang in Xi'an Jiaotong University as previously described.[24] The chemical structures of two small molecule OSCs and PLA are outlined (**Figure 3.1a**). The optical properties of CPDI-CN2-C6 in chloroform (CF, 1.0×10^{-4} M) were investigated using UV-vis spectrometry. Both enantiomeric/racemic forms of CPDI-CN2-C6 exhibited identical peaks at 524, 487, 456, and 428 nm, which corresponded to the 0−0, 0−1, 0−2, and 0−3 transitions of the well-resolved vibronic structure of the monomer, respectively (**Figure 3.1b**), which was characteristic electronic absorptions of perylene diimides.[29-32] To investigate the absorption spectrum in aggregated states, spin-coated pure and blended thin films were prepared on a quartz plate. When (*S*)- or (*Rac*)-CPDI-CN2-C6 was blended with 25 wt% PLA, there was a slight change in the absorption peaks when compared to CPDI-CN2-C6 alone. However, if the blending ratio was inversed to 25 wt% (*S*)- or (*Rac*)-CPDI-CN2-C6 with 75 wt% PLA, the maximum absorption peaks exhibited a remarkable hypsochromic shift from 535, 496 and 471 nm to 525, 490 and 465 nm for (*S*)- and (*Rac*)-CPDI-CN2-C6, respectively (**Figure 3.1c**), indicating that the electron withdrawing property of the PLA may affect the energy level of the CPDI-CN-C6 molecule in the blended system.[1] In addition, Franck-Condon ratio A_{0-0}/A_{0-1} decreases from 0.97 to 0.85, indicating stronger electronic coupling between PDI molecules via π–π stacking interactions.[29, 31] The energy band gap of CPDI-CN2-C6 was characterized by DFT calculation (**Figure 3.2**) and CV measurements in chloroform (1.0×10^{-4} M) (**Figure 3.3**). The LUMO energy levels of CPDI-CN2-C6 were obtained as –4.14 eV and –4.23 eV from DFT calculation and CV measurement, respectively, indicating that CPDI-CN2-C6 has the potential to be used in practical applications under ambient conditions (**Table 3.1**).[19] To examine the chiroptical properties of CPDI-CN2-C6,

CD spectra were measured in both solution and thin film conditions (**Figure 3.4**). **Figure 3.4** shows that chirality was successfully transferred from the chiral pendant to the entire aggregated film system with strong and opposite CD peaks in the UV and visible range. Furthermore, CPDI-CN2-C6 blended with 75 wt% PLA showed an amplified intensity when compared to 25 wt% PLA, owing to the different aggregated states of the thin films. The amplified intensity and CD spectra in UV range indicated that the chirality is attributed to induced chirality in the achiral polymers with the chiral molecular dopants.[33-34]

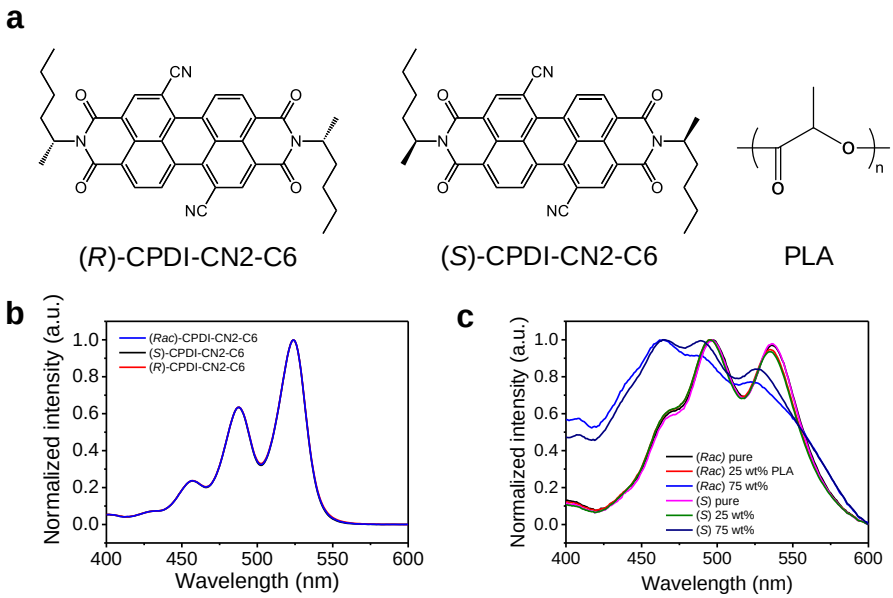

Figure 3.1. Characterizations of chiral cyanated PDIs. a, Chemical structures of (*R*)-CPDI-CN2-C6, (*S*)-CPDI-CN2-C6, and PLA. **b**–**c**, UV-vis spectra of solutions (10^{-4} M in chloroform) (**b**), and thin films containing varying compositions of enantiopure or recemate CPDI-CN2-C6 with regard to PLA (**c**).

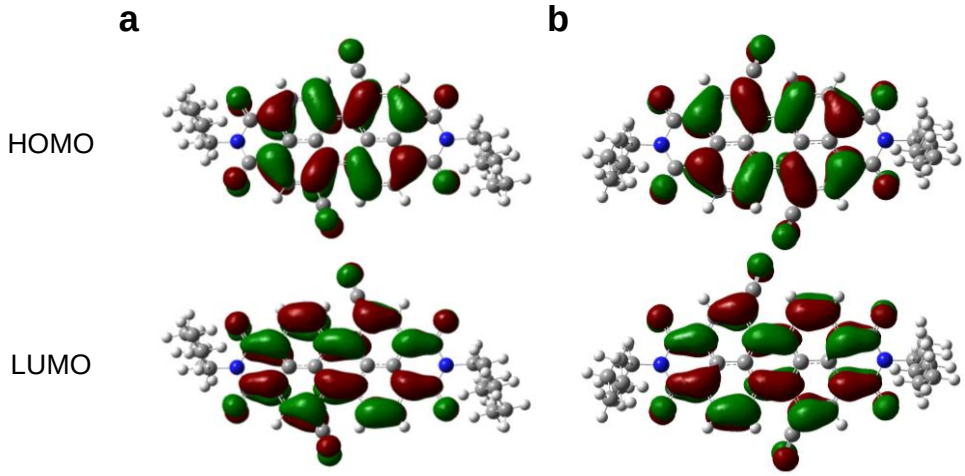

Figure 3.2. DFT calculation results of chiral cyanated PDIs. a–**b**, HOMO and LUMO electron distributions of (*R*)-CPDI-CN2-C6 (**a**), and (*S*)-CPDI-CN2-C6 (**b**).

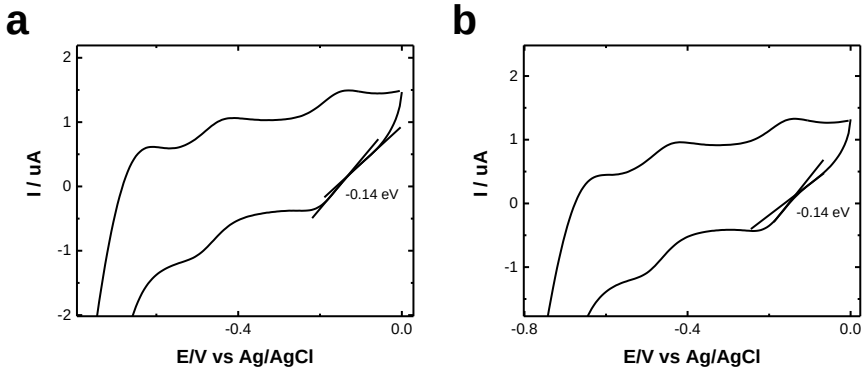

Figure 3.3. CV measurements results of chiral cyanated PDIs. a–b, Results of CV measurements from (*S*)-CPDI-CN2-C6 (**a**), and (*R*)-CPDI-CN2-C6 (**b**) solution (1.0×10^{-4} M in chloroform).

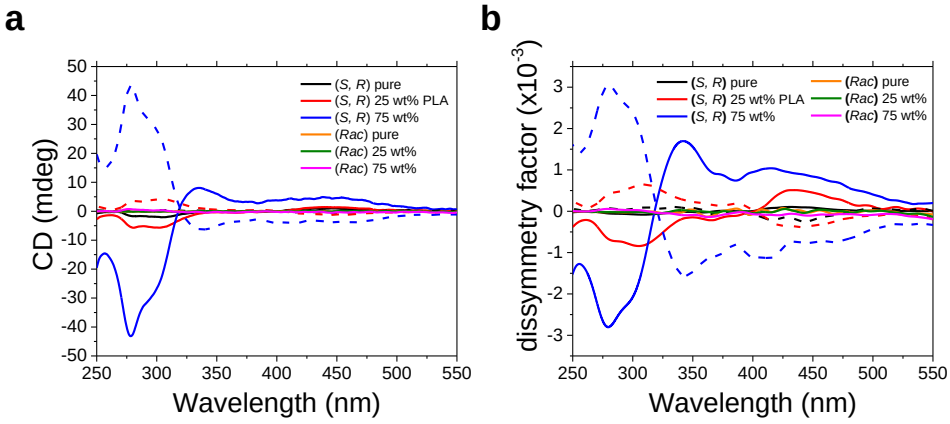

Figure 3.4. Chiroptical properties of cyanated PDIs and PLA blended system. a–b, Circular dichroism (**a**), and dissymmetry factor (**b**) results of (*S*)-CPDI-CN2-C6, (*R*)-CPDI-CN2-C6 and (*Rac*)-CPDI-CN2-C6 thin films mixed with PLA. Solid lines display result of (*S*)-CPDI-CN2-C6 and dotted lines one of (*R*)-CPDI-CN2-C6.

Table 3.1. Energy levels of enantiomeric CPDI-CN2-C6 from CV measurement and DFT calculation.

	Material	Orbital	Energy level (eV)
DFT	(*R*)-CPDI-CN2-C6	LUMO	−4.14
		HOMO	−6.60
	(*S*)-CPDI-CN2-C6	LUMO	−4.14
		HOMO	−6.61
CV	(*R*)-CPDI-CN2-C6	LUMO	−4.23
		HOMO	−6.52
	(*S*)-CPDI-CN2-C6	LUMO	−4.23
		HOMO	−6.52

3.2.2. Optoelectronic Properties of Cyanated PDIs and PLA Blended System

Within the blend system, PLA polar groups interact with OSCs and induce an interfacial charge-trapping effect. Devices were fabricated utilizing three conditions: CPDI-CN2-C6 alone, and CPDI-CN2-C6 mixed with 25 wt% and 75 wt% PLA. OPTs were fabricated with bottom-gate and top-contact transistor geometry on OTS-treated SiO_2/Si substrates. Fabrication of the CPDI-CN2-C6 film with the hydrophobic OTS-treated surface proved troublesome, therefore pure CPDI-CN2-C6-based OPTs were exclusively fabricated on hexamethyldisilazane (HMDS)-treated SiO_2/Si substrates. Transfer characteristics of fabricated OPTs are outlined (**Figure 3.5a**). From the transfer curve, the mobility at a specific gate voltage region recorded as the highest during the gate voltage sweep was extracted. In an N_2 atmosphere, pure CPDI-CN2-C6-based OPTs showed an average electron mobility of 6.8×10^{-3} cm^2 V^{-1} s^{-1} (**Table 3.2**). In contrast, CPDI-CN2-C6 blended with 25 wt% PLA showed a much higher electron mobility of 0.1 cm^2 V^{-1} s^{-1}. This change originates from the difference in the electron density, the contact quality and the low water/oxygen content of the dielectric hydrophobic self-assembled monolayer.[35-36] An advantage to this blending system is that it allows small molecule compounds to form the robust films on the hydrophobic self-assembled monolayer surface through a simple solution process by increasing the wettability. It is usually difficult to obtain thin films of uniform morphology using solution processes because of the strong dewetting nature of the low viscosity small molecule solution. The high-viscosity blending solution increases the wettability on even highly hydrophobic self-assembled monolayer surface in the same organic solvent.[37-38] However, OPTs with CPDI-CN2-C6 blended with 75 wt% PLA showed a mobility of 2.7×10^{-3} cm^2 V^{-1} s^{-1}, which was much lower than that of CPDI-CN2-C6 with 25 wt% PLA. This change is due to the induction of more traps with a larger amount of insulating PLA that can hinder charge carrier transport in the dark state. The ester group in the

insulating polymers shallowly trap the charge carriers in the conducting channels of the semiconducting films, thus reducing the charge carrier transport rate, leading to the reduced drain current in dark state and charge carrier mobilities. Furthermore, several other factors, such as longer intermolecular distances of semiconducting molecules, injection barriers at the contact, and contact resistance, might contribute to the dark current suppression. In spite of the high dark current suppression, the current hysteresis behaviors were not observed in the blended system (**Figure 3.6**). It indicates that the introduction of the insulating polymers in the blending system produces the shallow traps in the conducting channels of the semiconducting films, rather than the deep traps which greatly contribute to the bias stress.[39] To investigate the dark current suppression in the insulating polymer blending system by the shallow traps, I fabricated blended films on a HMDS treated substrate to compare with pure one by using the identical self-assembled monolayer condition. The dark current was suppressed significantly as the content of the insulating polymers increased, which indicates that the insulating polymers effectively worked as charge traps in the conducting channels (**Figure 3.7**).

To investigate the photodetecting properties of the OPTs, both the pure CPDI-CN2-C6 and blended systems were subjected to monochromatic light (λ = 465 nm) at varying illumination intensities (5, 10, 30, 50, 100, 200, 300, and 400 μW cm^{-2}). Under visible light irradiation, pure CPDI-CN2-C6-based OPTs exhibited negatively shifted threshold voltage (V_T) and enhanced current levels in transfer curves (**Figure 3.5a**). The easier turn-on observed under light irradiation originates from both exciton dissociation/separation, and an increase in charge transport, leading to enhanced photocurrent.[40] Interestingly, PLA additives (25 wt%) possess two main advantages in OPT applications: i) better charge transport using hydrophobic self-assembled monolayer processes, and ii) reduced dark current by the trap site rule of PLA chains in semiconductor systems. Under the illumination, the ability of the taps to capture charge carreirs would be reduced and saturated after a large amount of

photoexcitons are generated. The transport rate of extra photogenerated charge carriers would not be affected by the traps, thus drain current increases along with light intensity.[39] Thus, when compared with pure OSCs, 25 wt% PLA-blended devices showed enhanced photocurrents/dark currents and optoelectronic properties. PLA-blended (75 wt%) devices displayed a greater dark current reduction than 25 wt% PLA-blended devices, indicating the more trap sites present in 75 wt% than in 25 wt% thin films. In addition, I found the nonlinear transfer characteristics in the negative gate field region under the light exposure as the blended PLA ratio increased to 75 wt%. In the negative gate voltage (V_{GS}) region, holes from the photogenerated exciton transfer across the semiconductor/dielectric interface, leaving extra electrons in the transistor channel. It makes the transistor device easier to turn on. The transferred holes act as extra shallow traps to disrupt the electron transport in the semiconducting channel. In the more PLA-blended devices, there are the more extra shallow traps due to the high ratio of insulating polymer and large charge trapping nature, leading to the more nonlinear transfer characteristics.[39]

To further evaluate OPT performances, R, P, EQE, and D^* depending on gate voltage were estimated using transfer curves (**Figure 3.5b−e**). Compared to pure CPDI-CN2-C6-based OPTs, PLA-blended OPTs showed better performances in all of these parameters. For example, 25 wt% PLA-blended CPDI-CN2-C6 system exhibited maximum R of 47 A W^{-1}, P of 18, EQE of 12,562%, and D^* of 4.4×10^{11} Jones, which are 224, 20, 224, and 26 times higher than those in pure PDI systems under 300 μW cm^{-2} illumination, respectively (**Table 3.2**). The EQE values higher than 100% are attributed to the photomultiplication phenomenon by external bias in circuit. Under the light exposure, extra holes from the photogenerated exciton could be trapped at the interfaces between electrodes and photoactive materials, which results in the significant change of interfacial energy barriers from the triangle shape into a wedge shape. Then, the electrons could be easily injected from the external

circuit through the wedge shape interfacial barrier, which results in high photocurrent and EQE.[41]

Higher *R* and EQE values of PLA-blended devices originate from the enhanced photocurrent due to a decrease in H_2O/O_2 concentration and better contact with the hydrophobic self-assembled monolayer surface. This effect was stronger in 25 wt% PLA-blended systems than that in its 75 wt% counterpart because the photocurrent enhancement was optimized as there were relatively less trap sites. Furthermore, PLA-blended devices exhibited better *P* and D^* values than pure CPDI-CN2-C6-based OPTs owing to a suppression in dark current by trap site introduction. In particular, OPTs with CPDI-CN2-C6 blended with PLA 75 wt% showed a larger reduction in dark current, leading to a higher maximum *P* of 281 and D^* of 1.1×10^{12} Jones, 16 and 2.5 times higher than 25 wt% PLA-blended devices, respectively. The optoelectronic properties in OPTs could be tuned by varying the PLA additive ratio, indicating that it may be a tooling factor for on-demand optoelectronic applications.

Both CPDI-CN2-C6 alone and the blended CPDI-CN2-C6 films showed excellent air stability (**Figure 3.5f**). Devices of CPDI-CN2-C6 and 75 wt% PLA-blended films could endure over 1,000 h under ambient conditions, showing only a 10–20% reduction in their original mobility over time, outlining their great potential for practical applications. This indicated that the hindered charge-carrier transport aspect helped retain the electrical properties under ambient conditions, owing to the barrier effect against water and oxygen.

In order to investigate the photoresponse for the wide spectral range OPT applications, I also tested photoresponse under the light exposure of wavelength of 490 and 525 nm (**Figure 3.8**). I confirmed the similar photodetection ability compared to one under the light illumination of wavelength of 465 nm, which indicates that our OPT devices have strong dark current suppression and the resulting high-performance in a wide range of visible light illumination. Furthermore, I tested the linearity between the photocurrent and the power of the incident light, estimating

the linear dynamic range (LDR), which is the range in decibel (dB) of input light power over which the responsivity is constant (**Figure 3.9**). In general, the upper limit of linearity between the input irradiance and the photocurrent is defined by a deviation current, where bimolecular recombination is more dominant than a monomolecular recombination at high enough charge carrier concentration.[42] As I could not find the deviation current and any nonlinearity under irradiance up to 5 mW cm^{-2}, I estimated the measurable LDR using the upper limit and lower limit of laser installation. The LDR was calculated using the following equation:[43]

$$\mathrm{LDR} = 20 \log \frac{L_{highest}}{L_{Lowest}} = 90 \text{ dB} \quad (1)$$

where the $L_{highest}$ and L_{lowest} are the highest and lowest incident light power within the linear regime, respectively. The estimated LDR was 90 dB in spite of the limitation of laser installation. I tested transfer characteristics in the linear regimes and output characteristics to further investigate the electrical behavior of the phototransistor devices (**Figure 3.10**). The pure and small polymer blending ratio devices exhibited well-defined transfer curves with small hysteresis and threshold voltage shifts. In addition, the output curves of pure and small polymer blending ratio devices also exhibited well-defined output behavior with a prominent transition from linear to saturation behavior with increasing V_{GS}. However, I found the abnormal nature and the injection limitation in small drain bias as the polymer blending ratio increased, although the racemic devices showed relatively better electrical characteristics. It is because of the excessive charge trap effect for enhancing the photocurrent/dark current ratio significantly, which requires high voltage operation to fill extra traps in the semiconducting films.

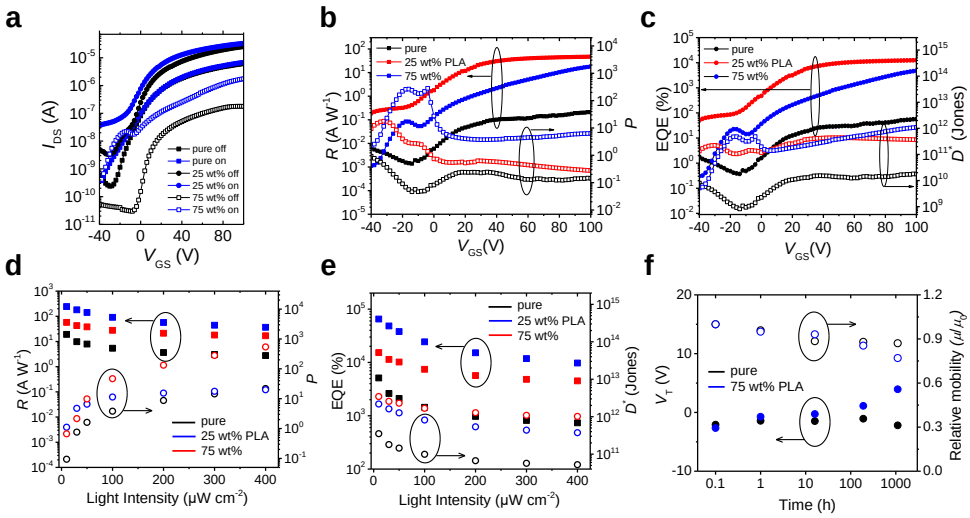

Figure 3.5. Optoelectronic properties of PLA-blended chiral cyanated PDIs based phototransistors. a, I_{DS}-V_{GS} characteristics of PLA-blended CPDI-CN2-C6 thin films with different ratio in dark and under monochromatic light illumination (λ = 465 nm) and vacuum conditions (V_{DS} = 100 V). **b**–**c**, photoresponsivity and photosensitivity (**b**), EQE and specific detectivity (**c**) of PLA-blended CPDI-CN2-C6 thin films with different blending ratios depending on gate voltage. **d**–**e**, R and P (**d**), EQE and D^* (**e**) of PLA-blended CPDI-CN2-C6 thin films with different blending ratios depending on light intensity. **f**, Changes in the threshold voltage and relative mobility of both pure CPDI-CN2-C6 and PLA-blended CPDI-CN2-C6 thin films under ambient conditions as a function of elapsed time.

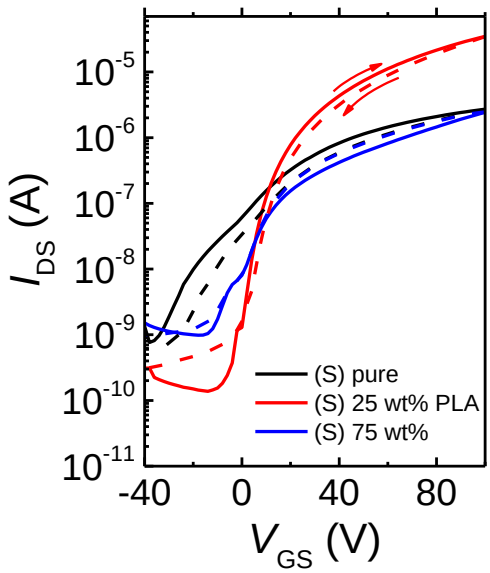

Figure 3.6. Hysteresis behaviors of PLA-blended CPDI-CN2-C6 thin films with different compositions of PLA in the dark condition.

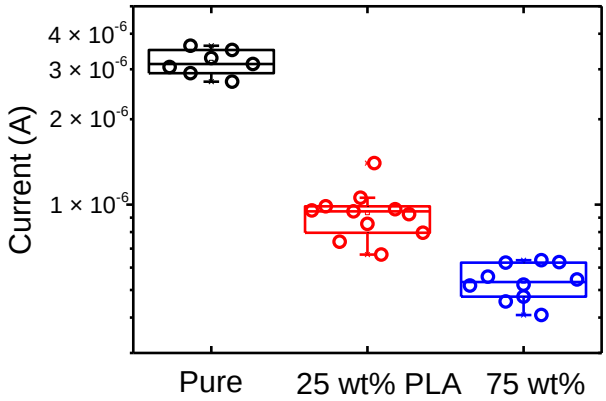

Figure 3.7. Drain current distributions of several devices depending on PLA composition. V_{GS} = 100 V, V_{DS} = 100 V.

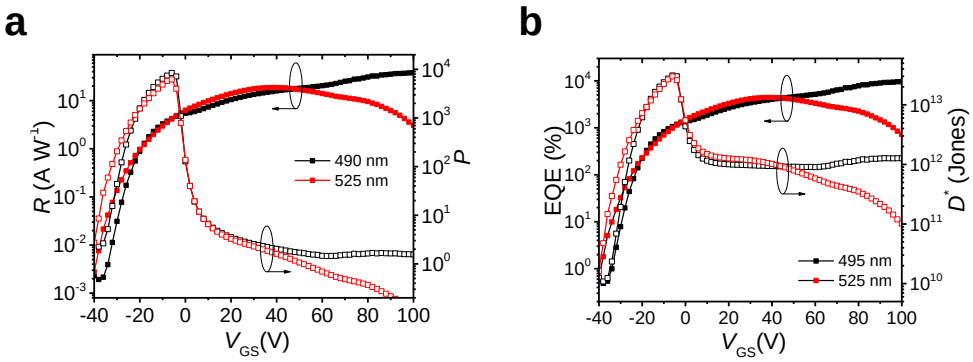

Figure 3.8. Optoelectronic properties in various wavelength region. a–b, *R* and *P* (**a**), EQE and D^* (**b**) of 75 wt% PLA-blended (*Rac*)-CPDI-CN2-C6 thin films under 490 and 525 nm light illumination.

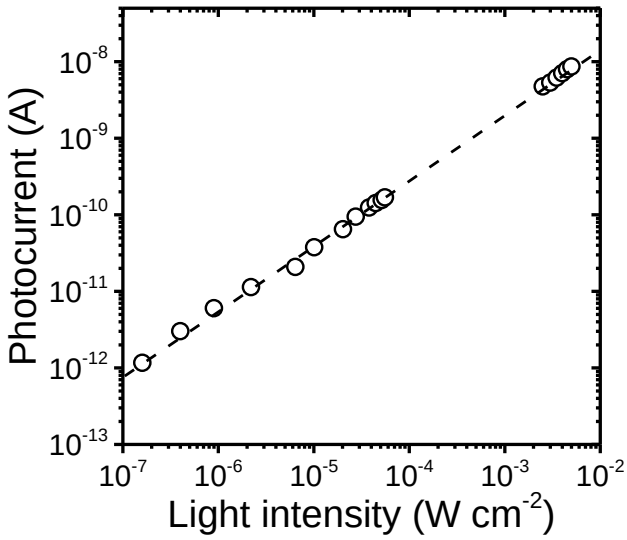

Figure 3.9. Linear dynamic range measurement result. Photocurrent of (*Rac*)-CPDI-CN2-C6 with 75 wt% PLA thin film based OPTs measured at −20 V as a function of incident light irradiance (λ = 532 nm). The irradiance was ranged from 160 nW cm^{-2} to 5 mW cm^{-2}, which was the lower and upper limit of our illumination facilities, respectively.

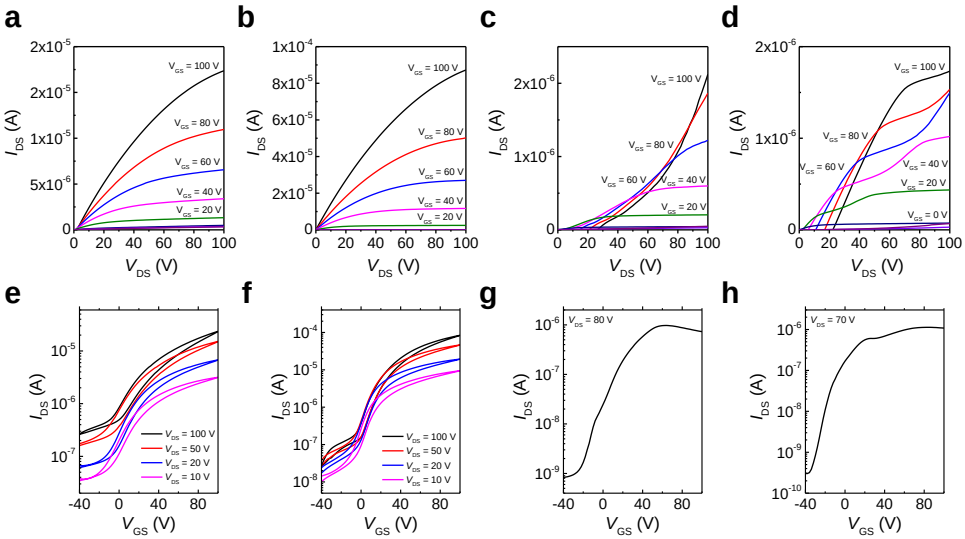

Figure 3.10. Electrical properties of phototransistors depending on PLA composition. a–d, output characteristics of pure (**a**), 25 wt% PLA-blended (**b**), 75 wt% PLA-blended (**c**) (*S*)-CPDI-CN2-C6, and 75 wt% PLA-blended (*Rac*)-CPDI-CN2-C6 (**d**). **e–h**, Transfer characteristics of pure (**e**), 25 wt% PLA-blended (**f**), 75 wt% PLA-blended (**g**) (*S*)-CPDI-CN2-C6, and 75 wt% PLA-blended (*Rac*)-CPDI-CN2-C6 (**h**) under linear regime.

Table 3.2. Optoelectronic properties of CPDI-CN2-C6 devices.

Chirality	Blending Ratio	μ (cm^2 V^{-1}s^{-1})	R [c] (A W^{-1})	P [c]	EQE [c](%)	D^* [c](Jones)
Enantiomer	Pure	6.8×10^{-3} [a] (3.9×10^{-3}) [b]	0.2	0.9	56	1.7×10^{10}
	25 wt% PLA	0.1 (1.8×10^{-2})	47	17.7	12562	4.4×10^{11}
	75 wt% PLA	2.7×10^{-3} (1.1×10^{-3})	18	281	4821	1.1×10^{12}
Racemate	75 wt% PLA	8.8×10^{-3} (2.8×10^{-3})	10	5791	2710	1.3×10^{13}

[a] Average charge carrier mobility of at least four points in more than five devices under dark condition.

[b] Standard derivation of charge carrier mobility of at least four points in more than five devices under dark condition.

[c] Maximum values obtained in the gate voltage sweep (−40 V - 100 V) under monochromic light illumination (λ = 465 nm, 300 μW cm^{-2}).

3.2.3. Phase Separation Analysis of Blended Thin Films

In order to investigate the phase separation issues in solid thin films during the solution processing, I conducted X-ray photoelectron spectroscopy (XPS). XPS was performed for the blended thin films (75 wt%) to investigate the film structure in the vertical profile. **Figure 3.11** displays the estimated relative ratio of carbon and nitrogen elements (contained in PDI molecules), as a function of vertical depth. The XPS results revealed that the insulating polymers were relatively concentrated in the middle of the film. These distributions have advantages for the follow OPT applications, because the charge carriers need to flow through the bulk film vertically (through the middle part) and the light absorption for exciton formation decreases at interfaces between the semiconducting film and the dielectric layer (bottom part). Meanwhile, the devices exhibited high gate-bias stability with small hysteresis behavior because of a small ratio of the polar polymer at the semiconductor/dielectric interfaces.

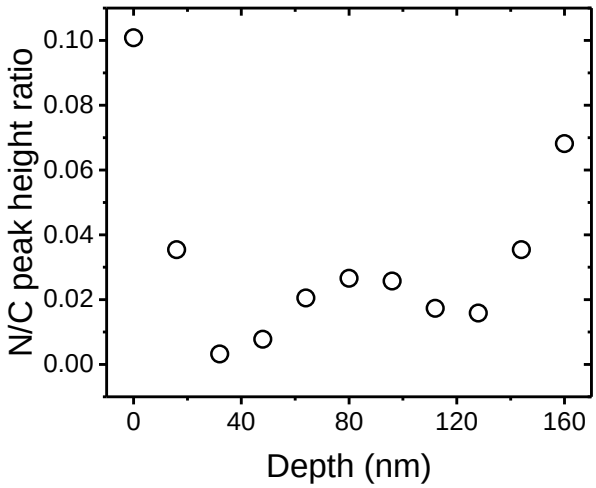

Figure 3.11. XPS characterization of 75 wt% PLA-blended film.

3.2.4. Effect of Chiral Composition on Optoelectronic Properties

To investigate the effect of chiral composition on the optoelectronic properties, I also fabricated OPTs using racemic CPDI-CN2-C6. Both (*S*)- and (*R*)-CPDI-CN2-C6 (1:1 ratio) were blended with 75 wt% PLA. Interestingly, racemic CPDI-CN2-C6 showed better performances than enantiopure OPTs. They exhibited an average electron mobility of 8.8×10^{-3} $cm^2 V^{-1}s^{-1}$, three times higher than that of enantiopure CPDI-CN2-C6-based devices (**Figure 3.12a, Table 3.2**). In addition, when subjected to monochromic light (λ = 465 nm, 300 μW cm^{-2}), the racemic OPTs P and D^* values were 5,791 and 1.3×10^{13} Jones, respectively, showing a clear enhancement over the enantiopure CPDI-CN2-C6-based OPTs ($P \approx 21$ times and $D^* \approx 12$ times) (**Figure 3.12b, c**). To further demonstrate the real-time light detection ability of our OPTs, I investigated the photoresponse upon on-and-off switching of light illumination (λ = 465 nm, 400 μW cm^{-2}) at various V_{GS} using CPDI-CN2-C6 OPTs. The results outlined in **Figure 3.12d** show the reproducibility and the reversible drain current response to the switching of light. Additionally, the OPTs exhibited tunable real-time photoresponses depending on the applied V_{GS}. The rise and decay times were estimated in the reversible photoswitching in **Figure 3.12d** and **Figure 3.13**. They exhibited a relatively slow photoresponse speed with a rise time of 5.3 s and a decay time of 22 s. There is a trade-off between the high photosensitivity and slow photoswitching speed due to the charge trapping effect. These real-time, but relatively slow tunable light detection properties can be used in several optoelectronic applications which require high-accuracy photodetection, rather than optical communications which need high frequency switching.

To elucidate the effect of the chiral composition and the insulating polymer introduction on optoelectronic performances in terms of molecular packing, I investigated the morphologies of both enantiopure and racemic CPDI-CN2-C6 thin films using tapping-mode atomic force microscopy (AFM). AFM analysis revealed the height images (2×2 μm^2 scan) of enantiopure and racemic CPDI-CN2-C6 thin

films (**Figure 3.12e, f** and **Figure 3.14**). The enantiopure blended thin films exhibited more distinct and larger grains as the insulating ratio decreased. In a higher PLA blending ratio, semiconducting small molecules have weaker intermolecular interaction between themselves, leading to the larger interfacial area between semiconductors and polar polymers and the resulting strong charge carrier trapping. Racemic films exhibited more aggregated morphologies and larger grains in the AFM analysis. These differences in thin film morphology depending on the chiral composition indicate that the individual enantiopure molecules have the stronger intermolecular interactions with the opposite chiral molecules in racemic state, leading to the more intense aggregation compared to their enantiopure part. The fewer grain boundaries and defects accompanied by larger grain sizes allow the faster charge carrier transport, leading to the easier exciton dissociation and exciton separation upon light exposure.[4, 44] Thus, it is hypothesized that chirality causes different intramolecular interactions resulting in alternative molecular packing. I can conclude that chirality can be used as an effective tuning parameter for high-performance OPTs.

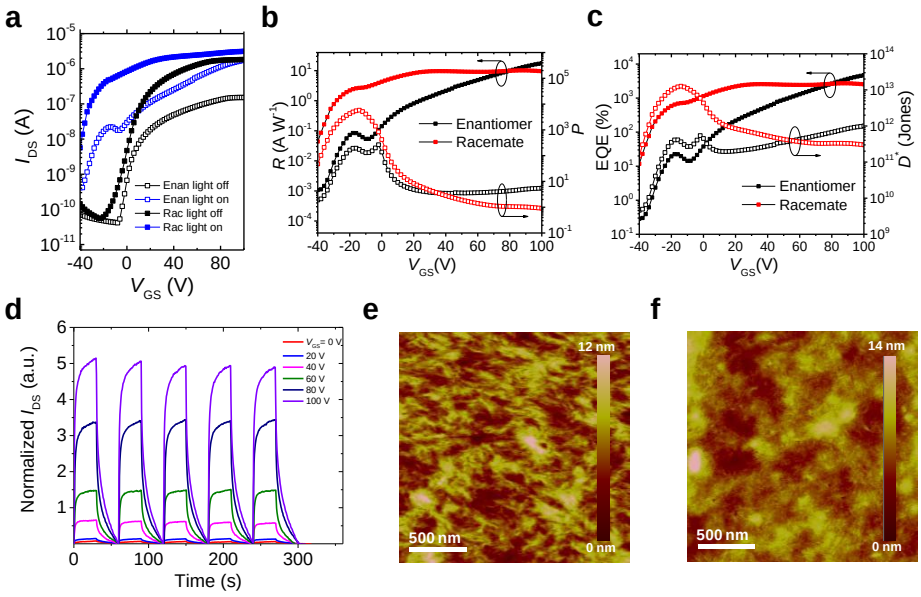

Figure 3.12. Comparison results of optoelectronic properties and morphologies depending on chiral composition. a, I_{DS}-V_{GS} characteristics of (*S*)-CPDI-CN2-C6 and (*Rac*)-CPDI-CN2-C6 thin films (75 wt% PLA) in dark and under monochromatic light illumination (λ = 465 nm) and vacuum conditions (V_{DS} = 100 V). **b**–**c**, *R* and *P* (**b**), EQE and D^* (**c**) of (*S*)-CPDI-CN2-C6 and (*Rac*)-CPDI-CN2-C6 thin films (75 wt% PLA). **d**, photoswitching of (*Rac*)-CPDI-CN2-C6 thin films (75 wt% PLA). **e**–**f**, AFM images of (*S*)-CPDI-CN2-C6 thin films (**e**) and (*Rac*)-CPDI-CN2-C6 thin films (**f**) (75 wt% PLA).

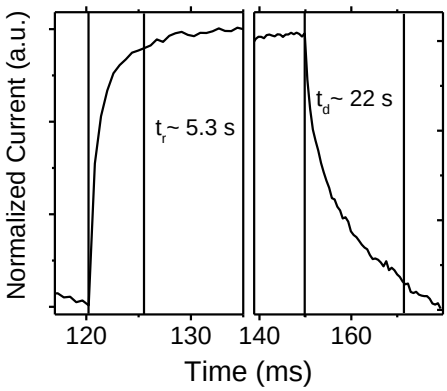

Figure 3.13. Rise/decay time of (*Rac*)-CPDI-CN2-C6 thin film based OPTs.

(V_{GS} = 40 V, V_{DS} = 100 V).

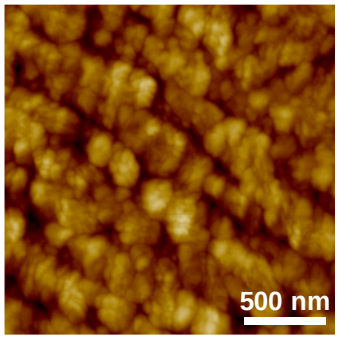

Figure 3.14. AFM images of 25 wt% PLA-blended (*S*)-CPDI-CN2-C6 film.

3. 3. Conclusion

In summary, the air-stable chiral organic semiconductor CPDI-CN2-C6 was synthesized and I systematically investigated the photoresponses of pure OSC and PLA-blended OSC systems. Compared with the pure OSC film, both the 25 and 75 wt% PLA-blended-OPTs exhibited better optoelectronic performance, owing to the efficient charge trapping at the insulating polymer/OSC interface and the resulting suppressed dark current. The maximum P and D^* of 75 wt% PLA-blended devices reached 281 and 1.1×10^{12} Jones, respectively, 312 and 65 times higher than those of unblended film, respectively. Due to the lower LUMO energy level of *n*-type CPDI-CN2-C6, both unblended and blended films showed excellent air stability. Both the pure and 75 wt% PLA-blended CPDI-CN2-C6 film exhibited 80–90% of their original mobilities when run for over 1000 h under ambient conditions, suggesting the high potential for practical application in optoelectronics. In addition, this work is the first study to investigate the effects of chirality on the photoresponses of blended photoactive systems in OPTs. Interestingly, the maximum P of 5,791 and D^* of 1.3×10^{13} Jones for the racemic blended systems were 21 and 12 times higher than those of the enantiomeric blended system, respectively. AFM analysis displayed the chiral molecules have more intense aggregation in racemic state, leading to the faster charge carrier transport and exciton dissociation/separation upon light exposure. Therefore, chirality can be utilized as a tooling parameter to tune the optoelectronic performance of OPTs. This work contributes to the investigation into the charge-trapping effects of enantiopure/racemic blended OPT systems, paving the way for the development of high-performance air-stable optoelectronics with *n*-type OSCs.

3.4. Experimental Details

3.4.1. Device Fabrication

The organic thin film transistor devices were fabricated with a bottom-gate top-contact configuration. Heavily doped silicon wafers (*n*-type, < 0.004 Ω·cm) with thermally grown 300-nm-thick SiO_2 (C_i = 11.5 nF cm^{-2}) were used as substrates for gate and gate dielectric layer, respectively. The SiO_2/Si wafers were cleaned with piranha solution for 1 h (a mixture of 70 vol% H_2SO_4 and 30 vol% H_2O_2), followed by UV-ozone treatment. The surface of the wafers was treated with OTS or HMDS self-assembled monolayer. The wafers were sequentially washed with toluene, acetone and isopropyl alcohol, and dried with nitrogen blowing. A solution containing both CPDI-CN2-C6 and PLA was prepared in chloroform (0.5 wt%) and spin-coated on the substrate (40 nm for pure and 25wt% PLA mixed films, and 160 nm for 75wt% PLA mixed films). As source and drain electrodes, gold electrodes (40 nm) were deposited by thermal evaporation through a shadow mask. The source/drain patterns had a channel length (L) of 50 μm and a channel width (W) of 1000 μm (W/L = 20).

3.4.2. Material Analysis

The UV-vis spectra were obtained using a Cary 5000 UV-vis-NIR spectrophotometer for thin film and solution. The CD spectra were measured using a *J*-815 Spectropolarimeter (JASCO). For UV-vis and CD measurements, CPDI-CN2-C6 were dissolved in chloroform (CF, 1.0×10^{-4} M) for solution samples. For solid samples, solution containing both CPDI-CN2-C6 and PLA was prepared in chloroform (0.5 wt%) and spin-coated on the quartz plate. DFT calculations were obtained with Gaussian 09 package. Cyclic voltammetric measurements were performed using a three-electrode cell with a polished 2 mm glassy carbon as working electrode, Pt as counter electrode, and Ag/$AgNO_3$ as reference electrode;

solutions in chloroform were 1×10^{-4} M for CPDI-CN2-C6 and 0.1 M for supporting electrolyte, tetrabutylammonium hexafluorophosphate. In order to calculate the LUMO levels, the redox data were standardized to the ferrocene/ferrocenium couple having a calculated absolute energy of −4.8 eV, using the following equation (1). The HOMO levels were calculated by adding the optical band gap which was obatained from UV-vis spectra to the LUMO levels.

$$E_{LUMO} = -((E_{onset,red} - E_{1/2(Ferrocene)}) + 4.8) \ \ [eV] \qquad (2)$$

3.4.3. Optoelectronic Measurement

The current-voltage characteristics of the OPTs were measured under vacuum condition (< 5.0×10^{-5} torr), by using a Keithley 4200-SCS semiconductor parametric analyzer. In OPT measurements, monochromatic light was produced using an 300W Xenon lamp and Oriel Cornerstone 130 monochromator with dual gratings. 280 μm slits were used for bandwidth of 3.7 nm.

3.4.4. Atomic Force Microscopy

AFM topographic images (2 μm × 2 μm) were obtained using a MultiMode 8 scanning probe microscope with a Nanoscope V controller.

3.5. References

(1) Huang, J.; Du, J.; Cevher, Z.; Ren, Y.; Wu, X.; Chu, Y. Printable and Flexible Phototransistors Based on Blend of Organic Semiconductor and Biopolymer. *Adv. Funct. Mater.* **2017,** *27*, 1604163.

(2) Chu, Y.; Wu, X.; Lu, J.; Liu, D.; Du, J.; Zhang, G.; Huang, J. Photosensitive and Flexible Organic Field-Effect Transistors Based on Interface Trapping Effect and Their Application in 2d Imaging Array. *Adv. Sci.* **2016,** *3*, 1500435.

(3) Hatakeyama, T.; Hashimoto, S.; Oba, T.; Nakamura, M. Azaboradibenzo[6]Helicene: Carrier Inversion Induced by Helical Homochirality. *J. Am. Chem. Soc.* **2012,** *134*, 19600-19603.

(4) Yang, Y.; Rice, B.; Shi, X.; Brandt, J. R.; Correa da Costa, R.; Hedley, G. J.; Smilgies, D.-M.; Frost, J. M.; Samuel, I. D. W.; Otero-de-la-Roza, A.; Johnson, E. R.; Jelfs, K. E.; Nelson, J.; Campbell, A. J.; Fuchter, M. J. Emergent Properties of an Organic Semiconductor Driven by Its Molecular Chirality. *ACS Nano* **2017,** *11*, 8329-8338.

(5) Liu, J.; Zhang, Y.; Phan, H.; Sharenko, A.; Moonsin, P.; Walker, B.; Promarak, V.; Nguyen, T.-Q. Effects of Stereoisomerism on the Crystallization Behavior and Optoelectrical Properties of Conjugated Molecules. *Adv. Mater.* **2013,** *25*, 3645-3650.

(6) Shang, X.; Song, I.; Ohtsu, H.; Lee, Y. H.; Zhao, T.; Kojima, T.; Jung, J. H.; Kawano, M.; Oh, J. H. Supramolecular Nanostructures of Chiral Perylene Diimides with Amplified Chirality for High-Performance Chiroptical Sensing. *Adv. Mater.* **2017,** *29*, 1605828.

(7) He, T.; Leowanawat, P.; Burschka, C.; Stepanenko, V.; Stolte, M.; Würthner, F. Impact of 2-Ethylhexyl Stereoisomers on the Electrical Performance of Single-Crystal Field-Effect Transistors. *Adv. Mater.* **2018,** *30*, 1804032.

(8) Jiang, H.; Jiang, Y.; Han, J.; Zhang, L.; Liu, M. Helical Nanostructures: Chirality Transfer and a Photodriven Transformation from Superhelix to Nanokebab. *Angew. Chem. Int. Ed.* **2019,** *58*, 785-790.

(9) Liu, Y.; Wang, C.; Guo, Y.; Ma, L.; Zhou, C.; Liu, Y.; Zhu, L.; Li, X.; Zhang, M.; Zhao, G. New Lead Bromide Chiral Perovskites with Ultra-Broadband White-Light Emission. *J. Mater. Chem. C* **2020,** *8*, 5673-5680.

(10) Huang, C.; Barlow, S.; Marder, S. R. Perylene-3,4,9,10-Tetracarboxylic Acid Diimides: Synthesis, Physical Properties, and Use in Organic Electronics. *J. Org. Chem.* **2011,** *76*, 2386-2407.

(11) Shang, X.; Song, I.; Ohtsu, H.; Tong, J.; Zhang, H.; Oh, J. H. Morphogenesis and Optoelectronic Properties of Supramolecular Assemblies of Chiral Perylene Diimides in a Binary Solvent System. *Sci. Rep.* **2017,** *7*, 5508.

(12) Shang, X.; Song, I.; Lee, J. H.; Han, M.; Kim, J. C.; Ohtsu, H.; Ahn, J.; Kwak, S. K.; Oh, J. H. Tuning the Supramolecular Chirality and Optoelectronic Performance of Chiral Perylene Diimide Nanowires Via N-Substituted Side Chain Engineering. *J. Mater. Chem. C* **2019,** *7*, 8688-8697.

(13) Dong, H.; Fu, X.; Liu, J.; Wang, Z.; Hu, W. 25th Anniversary Article: Key Points for High-Mobility Organic Field-Effect Transistors. *Adv. Mater.* **2013,** *25*, 6158-6183.

(14) Oh, J. H.; Suraru, S. L.; Lee, W.-Y.; Könemann, M.; Höffken, H. W.; Röger, C.; Schmidt, R.; Chung, Y.; Chen, W.-C.; Würthner, F.; Bao, Z. High-Performance Air-Stable N-Type Organic Transistors Based on Core-Chlorinated Naphthalene Tetracarboxylic Diimides. *Adv. Funct. Mater.* **2010,** *20*, 2148-2156.

(15) Lee, W.-Y.; Oh, J. H.; Suraru, S.-L.; Chen, W.-C.; Würthner, F.; Bao, Z. High-Mobility Air-Stable Solution-Shear-Processed N-Channel Organic Transistors Based on Core-Chlorinated Naphthalene Diimides. *Adv. Funct. Mater.* **2011,** *21*, 4173-4181.

(16) Jones, B. A.; Facchetti, A.; Wasielewski, M. R.; Marks, T. J. Effects of Arylene Diimide Thin Film Growth Conditions on N-Channel Ofet Performance. *Adv. Funct. Mater.* **2008,** *18*, 1329-1339.

(17) Huang, Y.; Fu, L.; Zou, W.; Zhang, F.; Wei, Z. Ammonia Sensory Properties Based on Single-Crystalline Micro/Nanostructures of Perylenediimide Derivatives: Core-Substituted Effect. *J. Phys. Chem. C* **2011,** *115*, 10399-10404.

(18) Huang, Y.; Zhang, W.; Wang, J.; Fu, L.; Shi, J. Electron-Withdrawing Groups Induced Remarkable Changes in Sensory Property Based on Single Micro/Nanostructure of Perylenediimide Derivatives. *Mater. Chem. Phys.* **2015,** *151*, 93-98.

(19) Oh, J. H.; Sun, Y.-S.; Schmidt, R.; Toney, M. F.; Nordlund, D.; Könemann, M.; Würthner, F.; Bao, Z. Interplay between Energetic and Kinetic Factors on the Ambient Stability of N-Channel Organic Transistors Based on Perylene Diimide Derivatives. *Chem. Mater.* **2009,** *21*, 5508-5518.

(20) Weitz, R. T.; Amsharov, K.; Zschieschang, U.; Villas, E. B.; Goswami, D. K.; Burghard, M.; Dosch, H.; Jansen, M.; Kern, K.; Klauk, H. Organic N-Channel Transistors Based on Core-Cyanated Perylene Carboxylic Diimide Derivatives. *J. Am. Chem. Soc.* **2008,** *130*, 4637-4645.

(21) Liscio, F.; Milita, S.; Albonetti, C.; D'Angelo, P.; Guagliardi, A.; Masciocchi, N.; Della Valle, R. G.; Venuti, E.; Brillante, A.; Biscarini, F. Structure and Morphology of Pdi8-Cn2 for N-Type Thin-Film Transistors. *Adv. Funct. Mater.* **2012,** *22*, 943-953.

(22) Jones, B. A.; Ahrens, M. J.; Yoon, M.-H.; Facchetti, A.; Marks, T. J.; Wasielewski, M. R. High-Mobility Air-Stable N-Type Semiconductors with Processing Versatility: Dicyanoperylene-3,4:9,10-Bis(Dicarboximides). *Angew. Chem. Int. Ed.* **2004,** *43*, 6363-6366.

(23) Ferlauto, L.; Liscio, F.; Orgiu, E.; Masciocchi, N.; Guagliardi, A.; Biscarini, F.; Samorì, P.; Milita, S. Enhancing the Charge Transport in Solution-Processed Perylene Di-Imide Transistors Via Thermal Annealing of Metastable Disordered Films. *Adv. Funct. Mater.* **2014,** *24*, 5503-5510.

(24) Vladimirov, I.; Kellermeier, M.; Geßner, T.; Molla, Z.; Grigorian, S.; Pietsch, U.; Schaffroth, L. S.; Kühn, M.; May, F.; Weitz, R. T. High-Mobility, Ultrathin Organic Semiconducting Films Realized by Surface-Mediated Crystallization. *Nano Lett.* **2018,** *18*, 9-14.

(25) Molinari, A. S.; Alves, H.; Chen, Z.; Facchetti, A.; Morpurgo, A. F. High Electron Mobility in Vacuum and Ambient for Pdif-Cn2 Single-Crystal Transistors. *J. Am. Chem. Soc.* **2009,** *131*, 2462-2463.

(26) Pitsalidis, C.; Pappa, A. M.; Hunter, S.; Laskarakis, A.; Kaimakamis, T.; Payne, M. M.; Anthony, J. E.; Anthopoulos, T. D.; Logothetidis, S. High Mobility Transistors Based on Electrospray-Printed Small-Molecule/Polymer Semiconducting Blends. *J. Mater. Chem. C* **2016,** *4*, 3499-3507.

(27) Smith, J.; Zhang, W.; Sougrat, R.; Zhao, K.; Li, R.; Cha, D.; Amassian, A.; Heeney, M.; McCulloch, I.; Anthopoulos, T. D. Solution-Processed Small Molecule-Polymer Blend Organic Thin-Film Transistors with Hole Mobility Greater Than 5 Cm2/Vs. *Adv. Mater.* **2012,** *24*, 2441-2446.

(28) Kang, B.; Ge, F.; Qiu, L.; Cho, K. Effective Use of Electrically Insulating Units in Organic Semiconductor Thin Films for High-Performance Organic Transistors. *Adv. Electron. Mater.* **2017,** *3*, 1600240.

(29) Sung, J.; Kim, P.; Fimmel, B.; Würthner, F.; Kim, D. Direct Observation of Ultrafast Coherent Exciton Dynamics in Helical Π-Stacks of Self-Assembled Perylene Bisimides. *Nat. Commun.* **2015,** *6*, 8646.

(30) Oleson, A.; Zhu, T.; Dunn, I. S.; Bialas, D.; Bai, Y.; Zhang, W.; Dai, M.; Reichman, D. R.; Tempelaar, R.; Huang, L.; Spano, F. C. Perylene Diimide-Based Hj- and Hj-Aggregates: The Prospect of Exciton Band Shape Engineering in Organic Materials. *J. Phys. Chem. C* **2019,** *123*, 20567-20578.

(31) Singh, P.; Mittal, L. S.; Singh, H.; Bhargava, G.; Kumar, S. Perylene Diimide-Based Organic Π-Motif for Differentiating Cn− and F− Ions by Electron-Transfer and Desilylation Mechanisms: Applications to Complex Logic Circuits. *New J. Chem.* **2017,** *41*, 10281-10290.

(32) Ozdal, D.; Aydinlik, N. P.; Bodapati, J. B.; Icil, H. Self-Assembly, Optical, Thermal and Electrochemical Properties of Bis-N-Benzyl Perylene Diimide Dye. *Photochem. Photobiol. Sci.* **2017,** *16*, 262-270.

(33) Kim, N. Y.; Kyhm, J.; Han, H.; Kim, S. J.; Ahn, J.; Hwang, D. K.; Jang, H. W.; Ju, B.-K.; Lim, J. A. Chiroptical-Conjugated Polymer/Chiral Small Molecule Hybrid Thin Films for Circularly Polarized Light-Detecting Heterojunction Devices. *Adv. Funct. Mater.* **2019,** *29*, 1808668.

(34) Lee, D.-M.; Song, J.-W.; Lee, Y.-J.; Yu, C.-J.; Kim, J.-H. Control of Circularly Polarized Electroluminescence in Induced Twist Structure of Conjugate Polymer. *Adv. Mater.* **2017,** *29*, 1700907.

(35) Briseno, A. L.; Mannsfeld, S. C. B.; Jenekhe, S. A.; Bao, Z.; Xia, Y. Introducing Organic Nanowire Transistors. *Mater. Today* **2008,** *11*, 38-47.

(36) Oh, J. H.; Lee, H. W.; Mannsfeld, S.; Stoltenberg, R. M.; Jung, E.; Jin, Y. W.; Kim, J. M.; Yoo, J.-B.; Bao, Z. Solution-Processed, High-Performance N-Channel Organic Microwire Transistors. *Proc. Natl. Acad. Sci. USA* **2009,** *106*, 6065-6070.

(37) Shin, N.; Kang, J.; Richter, L. J.; Prabhu, V. M.; Kline, R. J.; Fischer, D. A.; DeLongchamp, D. M.; Toney, M. F.; Satija, S. K.; Gundlach, D. J.; Purushothaman, B.; Anthony, J. E.; Yoon, D. Y. Vertically Segregated Structure and Properties of Small Molecule–Polymer Blend Semiconductors for Organic Thin-Film Transistors. *Adv. Funct. Mater.* **2013,** *23*, 366-376.

(38) Kang, M.; Hwang, H.; Park, W.-T.; Khim, D.; Yeo, J.-S.; Kim, Y.; Kim, Y.-J.; Noh, Y.-Y.; Kim, D.-Y. Ambipolar Small-Molecule:Polymer Blend Semiconductors for Solution-Processable Organic Field-Effect Transistors. *ACS Appl. Mater. Interfaces* **2017,** *9*, 2686-2692.

(39) Wu, X.; Chu, Y.; Liu, R.; Katz, H. E.; Huang, J. Pursuing Polymer Dielectric Interfacial Effect in Organic Transistors for Photosensing Performance Optimization. *Adv. Sci.* **2017,** *4*, 1700442.

(40) Samanta, S. K.; Song, I.; Yoo, J. H.; Oh, J. H. Organic N-Channel Transistors Based on [1]Benzothieno[3,2-B]Benzothiophene–Rylene Diimide Donor–Acceptor Conjugated Polymers. *ACS Appl. Mater. Interfaces* **2018,** *10*, 32444-32453.

(41) Zhao, Z.; Li, C.; Shen, L.; Zhang, X.; Zhang, F. Photomultiplication Type Organic Photodetectors Based on Electron Tunneling Injection. *Nanoscale* **2020,** *12*, 1091-1099.

(42) Street, R. A.; Schoendorf, M.; Roy, A.; Lee, J. H. Interface State Recombination in Organic Solar Cells. *Phys. Rev. B* **2010,** *81*, 205307.

(43) Yang, B.; Li, Y.-J.; Tang, Y.-X.; Mao, X.; Luo, C.; Wang, M.-S.; Deng, W.-Q.; Han, K.-L. Constructing Sensitive and Fast Lead-Free Single-Crystalline Perovskite Photodetectors. *J. Phys. Chem. Lett.* **2018,** *9*, 3087-3092.

(44) Chen, M.; Li, J.; Jiao, X.; Yang, X.; Wu, W.; McNeill, C. R.; Gao, X. Enantiopure Versus Racemic Naphthalene Diimide-Based N-Type Organic Semiconductors: Effect on Charge Transport. *J. Mater. Chem. C* **2019,** *7*, 2659-2665.

Chapter 4

Studies on Highly Dissymmetric Supramolecular Organic Chiroptical Systems and Their Applications

4. 1. Introduction

Interaction between an electromagnetic field and chiral matter was originally envisioned by S. Wiesner as a path to quantum cryptography.[1] However, its practical realization with circularly polarized light pipes remains problematic due to insufficient sensitivity and accuracy of polarization detection and different often protocols using single photon sources became more common. The spin angular momentum (SAM) generated in a circularly polarized (CP) beam must dissymmetrically interact with chiral matter as determined by polarization helicity and the bounded value $\boldsymbol{S} = \pm \hbar$ per photon for right-handed circular polarized (RCP) and left-handed circular polarized (LCP) beams.[2] The use of SAM for quantum computation/networking and information storage has attracted considerable attention[3], but the optical control and direct readout of spin information into an electric signal remains the key barrier in implementation of this technology.

Extensive theoretical and experimental studies have shown that properly designed mirror asymmetric surfaces and materials should lead to polarization-dependent photocurrent when CP light is reflected or transmitted.[4-8] Most recent research in this area was concentrated on metastructures or thick chiral mirrors that could result in high polarization rotation. However, such type of metamaterials requires expensive and low-throughput electron beam processing and a highly sophisticated optical design to match the light propagation direction to the optical axis of the chiral medium. Furthermore, they are not readily compatible with on-chip manufacturing technologies and the photocurrent output is strongly angle-dependent.[7-8]

Recently, the direct readout of SAM have been realized using circularly polarized plane waves.[9-13] In a homogeneous medium, the differential absorption of CP radiation is determined by the magnitude and direction of the electric transition dipole ($\boldsymbol{\mu}$) and magnetic transition dipole ($\boldsymbol{m}$) upon electronic excitation. CD is reinforced at increased $|\boldsymbol{m}|/|\boldsymbol{\mu}|$; thus, electric-dipole *forbidden* and magnetic-dipole *allowed* transitions show strong chiroptical activity,[14-15] but the overall absorption

coefficient of the matter remains extremely limited.[16] Accordingly, there is strong demand to utilize chirality in multiple scale of highly polarizable organic or inorganic structures to go beyond molecular-scale chiroptical responses to overcome this trade-off in chiroptical activity.

Here, I report an efficient method to fabricate a highly dissymmetric homochiral active layer using supramolecular helical ordering of conjugated polymers that displays the chirality at molecular, nanometer and submicron scales while providing highly polarizable electrons. This homogeneous spin-sensitive photoactive medium enables sensitive and accurate CP detection via long-range chiral activity in the supramolecular structure, which eliminates the need for elaborate optical designs and elements. It results in extraordinary CD and photon spin-electronic charge conversion with excellent accordance in range of highest *g* values of 1.2. Finally, the real-time spatiotemporal visualization of CP polarization in the visible range using a multiplex chiroptical sensing matrix was demonstrated.

4.2. Results and Discussion

4.2.1. Strategy for Highly Dissymmetric Chiral Single-Layered Flm

A diverse set of optoelectronic conjugated organic semiconductors, namely, poly(3-hexylthiophene-2,5-diyl) (P3HT), poly(9,9-dioctylfluorene-alt-bithiophene) (F8T2), poly[2,6-(4,4-bis(2-ethylhexyl)-4H-cyclopenta-[2,1-b:3,4-b']dithiophene-alt-4,7-bis(thiophen-2-yl)benzo-2,1,3-thiadiazole] (PCPDTTBTT), poly{2,2'-[(2,5-bis(2-octyldodecyl)-3,6-dioxo-2,3,5,6-tetrahydropyrrolo[3,4-c]pyrrole-1,4-diyl)dithiophene-5,5'-diyl-alt-thieno[3,2-b]thiophen-2,5-diyl} (PDBT-co-TT), poly[2-methoxy-5-(2'-ethylhexyloxy)-1,4-phenylene vinylene] (MEH-PPV), and poly[4,8-bis(5-(2-ethylhexyl)thiophen-2-yl)benzo[1,2-b;4,5-b']dithiophene-2,6-diyl-alt-(4-(2-ethylhexyl)-3-fluorothieno[3,4-b]thiophene-)-2-carboxylate-2-6-diyl)] (PTB7-Th) were blended with chiral additives, namely, 1,1′-Binaphthyl-2,2′-diamine ((*R*)- or (*S*)-BN), (13bR)-5,6-dihydro-5-(trans-4-propylcyclohexyl)-4H-dinaphtho[2,1-f:1',2'-h][1,5]dioxonin (R5011 or S5011), (2,2-dimethyl-1,3-dioxolane-4,5-diyl)bis(diphenylmethanol) ((*R*, *R*)- or (*S*, *S*)-TADDOL), (R)- or (S)-2-octyl 4-[4-(hexyloxy)benzoyloxy]benzoate (R811 or S811), 2-amino-3-mercaptopropionic acid (*L*- or *D*-cysteine), and 4'-[(S)-2-methylbutyl]biphenyl-4-carbonitrile (CB15), which were previously used as chiral active layers[17-22] was tested in the onset of this study. The molecular structures of the various conjugated polymers and chiral additives used to fabricate the homochiral active layers are provided in **Figure 4.1**, and **4.2**. All solutions were spin-coated on quartz plates for CD and UV-vis spectroscopic analyses; the results of the as-cast and thermally annealed films are compared in **Figure 4.3-9**. As expected, the fluorene-based conjugated polymer exhibited a strong CD activity when the chiral additives were blended in. Unanticipated CD bands were observed in the films of PCPDTTBTT. The CPDT-based polymer displayed a strong and distinct Cotton effect when doped

with (*S*)-BN, CB15, R811, (*S, S*)-TADDOL, and S5011. Chain rearrangement by thermal treatment at temperatures above the mesophase transition temperature induced significant chiroptical activities in both conjugated polymer-based thin films. Thus, the films with strong CD bands also showed a large Cotton effect in the absorption region of the solid-state conjugated polymeric films, regardless of the chiral dopants. This behavior is indicative of chirality transfer from chiral small molecule additives to entire active layer systems. The CPDT-based polymer doped with R5011 or S5011 exhibited unusual chiroptical properties, presumably because of the large helical twisting powers of R5011 and S5011, as well as efficient intermolecular interactions between the polymer and additives.[22] The impressive chirality transfer and amplification in π–π* transitions suggest high-performance broadband applications with strong electric dipole-allowed transitions (i.e., large absorption coefficient).

In contrast, negligible changes in CD spectra were observed with other conjugated polymeric films. Several semiconductor–additive combinations exhibited weak Cotton effect (i.e., P3HT with (*S*)-BN and R5011, MEH-PPV with (*S*)-BN and S5011, PDBT-co-TT with (*S*)-BN, CB15 and S5011, and PTB7-Th with (*S*)-BN, CB15 and S5011), but their chiroptical activities were very weak (< 100 mdeg) when compared with the aforementioned strong CD-effective films. Moreover, the CD-effective range was localized to the molecular electronic transition of chiral small molecule additives; it disappeared after thermal treatment at temperatures above the glass transition temperature (T_g) of the semiconductors because of chiral additive sublimation. This localization was caused by chiroptical effects that originated from intramolecular magneto-electric dipole coupling or weak intermolecular excitonic coupling in only partially twisted stacked chiral additive molecules; it indicated that the chiral additives could not induce π-conjugated semiconducting chromophores to contain any helical or twisted (i.e., chiral) arrangement for chiral excitonic coupling in major π–π^* transitions.

To overcome theoretical limitations between oscillator strength and rotational strength in atom, molecule, or chromophore, I proposed to construct the highly dissymmetric homochiral active layer by incorporating 1-dimensional supramolecular helical ordering of conjugated polymers. As such, a chiral templating using volatile enantiomer calcination generates efficient intrachain oblique stacks of chromophores and strong interchromophore coupling, even with presence of charge acceptor unit, [6,6]-Phenyl-C71-butyric acid methyl ester ($PC_{70}BM$) (**Figure 4.10a**). I hypothesize that a long-range, interchromophore chiral activities can generate asymmetric, chiral exciton coupling in strongly affected electric-dipole *allowed* transition, which ensures a Davydov splitting of excitation energy and rotational strength between the chirally arranged chromophores. These chiral media enable a dissymmetric interaction with SAM of photons through true optical activities, with zero differential reflectance or polarizance as well as constant CD and spin-current conversion of photons propagating in diverse oblique paths. As illustrated in **Figure 4.10b**, the homogeneous chiral media without any linear anisotropic properties can exhibit delicate extraction of polarization helicity information in unknown elliptically polarized beams.[13] Furthermore, an unambiguous, broadband trajectory visualization of spin sate of light beam can be demonstrated in real-time spatiotemporal imaging in on-chip manufacture device even omitting elaborate optic design and elements (i.e., oblique incidence angle and tuning of narrow working wavelength bandwidth).

I investigated differences in molecular packing or orientation phenomena in the solid state (**Figure 4.11**). The as-cast polymer films manifested featureless structures because of weak and short-range molecular ordering. Pronounced birefringent textures were observed in the annealed films of F8T2 and PCPDTTBTT. Both films exhibited distinct birefringent textures that were significantly affected by chain rearrangement during the thermal treatment, leading to highly crystalline and long-range molecular ordering. This result strongly indicated that the significant

chiroptical activities caused by chiral additives emerged with supramolecular and long-range molecular ordering beyond simple π–π interactions.

Both conjugated polymers exhibited very intense CD bands in their respective absorption ranges. However, PCPDTTBTT displayed broadband UV-vis and CD spectra with a more red-shifted absorption edge at ~800 nm. Fluorene-based polymers are frequently used in luminescence devices, rather than photon-absorbing devices, because of their high quantum yield and fast radiative recombination;[22-25] these properties contrast with the CPDT-based conjugated polymers used in solar cells and photodetector devices.[26-28] Therefore, I fabricated the intrinsic chiral active layer using the CPDT-based conjugated polymer for broadband CP detection and explored the corresponding extraordinary chiroptical activities and SAM detection device physics, with the intention to use them in real-time spin imaging prototype devices.

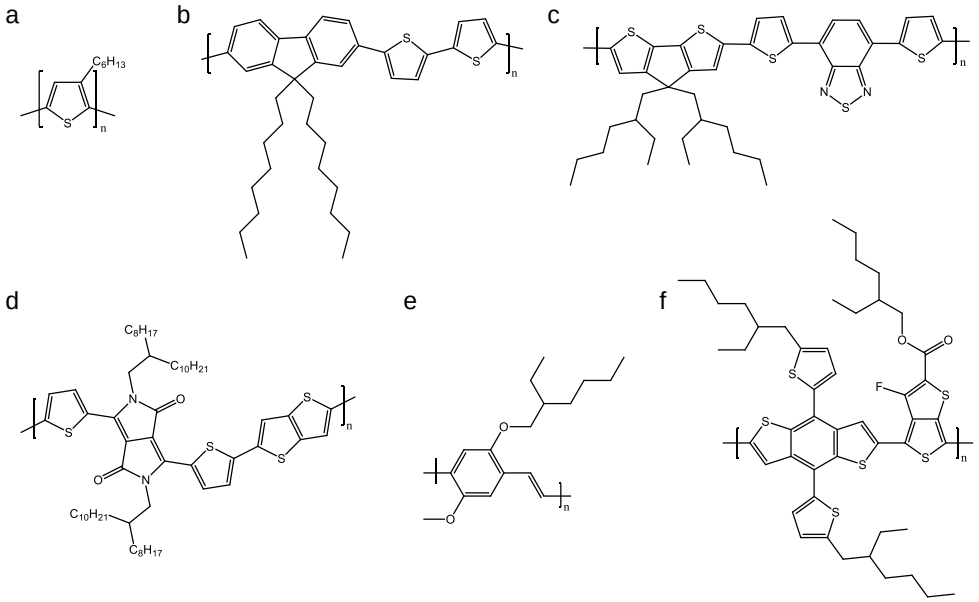

Figure 4.1. Molecular structures of various conjugated polymers. a–f, Molecular structures of P3HT (**a**), F8T2 (**b**), PCPDTTBTT (**c**), PDBT-co-TT (**d**), MEH-PPV (**e**), and PTB7-Th (**f**).

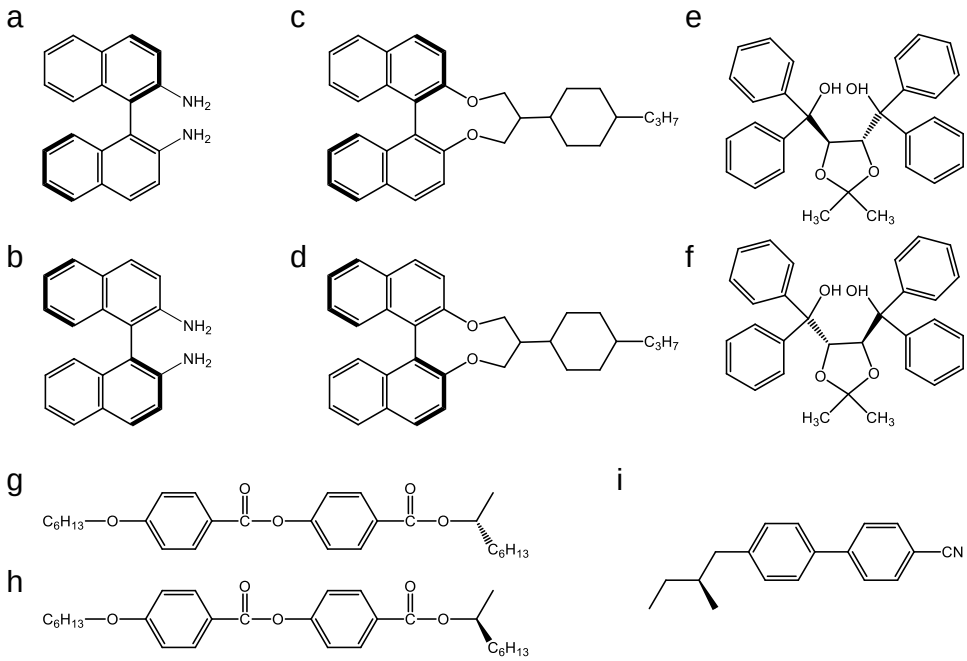

Figure 4.2. Molecular structures of various chiral additives. a–k, (*R*)-BN (**a**), (*S*)-BN (**b**), R5011 (**c**), S5011 (**d**), (*R*, *R*)-TADDOL (**e**), (*S*, *S*)-TADDOL (**f**), R811 (**g**), S811 (**h**), and CB15 (**i**).

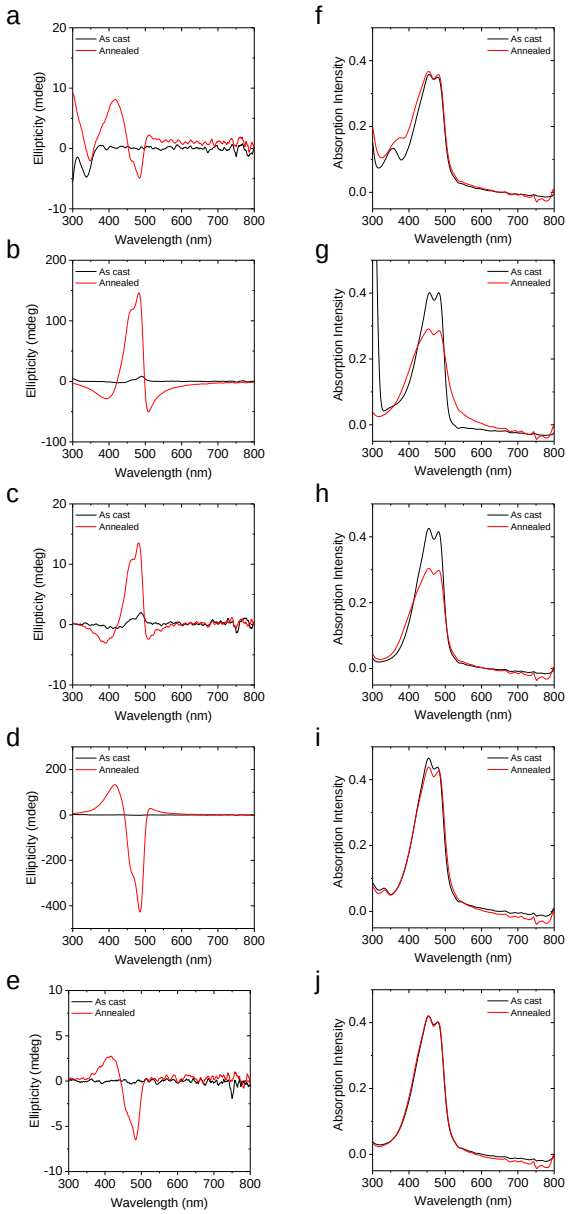

Figure 4.3. Circular dichroism and ultraviolet-visible absorption spectra of F8T2 with various chiral dopants. a–e, CD spectra of (*S*)-BN (**a**), CB15 (**b**), R811 (**c**), S5011 (**d**), and (*S*, *S*)-TADDOL (**e**) doped F8T2 thin films before and after thermal annealing. **f–j**, UV-vis absorption spectra of (*S*)-BN (**f**), CB15 (**g**), R811 (**h**), S5011 (**i**), and (*S*, *S*)-TADDOL (**j**) doped F8T2 thin films before and after thermal annealing.

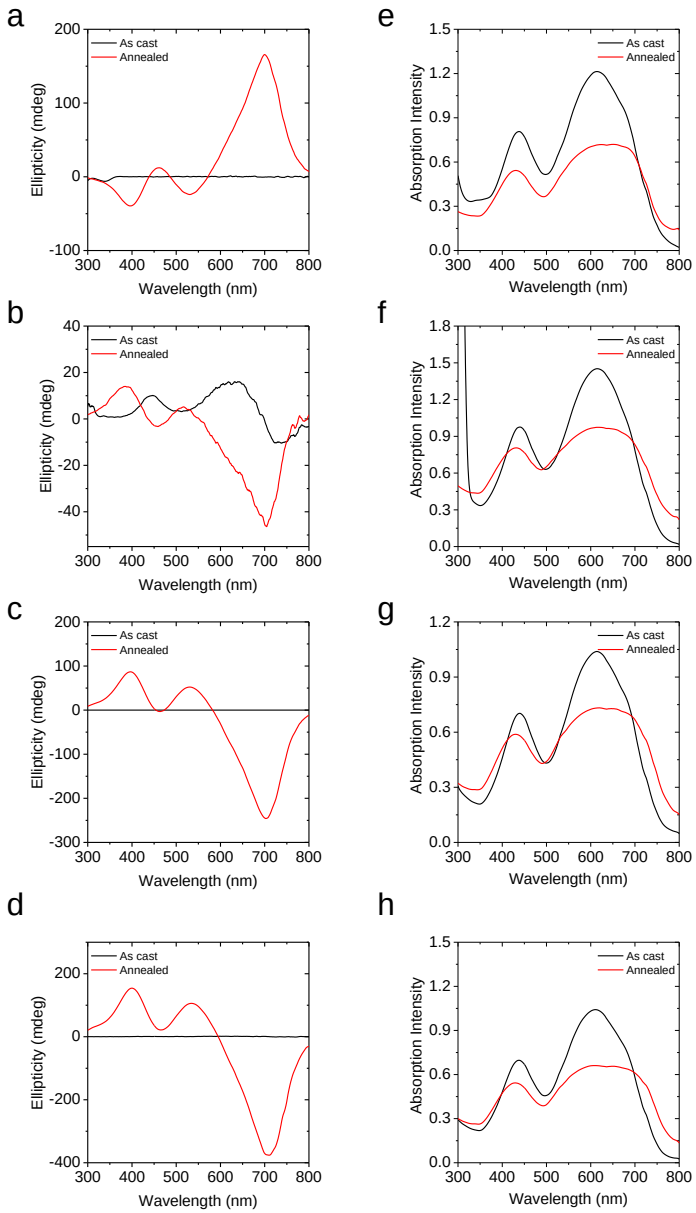

Figure 4.4. Circular dichroism and ultraviolet-visible absorption spectra of PCPDTTBTT with various chiral dopants. a–d, CD spectra of (*S*)-BN (**a**), CB15 (**b**), R811 (**c**), and (*S*, *S*)-TADDOL (**d**) doped PCPDTTBTT thin films before and after thermal annealing. **e–h,** UV-vis absorption spectra of (*S*)-BN (**e**), CB15 (**f**), R811 (**g**), and (*S*, *S*)-TADDOL (**h**) doped PCPDTTBTT thin films before and after thermal annealing.

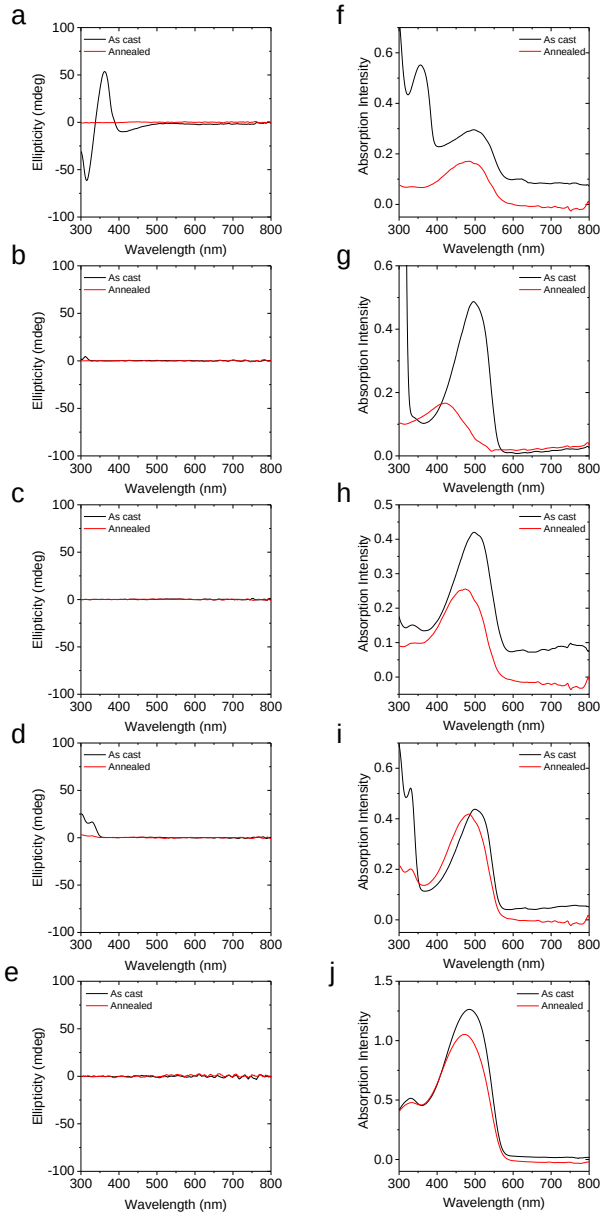

Figure 4.5. Circular dichroism and ultraviolet-visible absorption spectra of MEH-PPV with various chiral dopants. a–e, CD spectra of (*S*)-BN (**a**), CB15 (**b**), R811 (**c**), S5011 (**d**), and (*R*, *R*)-TADDOL (**e**) doped MEH-PPV thin films before and after thermal annealing. **f–j,** UV-vis absorption spectra of (*S*)-BN (**f**), CB15 (**g**), R811 (**h**), S5011 (**i**), and (*R*, *R*)-TADDOL (**j**) doped MEH-PPV thin films before and after thermal annealing.

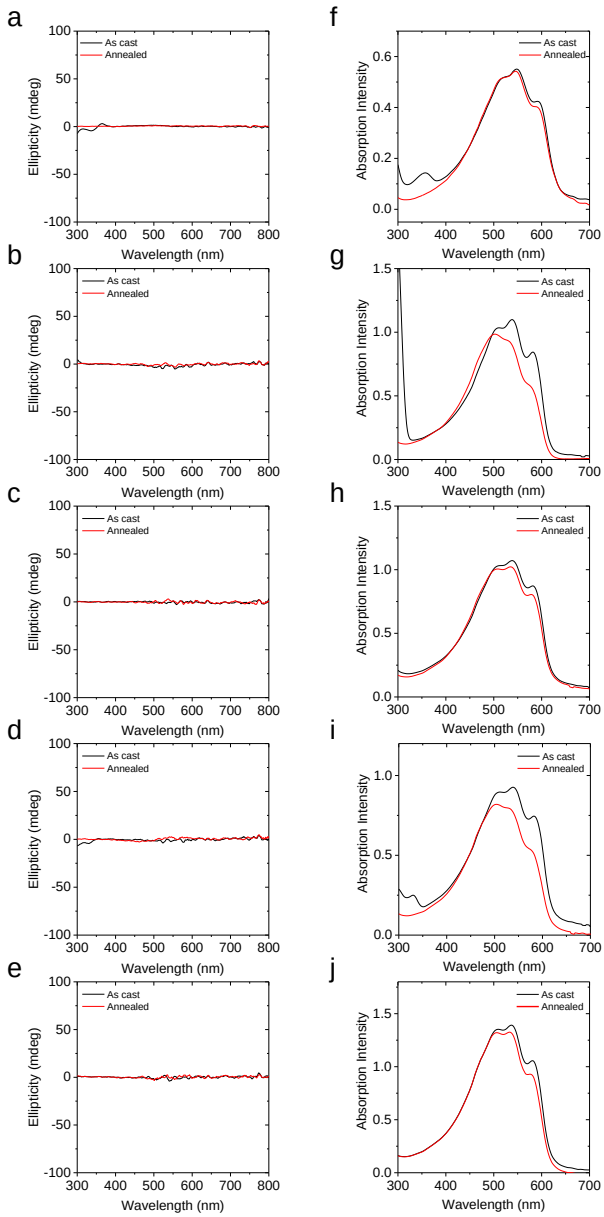

Figure 4.6. Circular dichroism and ultraviolet-visible absorption spectra of P3HT with various chiral dopants. a–e, CD spectra of (*S*)-BN (**a**), CB15 (**b**), R811 (**c**), R5011 (**d**), and (*R*, *R*)-TADDOL (**e**) doped P3HT thin films before and after thermal annealing. **f–j,** UV-vis absorption spectra of (*S*)-BN (**f**), CB15 (**g**), R811 (**h**), R5011 (**i**), and (*R*, *R*)-TADDOL (**j**) doped P3HT thin films before and after thermal annealing.

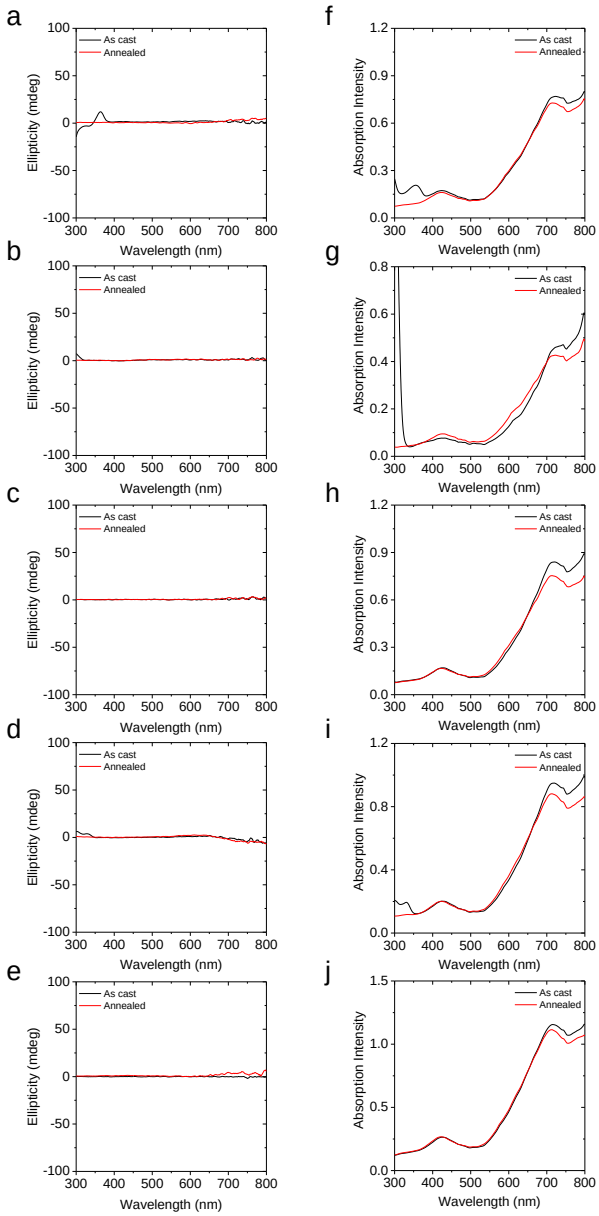

Figure 4.7. Circular dichroism and ultraviolet-visible absorption spectra of P29DPP-TTSe with various chiral dopants. a–e, CD spectra of (*S*)-BN (**a**), CB15 (**b**), R811 (**c**), S5011 (**d**), and (*S*, *S*)-TADDOL (**e**)**,** doped PDBT-co-TT thin films before and after thermal annealing. **f–j**, UV-vis absorption spectra of (*S*)-BN (**f**), CB15 (**g**), R811 (**h**), S5011 (**i**), and (*S*, *S*)-TADDOL (**j**) doped PDBT-co-TT thin films before and after thermal annealing.

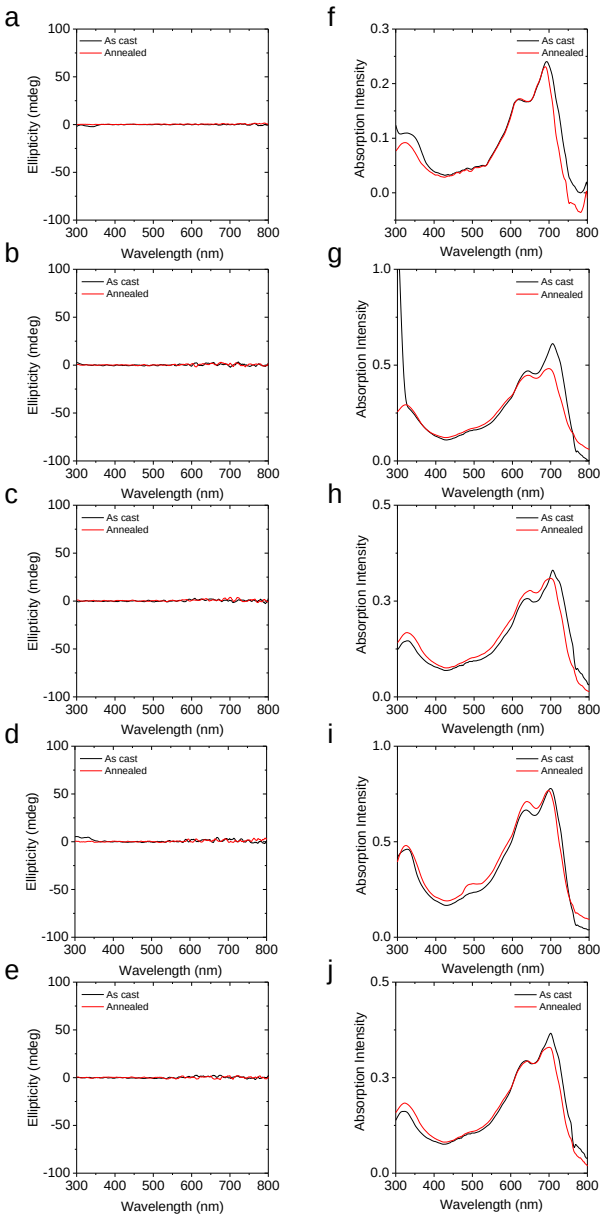

Figure 4.8. Circular dichroism and ultraviolet-visible absorption spectra of PTB7-Th with various chiral dopants. a–e, CD spectra of (*S*)-BN (**a**), CB15 (**b**), S811 (**c**), S5011 (**d**), and (*S*, *S*)-TADDOL (**e**) doped PTB7-Th thin films before and after thermal annealing. **f–j,** UV-vis absorption spectra of (*S*)-BN (**f**), CB15 (**g**), S811 (**h**), S5011 (**i**), and (*S*, *S*)-TADDOL (**j**) doped PTB7-Th thin films before and after thermal annealing.

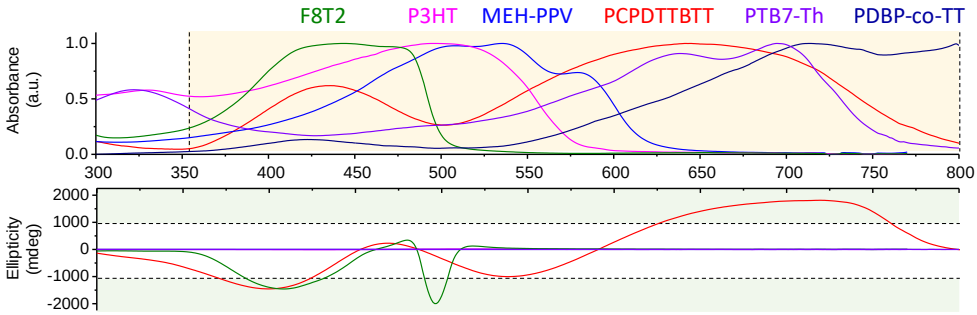

Figure 4.9. Ultraviolet-visible absorption and circular dichroism spectra of assorted conjugated polymer/chiral additive blends. Various conjugated polymers and chiral additives were used to fabricate the homochiral active layer. Among them, only fluorene-based and CPDT-based polymers exhibited strong CD signals. In addition, PCPDTTBTT, well-known in photon-absorbing devices, displayed broader UV-vis absorption and CD spectra compared with F8T2.

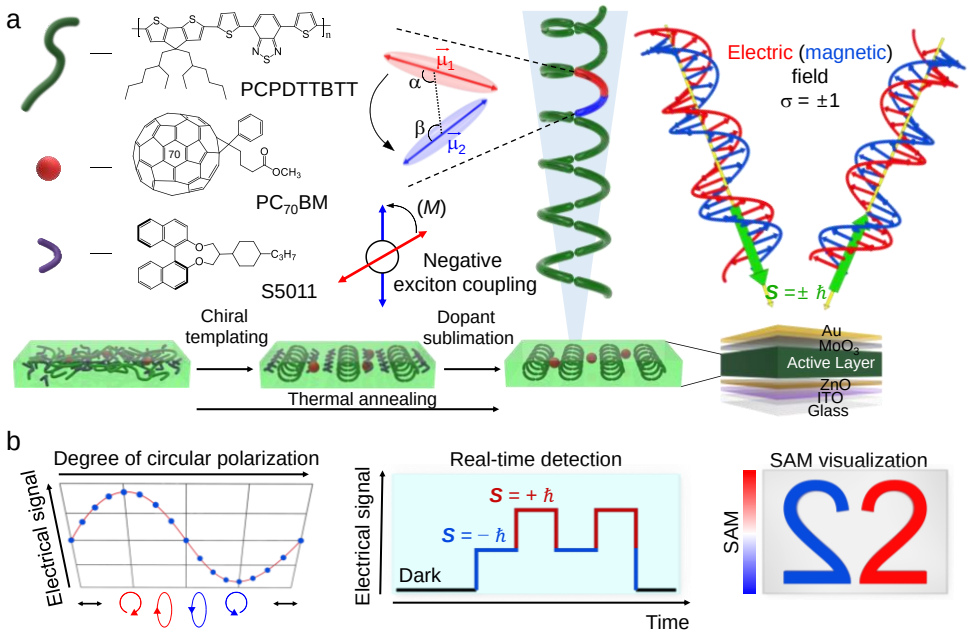

Figure 4.10. Fabrication of a highly dissymmetric homochiral active layer and its application in photon spin sensor. a, Schematic of photon spin sensor device. Chiral transient templating using volatile enantiomer calcination and chain rearrangement during thermal treatment generates 1-dimensional, supramolecular ordering of conjugated chromophores. The long range, interchromophore chiral activity ensures negative exciton coupling in S5011 doped supramolecular helix. The highly dissymmetric active layer achieved a high discrimination property by interacting with circular polarization through chiroptical activity. **b**, Schematic illustrations of delicate extraction of polarization helicity information in unknown elliptically polarized beams and SAM visualization in real-time spatiotemporal imaging in an on-chip device.

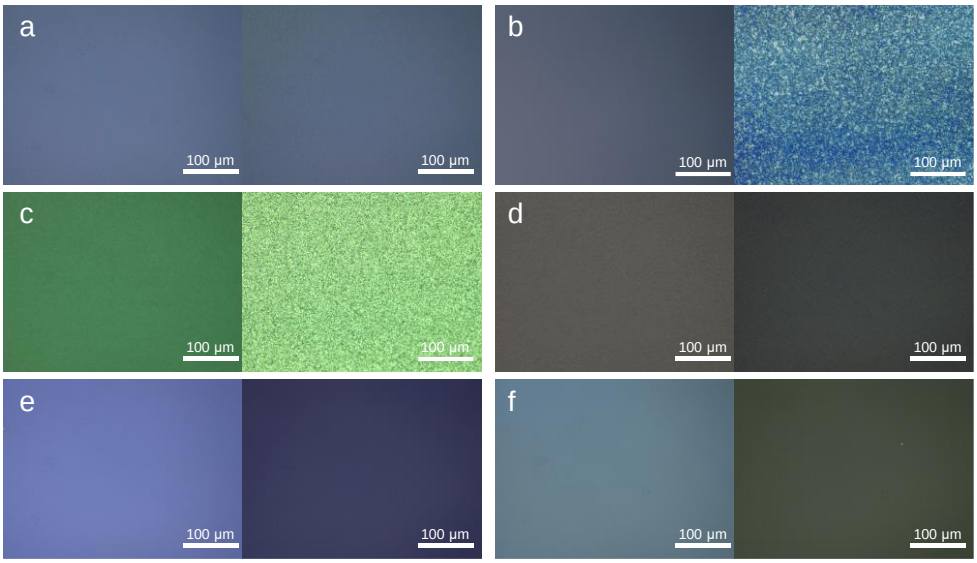

Figure 4.11. Polarized optical microscopy images of conjugated polymeric films. **a–f**, POM images of P29DPP-TTSe (**a**), PCPDTTBTT (**b**), F8T2 (**c**), P3HT (**d**), MEH-PPV (**e**), and PTB7-Th (**f**) thin films before (left) and after (right) thermal treatment with the angle between two polarizers of 0°.

4.2.2. Circular Dichroism Study

The PCPDTTBTT films exhibited dopant-independent broadband absorption spectra with two absorption maxima (at 645 and 435 nm) associated with π–π* and charge-transfer transitions (**Figure 4.12a**).[29-30] The addition of chiral dopant R5011 or S5011 and subsequent thermal annealing resulted in extremely strong chiroptical properties (**Figure 4.12b**, and **13**). The doped films exhibited mirror-image CD signals according to the chirality of the dopant with large CD intensity (> 20°) and dissymmetry factor (~0.8) in thin films (160 nm). The supramolecular chirality of the main absorption band of the polymers originated from efficient chirality inspirations within highly crystalline mesoscopic alignments. **Figure 4.12c**, **d** shows that the removal of dopants after thermal annealing was clearly discernible in the UV-vis spectra, which demonstrated that the chiral dopants acted as a template for helical stacks of polymer chains during chain rearrangements, rather than forming complexes with the polymer chains or crystal itself.

The CD-silent feature was observed in unannealed doped films and doped films annealed at higher than clearing temperature (290°C) (**Figure 4.12e**, **f**). Notably, the CD signals were saturated as the dopant content reached 50 wt% (**Figure 4.14a**). Additional introduction of chiral additives could not affect further changes in chiroptical effects, which indicated that the superposed chiral dopants did not cause a sudden reduction of chiroptical effects. **Figure 4.14b** shows the thickness-dependent chiroptical effects, which were quantitatively estimated as dissymmetry factors by normalizing the CD to the unpolarized absorbance of the sample. The extraordinarily high *g* values were independent of film thickness (> 100 nm), as it is commonly observed in conventional monodomain cholesteric stacks.[22, 31] Notably, the thin films showed small *g* values (~0.1) in very thin films (< 60 nm), but these values remained high with respect to other conjugated polymers except the fluorene series. This behavior may be related to the strong surface effect on oxide substrates,

leading to the formation of different morphologies during solidification and chain rearrangement processes.

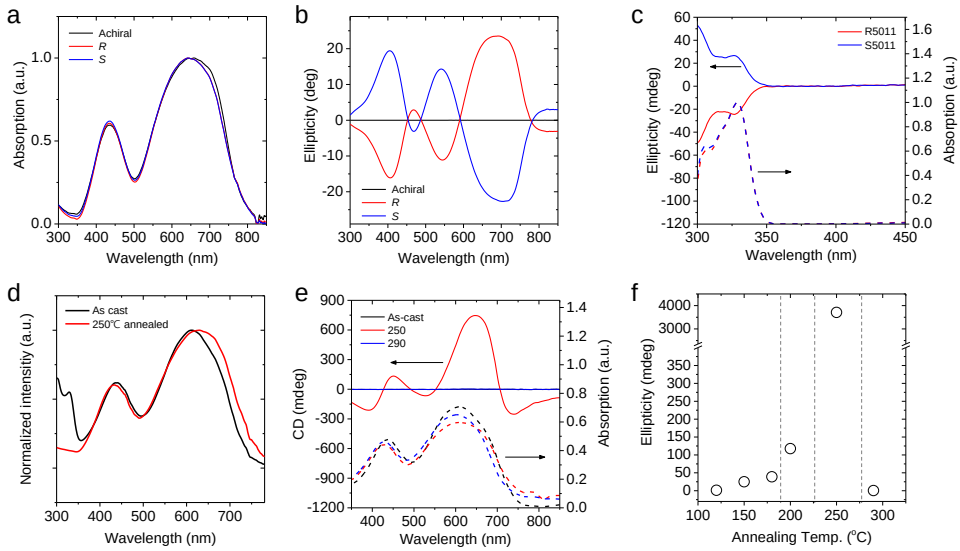

Figure 4.12. Circular dichroism and ultraviolet-visible absorption spectra. a, UV-vis absorption spectra of CPDT-based neat and doped polymer films after thermal annealing. **b**, Circular dichroism spectra of the CPDT-based neat and R5011- or S5011-doped polymer films. **c**, CD and UV-vis absorption spectra of chiral additives R5011 and S5011. **d**, UV-vis absorption spectra of CPDT-based doped polymer thin films before and after thermal annealing. **e–f**, CD and UV-vis absorption spectra (**e**) and CD intensity maxima (**f**) of CPDT-based doped thin films according to annealing temperature.

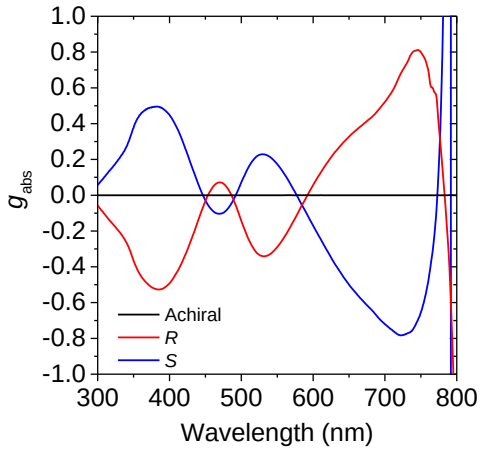

Figure 4.13. g_{abs} spectra of CPDT-based neat and doped polymer films after thermal annealing. Optimized films were formed using 30 mg mL^{-1} PCPDTTBTT in toluene. Doped films included 50 wt% of R5011 or S5011 in total solute.

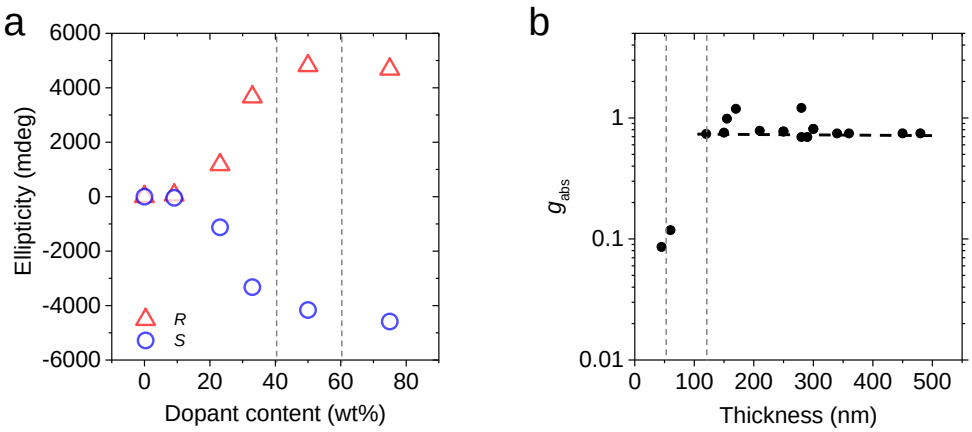

Figure 4.14. Chiroptical properties of CPDT-based polymer films. a, Circular dichroism intensity maxima of CPDT-based doped thin film as a function of chiral additive content. **b**, g_{abs} maxima of CPDT-based doped thin films as a function of film thickness.

4.2.3. Thermal Property Study

Thermogravimetric analysis and DSC were used to characterize the phase behavior and crystallization properties of the conjugated polymers as a function of temperature (**Figure 4.15**). PCPDTTBTT lost 5 wt% as the temperature increased to 430°C and decomposed by initial loss of alkyl substituents, which suggested high thermal stability. The peaks and valleys in DSC curves correspond to the release or intake of thermal energy that occurs during phase transitions. The DSC thermogram of the polymer PCPDTTBTT revealed the T_g at ~140°C and the onset of cold crystallization at 189°C. Two peaks observed between 220°C and 255°C indicated that the polymer contained two distinct mesophase states. The first peak at ~235°C corresponded to the melting of the solid to mesophase and the second peak corresponded to the transition between mesophases. Finally, the onset of the mesophase–isotropic transition appeared at 257°C, when the polymer became a disordered, liquid phase. Therefore, the optimized annealing temperature of 250°C used in this study allowed the polymer to attain a long-range ordered supramolecular structure, thereby enabling intense chiroptical properties with the addition of chiral dopants.

Polarized optical microscopy (POM) studies with crossed linear polarizers revealed that the thin films annealed at a temperature above the clearing temperature did not have any locally anisotropic and birefringent domains (**Figure 4.16**). Similarly, the as-cast films showed no birefringence because they lacked long-range ordering of the polymer chains. In contrast, clear Schlieren textures were observed after thermal treatment for the mesophase transition. The annealed chiral doped films displayed Schlieren textures almost identical to the textures of neat films, regardless of the ratio of chiral dopants (**Figure 4.17**). This indicated the absence of highly ordered cholesteric stacking, such as the stacking observed in double-spiraled textures (with a certain helical pitch) of chiral nematic films formed on rubbed substrates or sandwiched liquid-crystal cells.[32]

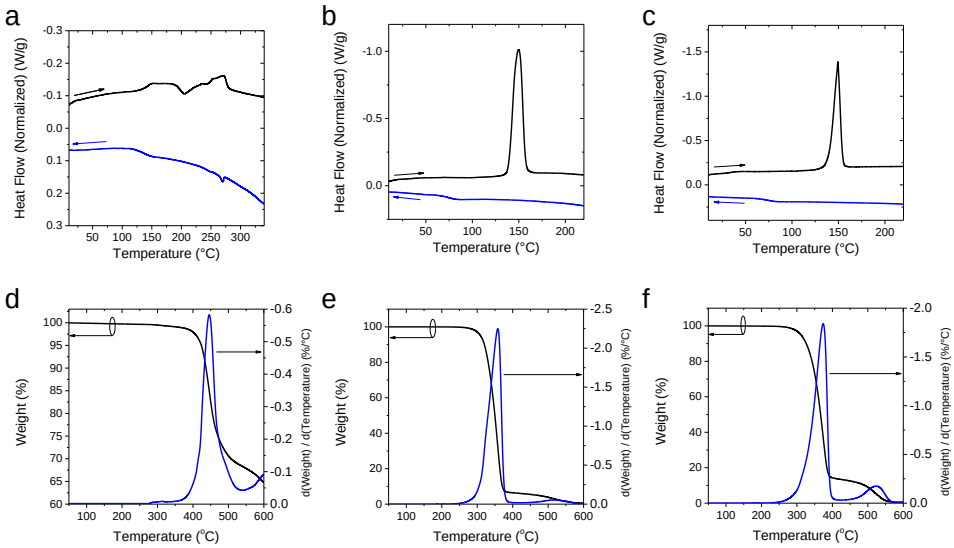

Figure 4.15. Differential scanning calorimetry and thermogravimetric analysis results of PCPDTTBTT and chiral dopants. a–c, DSC curves of PCPDTTBTT (**a**), R5011 (**b**), and S5011 (**c**) in heating (black) and cooling (blue) modes recorded at 10°C/min. **d–f**, TGA curves of PCPDTTBTT (**d**), R5011 (**e**), and S5011 (**f**).

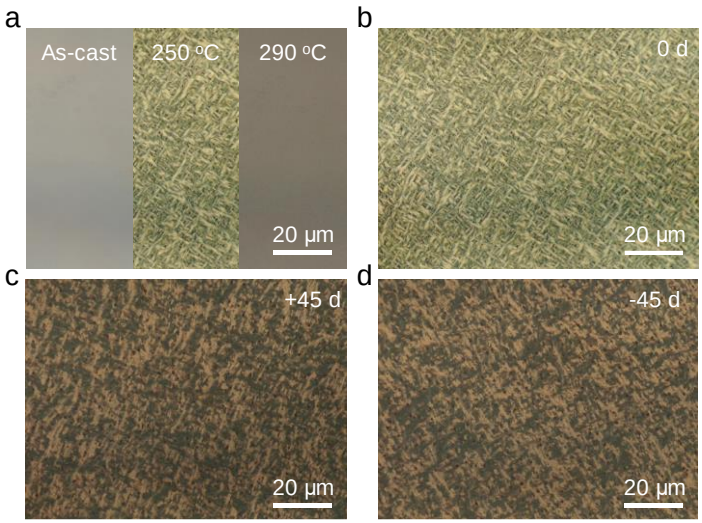

Figure 4.16. Polarized optical microscopy images of PCPDTTBTT films. a, Temperature-dependent POM images of PCPDTTBTT thin films. **b**–**d**, Images after thermal annealing with the angle between two polarizers of 0° (**b**), 45° (**c**), and −45° (**d**).

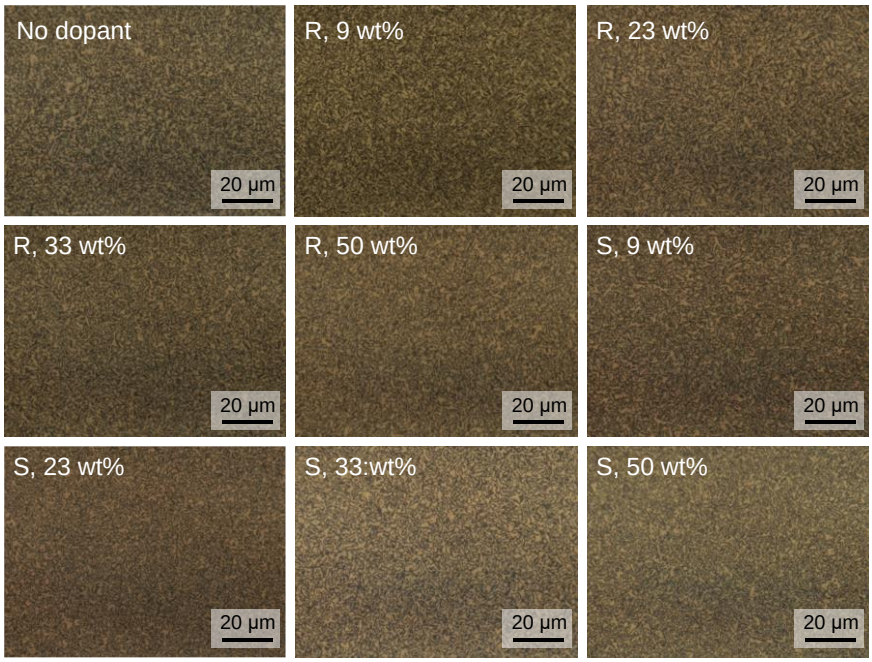

Figure 4.17. Polarized optical microscopy (POM) images of doped polymer films after thermal treatment with various dopant concentrations.

4.2.4. Microscale Morphology Analysis

SEM and AFM were used to observe the surface morphological structure of the chiral active layer at the microscale (**Figure 4.18**, and **19**). Before thermal annealing, undoped films and films with high chiral doping content showed morphologies similar to small nanobeads. After thermal annealing, the aggregates rearranged into a fibril-like organization with a rough surface (root-mean-square height: 1.9 nm) in undoped films. The long, one-dimensional structures at the submicron scale were responsible for the substantial optical anisotropic properties observed in POM images. In contrast, the presence of chiral small molecules during thermal annealing resulted in the rearrangement of constituent bead-shaped aggregates into smooth and homogeneous, wavy arrays of string-like features, which differed from the amorphous and rugged aggregates of the neat films (root-mean-square = 0.7 nm). The surface was comprised of nanofibrils with mean width of *ca.* 10–20 nm and length < 1 μm. Thus, the introduction of chiral small molecules resulted in the rearrangement of "worms" of constituent beads into wavy fiber arrays with smooth surfaces. The nanofibrils were arranged parallel to the surface, which may have been influenced by the nature of the free space.[17] Transmission electron microscopy measurements revealed flattened and oriented surfaces in a wavy rod-like fibril array organization with a heterogeneous chain rearrangement (**Figure 4.20**).

Intermediate morphological features were observed in species annealed below the mesophase transition temperature (**Figure 4.21**). SEM images of doped films annealed at 180°C exhibited much shorter fibrillar structures with remaining nanobeads, which indicated that the nanofibrils had formed by the aggregation of existing nanobeads. The magnified view of doped films annealed at 250°C in high-resolution AFM images indicated that the nanofibrils were composed of a string of beads *ca.* 4–5 nm in diameter (**Figure 4.22**). In addition, several nanofibrils with width of *ca.* 5–10 nm aggregated into bundle-like nanofibers.

Cross-sectional SEM images were observed to investigate the effects of interfacial interactions among the substrate, films, and free space on the morphology of active layers across the film depth (**Figure 4.23**, and **24**). Molecular rearrangements (ranging from bead-like morphologies to rod-like features) were observed throughout neat polymer films after thermal annealing, resulting in very rough surfaces and cross-sections. In contrast, chiral small additives resulted in much smoother surfaces and cross-sections in the annealed state. Notably, the nanofibrils preferred vertical ordering on the substrate, but tended to arrange in parallel at the interface with air, where the arrangements were more distinct in doped films. Characteristic "rice straw" features without complex cholesteric nature or periodic helical pitch were observed. Similar erratic features were observed in large-scale side-view cross-sectional SEM images in the presence of both enantiomeric dopants (**Figure 4.25**).

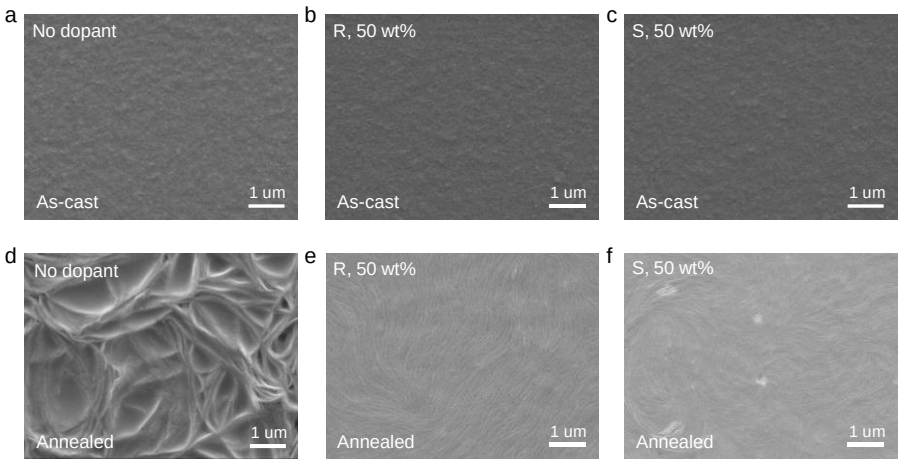

Figure 4.18. Scanning electron microscopy images of polymer films. a–c, Neat PCPDTTBTT (**a**), R5011-doped (**b**), and S5011-doped (**c**) films before thermal annealing. **d–f**, Neat PCPDTTBTT (**d**), R5011-doped (**e**), and S5011-doped (**f**) films after thermal annealing.

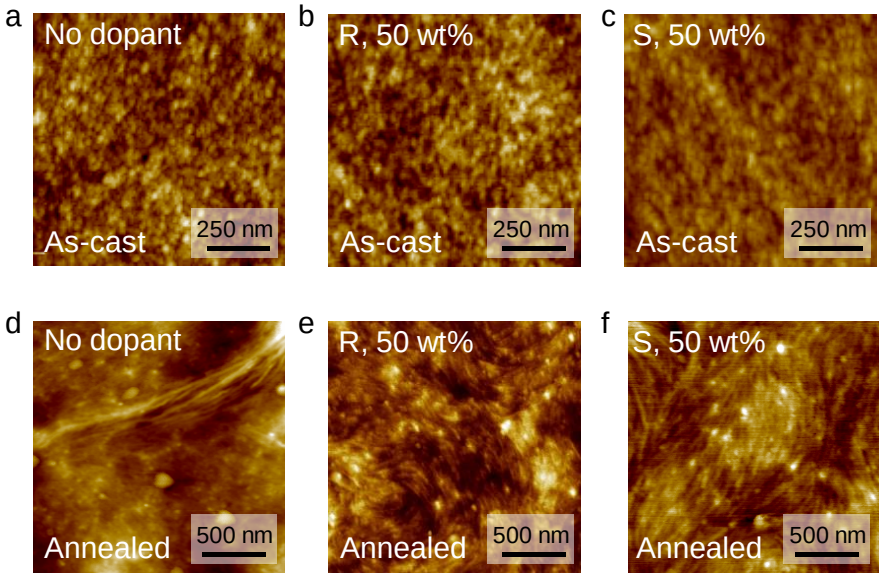

Figure 4.19. Atomic force microscopy images of polymeric films. a–c, Neat PCPDTTBTT (**a**), R5011-doped (**b**), and S5011-doped (**c**) films before thermal annealing. **d–f**, **N**eat PCPDTTBTT (**d**), R5011-doped (**e**), and S5011-doped (**f**) films after thermal annealing.

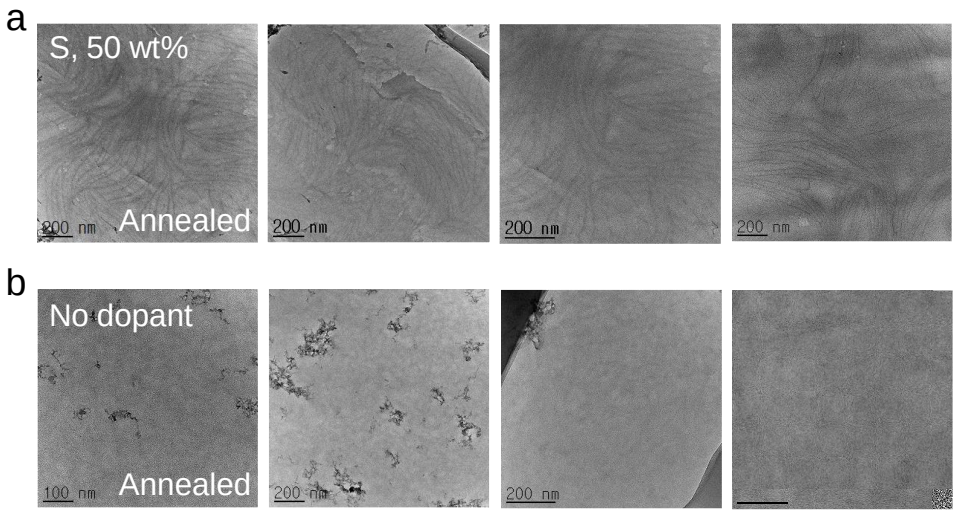

Figure 4.20. Transmission electron microscopy images of annealed polymeric films. a, Chiral doped PCPDTTBTT film. **b**, Neat PCPDTTBTT film.

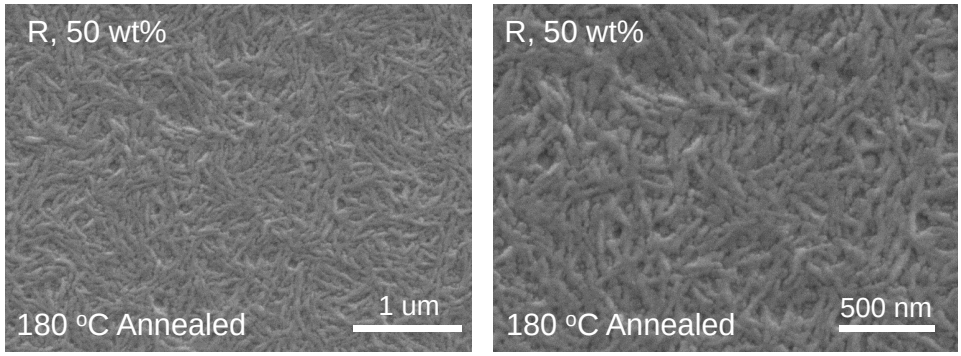

Figure 4.21. Scanning electron microscopy images of chiral doped films annealed at 180°C.

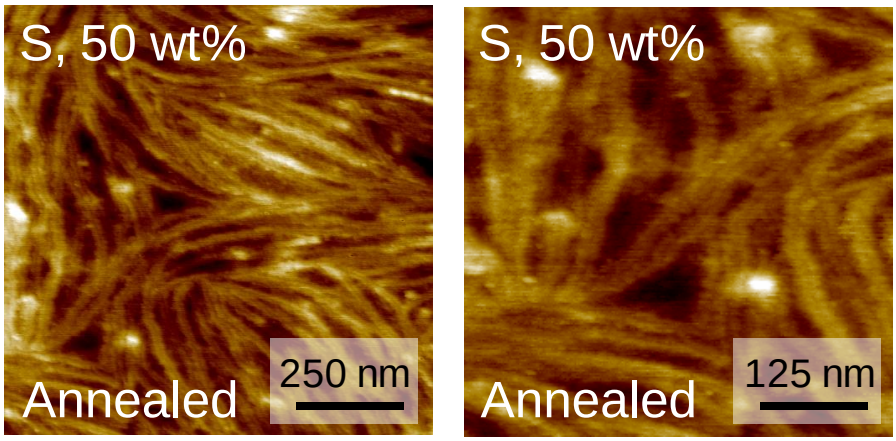

Figure 4.22. High-resolution atomic force microscopy images of chiral (S5011) doped PCPDTTBTT films after thermal annealing.

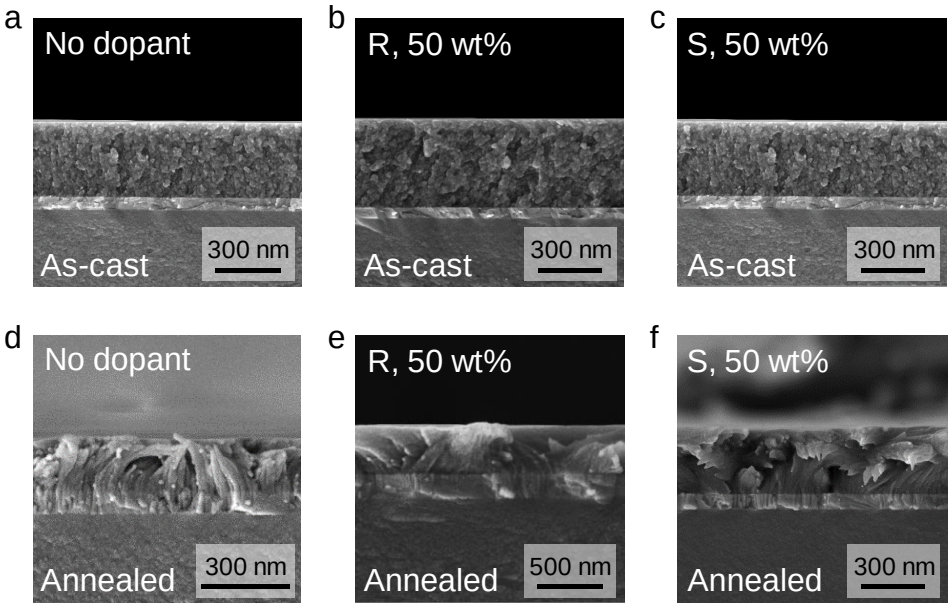

Figure 4.23. Cross-sectional scanning electron microscopy images of polymeric films. a–c, Neat PCPDTTBTT (**a**), R5011-doped (**b**), and S5011-doped (**c**) films before thermal annealing. **d–f**, **N**eat PCPDTTBTT (**d**), R5011-doped (**e**), and S5011-doped (**f**) films after thermal annealing

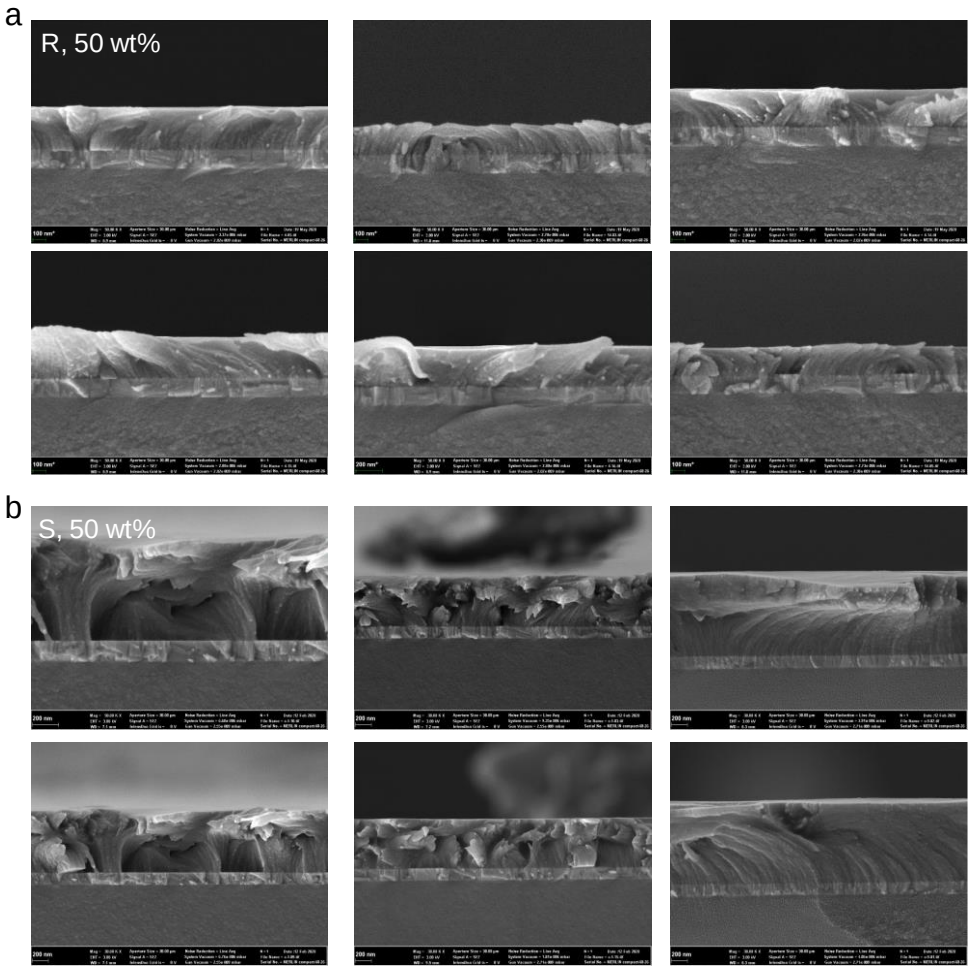

Figure 4.24. Cross-sectional scanning electron microscopy images of polymeric films after thermal annealing. a, R5011-doped PCPDTTBTT thin films. **b**, S5011-doped PCPDTTBTT thin films.

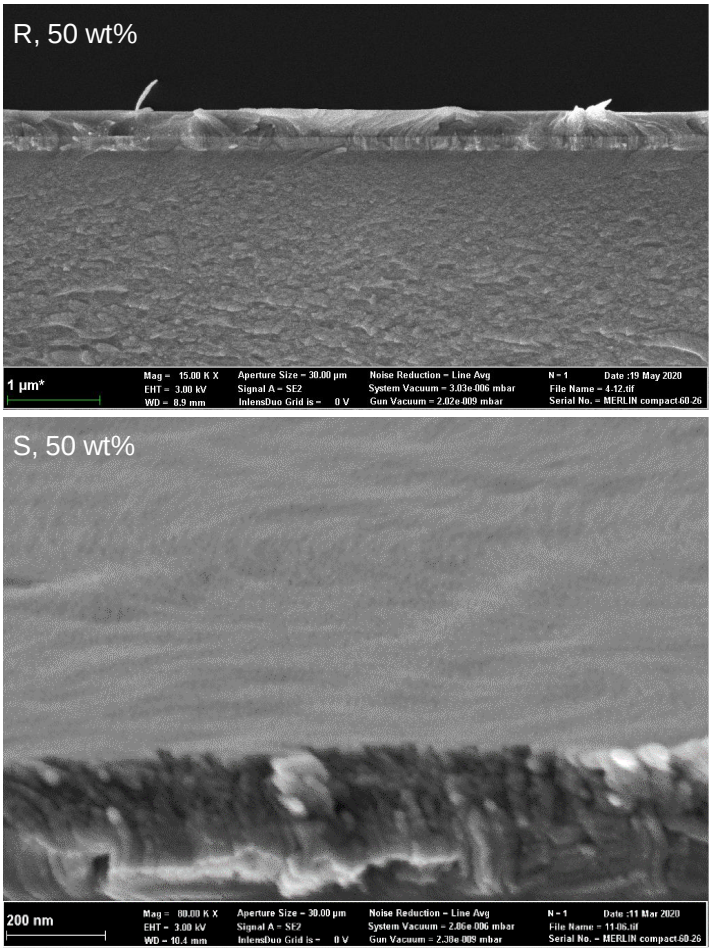

Figure 4.25. Large-scale and side-view cross-sectional scanning electron microscopy images of doped polymeric films after thermal annealing.

4.2.5. X-Ray Diffraction Study (interpreted by Hyungju Ahn in Pohang Accelerator Laboratory)

Sub-microscale molecular packing was investigated using X-ray diffraction techniques. Powder X-ray diffraction measurements revealed structural changes in neat and doped polymer films before and after thermal treatments (**Figure 4.26**). The annealed films showed a sharp peak at 2θ = 7.30° for out-of-direction molecular stacking (d = 12 Å), which corresponded to interdigitated packing of linear alkyl side chains or chain backbone repeat distance, rather than π−π stacking of conjugated planes. The diffraction peaks caused by chain rearrangement during thermal annealing were clearer and more distinct in neat films than in doped films, which indicated reduced crystallinity or a decrease in existing molecular ordering through the construction of another crystalline order after introduction of chiral small molecules. The 3D packing structures and geometries of polymer chains were further elucidated by 2D grazing-incidence wide-angle X-ray diffraction (GIWAXD) studies. Before thermal annealing, both neat and doped polymer films exhibited a polycrystalline nature with several well-defined ring patterns without any chain ordering preference in both in-plane and out-of-plane directions (**Figure 4.27**). **Figure 4.28a** shows that the 2D GIWAXD patterns of the annealed neat films had highly oriented X-ray reflections with the strongest (001) diffraction peak at $q_{xy} \approx$ 0.52 $Å^{-1}$ in the out-of-plane direction (d = 12 Å, similar to the diffraction pattern observed in powder X-ray diffraction), which corresponded to the typical interchain distance of conjugated D−A polymers, such as diketopyrrolopyrrole (DPP)-, isoindigo (ISO)-, and rylene diimide-based polymers. The polymer chains crystallized in the triclinic *P1* space group with unit cell lattice constant lengths a, b, and c of 12.0, 9.5, and 12.7 Å and lattice constant angles α, β, and γ of 97°, 95°, and 90°, respectively. When advancing the interpretation that chiroptical activities, film morphologies, and molecular packing are related to a surface effect, questions arise regarding molecular arrangements and crystallinities according to film thickness

direction. **Figure 4.29** shows 2D GIWAXD patterns as a function of incident angle α_i. The neat polymer films exhibited even distribution of crystallinity according to film depth, which indicated a weak surface effect of molecular packing during the chain rearrangement.

Chiral small molecule doping caused the emergence of distinctive crystalline changes; a new diffraction pattern was observed in relation to typical columnar structures with a fade-out of the triclinic polymeric crystals (**Figure 4.28b**, and **4.30**). Because the dopant-only films displayed an amorphous ring-pattern halo in the thin-film state (**Figure 4.31**), it was speculated that the new diffraction pattern resulted from chain rearrangement of the CPDT-based polymer in the presence of the chiral small molecules. The patterns were not differential according to chiral composition. However, the patterns were distinct from the "usual" packing, namely, conventional lamella stacking of conjugated polymers; they exhibited unique supramolecular long-range ordering. Analysis of the GIWAXD results revealed that the small-angle region reflection corresponded to a tetragonal 2D columnar phase with helical π-stacked assemblies (**Figure 4.28c**, and **4.32**). The center-to-center distance between helices (corresponding to the helix outer diameter), calculated from the position of the (100) Bragg reflection, was 45 Å. The intrahelix π-stacking distance estimated from the position of (010) reflection was 3.83 Å. Therefore, the polymer chains with chiral small molecule additives and thermal treatment presumably did not form the regular layer-like structures exhibited by common conjugated polymers; instead, they presumably formed supramolecular helical columnar structures with the columnar axis in-plane and the direction of π–π interactions parallel to the columnar axis. Such intrahelical chromophore orientations in extremely long nanofibrils enabled chiral exciton coupling of helically stacked chromophores.[33] Delocalization of electrons ensured the partitioning of excitation energy and rotational strength between the in-phase and out-of-phase electric dipole moment transitions, required for polarization-sensitive interaction with CP light.[14, 34-35] The 2D GIWAXD patterns

as a function of incident angle revealed the crystallinities of the in-plane helical ordering according to film depth (**Figure 4.33**). These patterns showed weak diffraction peaks at a beam incident angle of 0.13°, which indicated a strong surface anchoring effect on in-plane helical ordering during the chiral templating process.

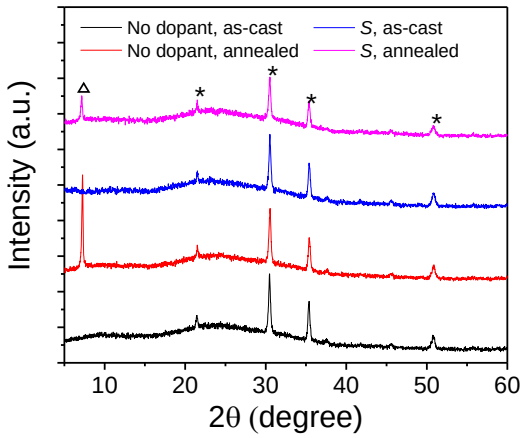

Figure 4.26. Powder X-ray diffraction results of neat polymeric and chiral doped thin films before and after thermal annealing. Triangular markers represent diffraction peaks from polymers and asterisks represent diffraction peaks from zinc oxide on the substrate.

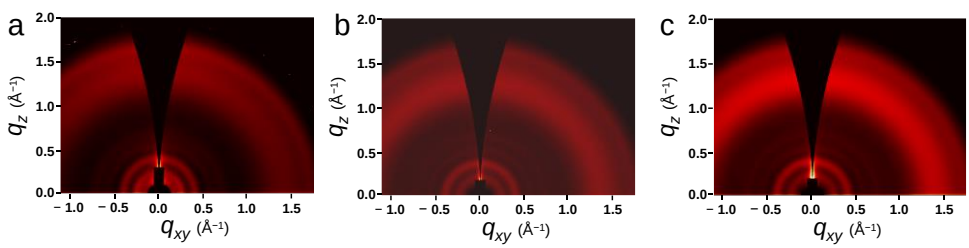

Figure 4.27. Two-dimensional grazing-incidence wide-angle X-ray diffraction results of polymeric films before thermal annealing. a–c, Neat PCPDTTBTT (**a**), R5011-doped (**b**), and S5011-doped (**c**) films before thermal annealing with beam incident angle of 0.12°.

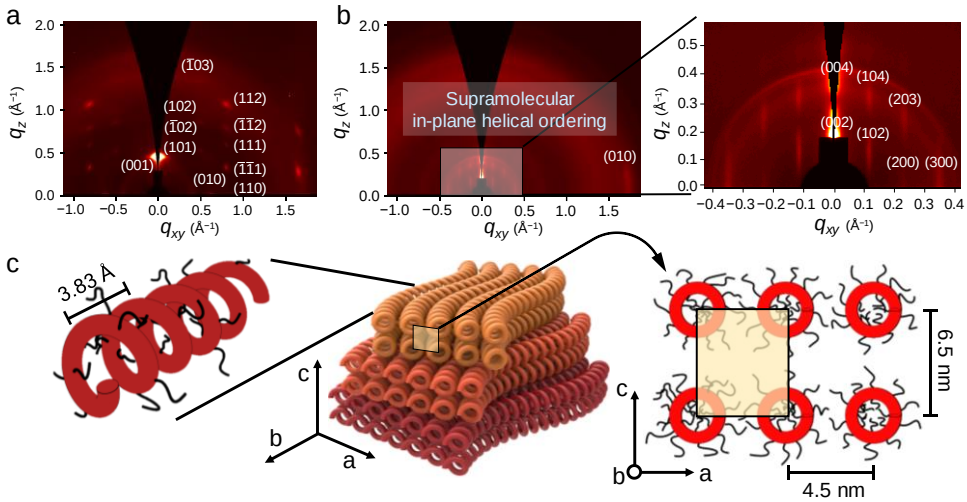

Figure 4.28. Molecular packing information of chiral doped polymeric films. a, **b**, Two-dimensional (2D) grazing-incidence wide-angle X-ray diffraction patterns of annealed CPDT-based neat polymer (**a**) and doped polymer (**b**) films after thermal annealing. **c**, Schematic image of a tetragonal 2D columnar phase with helical π-stacked assemblies.

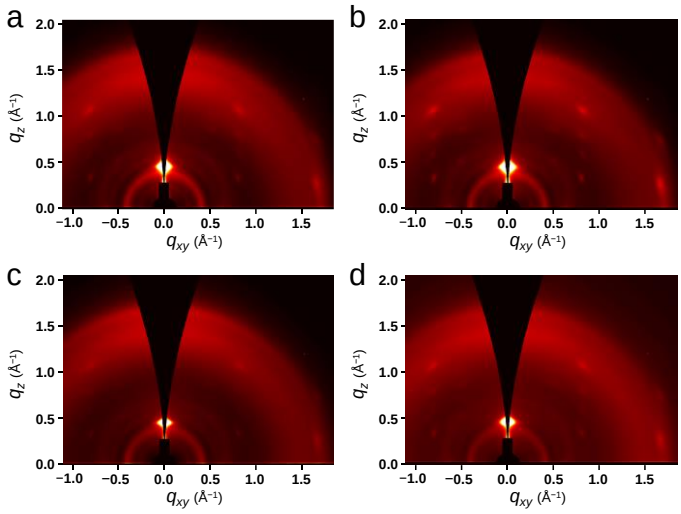

Figure 4.29. Two-dimensional grazing-incidence wide-angle X-ray diffraction results of polymeric films after thermal annealing. a–d, Neat PCPDTTBTT films with beam incident angle of 0.08° (**a**), 0.1° (**b**), 0.12° (**c**), and 0.13° (**d**).

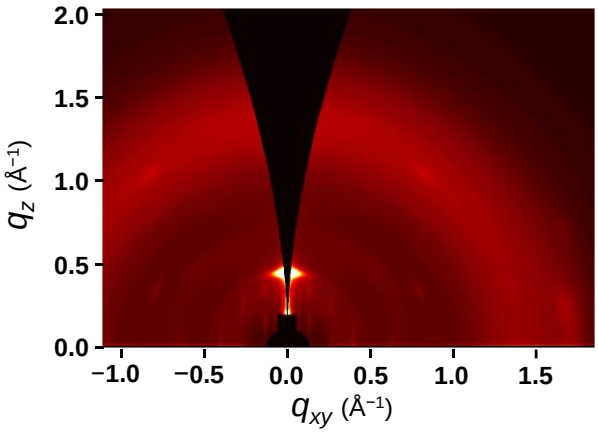

Figure 4.30. Two-dimensional grazing-incidence wide-angle X-ray diffraction results of chiral doped polymeric films after thermal annealing. R5011-doped PCPDTTBTT films with beam incident angle of 0.12°.

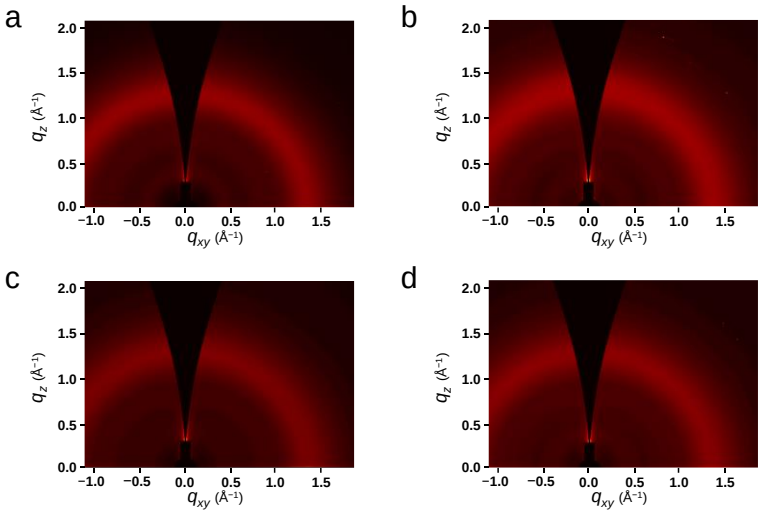

Figure 4.31. Two-dimensional grazing-incidence wide-angle X-ray diffraction results of chiral dopant films. a–d, Beam incident angle of 0.08° (**a**), 0.1° (**b**), 0.12° (**c**), and 0.13° (**d**).

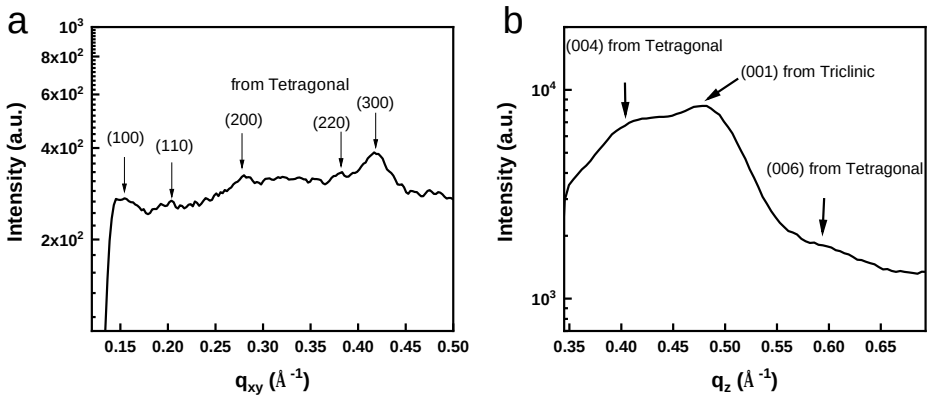

Figure 4.32. One-dimensional grazing-incidence wide-angle X-ray diffraction profiles of chiral dopant films. a, b, Intensity profiles of in-plane patterns of neat polymer films (**a**) and out-of-plane patterns of doped polymer films (**b**) after chain rearrangement. Both chiral dopant films were measured with a beam incident angle of 0.12°.

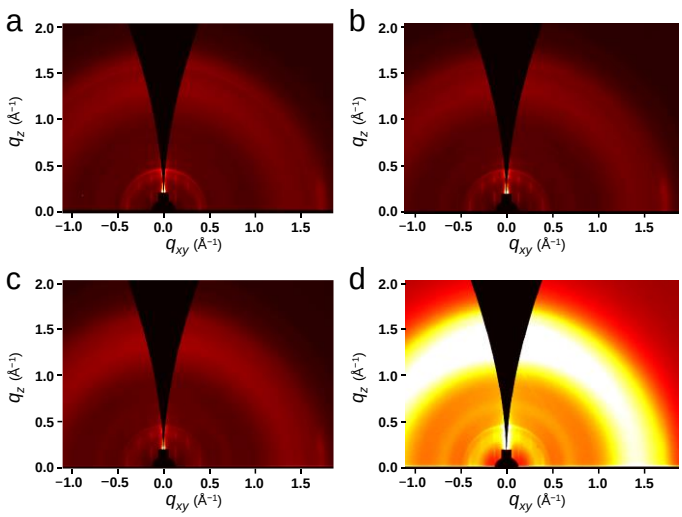

Figure 4.33. Two-dimensional grazing-incidence wide-angle X-ray diffraction results of chiral doped polymeric films after thermal annealing. a−d, S5011-doped PCPDTTBTT films with beam incident angle of 0.08° (**a**), 0.1° (**b**), 0.12° (**c**), and 0.13° (**d**).

4.2.6. XPS, FTIR, and ToF-SIMS Studies

XPS and Fourier-transform infrared spectroscopy (FTIR) were performed on the film surface to systematically investigate the helical rearrangement mechanism and dynamics of CPDT-based polymer films according to chiral templating. Dopant introduction and the annealing process did not significantly alter the S 2p and N 1s spectra because these peaks resulted from the polymer (**Figure 4.34**). The O 1s peak observed for the neat polymer thin film was likely caused by the oxidation of branched alkyl chains during measurement, which was conducted under ambient conditions; thermal annealing reduced the elemental oxygen content. In contrast, when chiral dopant was introduced into the polymer films, the O 1s spectrum exhibited a clear C−O−C peak at 532.5 eV, which originated from the molecular structure of the dopant. However, after thermal annealing, the peak almost disappeared; the peak caused by C−O−H increased in intensity (**Figure 4.35a**). This result implied that the chiral dopant caused chiral templating for supramolecular helical ordering. Most molecules were removed by sublimation at high temperature, as indicated by the sharply reduced overall atomic concentrations of carbon and oxygen after thermal annealing (**Table 4.1**). Similarly, the C−O peak of the C 1s spectrum of the doped polymer film was noticeably less intense after thermal annealing, which implied removal of the chiral dopant.

The chiral templating effect was also confirmed in the FTIR spectra of the blended thin film, where distinct peaks derived from the chiral dopant disappeared after thermal annealing (**Figure 4.36**). The peaks at ~2,900 cm^{-1} in the polymeric films originated from the 2-ethylhexyl side chains of PCPDTTBTT, while the peaks at ~1,500 cm^{-1} originated from ring stretching vibrations of the thiophene, cyclopentadiene, and benzene groups. The peaks derived from chiral dopant introduction almost disappeared after thermal annealing. However, the peak at 1,080 cm^{-1} corresponding to the C−O stretching vibration remained visible after thermal

annealing; it originated from the few remaining oxygen-containing moieties involved in interactions between the polymer chains and chiral dopants.

Time-of-flight secondary ion mass spectroscopy (ToF-SIMS) under negative polarity was conducted to investigate the chiral templating effect as a function of film depth (**Figure 4.37**). The introduction of chiral dopant strongly enhanced oxygen-containing peaks (O^-, OH^-, and C_2OH^-). In the as-cast mixtures, the oxygen-containing peaks and chain fragments ($C_3H_5S^-$, C_2HS^-, $CHNS^-$, and C_4HS^-) directly attributed to the polymer chain did not change according to depth, which indicated that polymer and chiral dopant were homogeneously distributed throughout the thin film without any phase separation in dopant or polymer blends after solvent removal. In addition, the doped films exhibited increased signals of S-containing chain fragments with an additional peak corresponding to CSO^-. The appearance of this peak may be related to ring structure degradation into R−S, R−SN, and R−SO moieties because of strong noncovalent bonding between the S/N content of CPDT/BT/thiophene in the polymer and the O content of the chiral dopants.[36-37] The typical oxygen peaks almost disappeared after thermal annealing, which was consistent with the surface XPS observation of decreased C−O−C peak intensity. Notably, unlike the O-containing peaks, the S-containing peaks greatly changed according to depth even after dopant sublimation, which indicated that the chiral templating phenomenon was more dominant at the free surface because of the surface anchoring effect and difficult dopant diffusion near the substrate (**Figure 4.35b**). From the aforementioned results, I concluded that the chiral dopants induced long-range intrachain helical ordering in supramolecular nanofabric structures via strong intermolecular interactions, such as S⋯O and N⋯O, during polymer chain rearrangement.

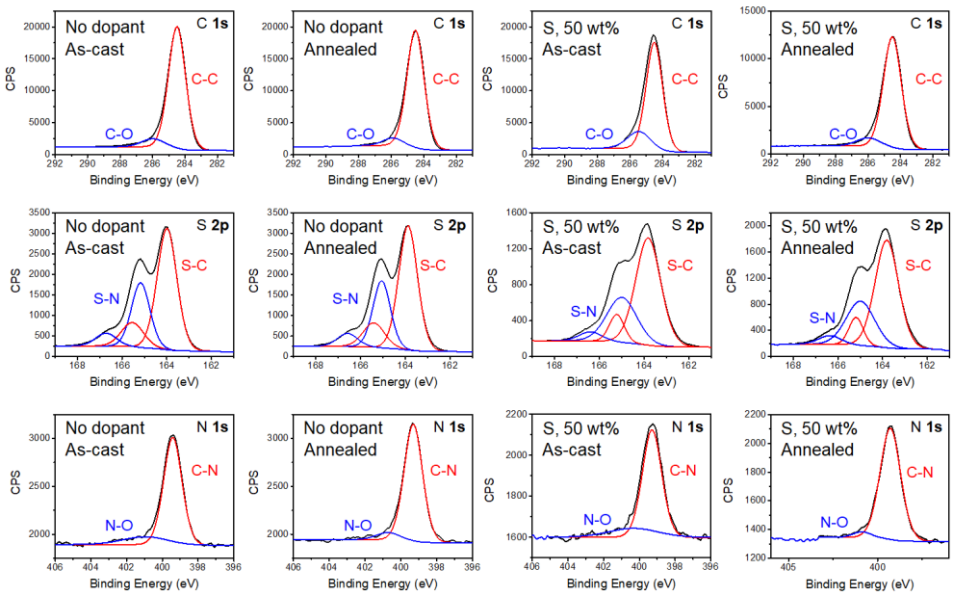

Figure 4.34. XPS results of neat PCPDTTBTT and chiral doped polymeric films before and after thermal annealing.

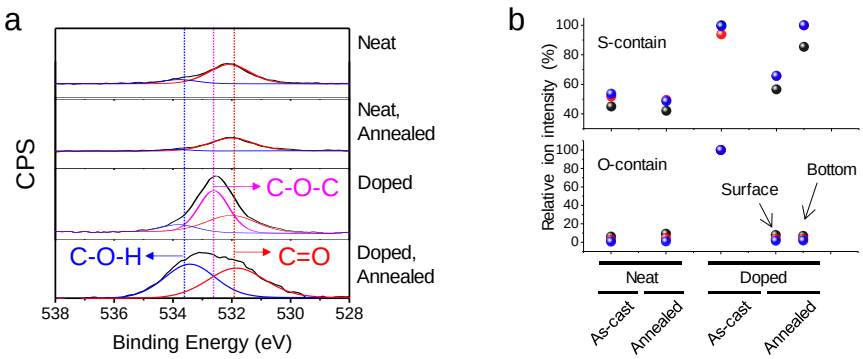

Figure 4.35. XPS and ToF-SIMS characterization of CPDT-based polymer films. **a**, Narrow-scan XPS results for elemental oxygen in CPDT-based polymer films before and after thermal annealing and doping. **b**, ToF-SIMS relative ion intensity graph comparing CPDT-based neat and doped polymer films before and after annealing. S-containing ions are $C_3H_5S^-$ (black), C_2HS^- (red), and C_4HS^- (blue). O-containing ions are O^- (black), OH^- (red), and C_2OH^- (blue).

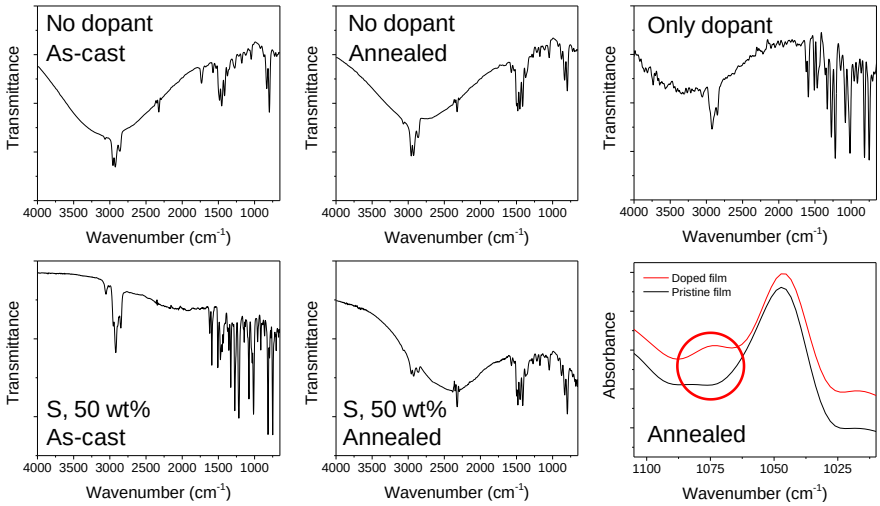

Figure 4.36. Fourier transform-infrared spectroscopy results of neat PCPDTTBTT, chiral dopant, and chiral doped polymeric films according to thermal annealing.

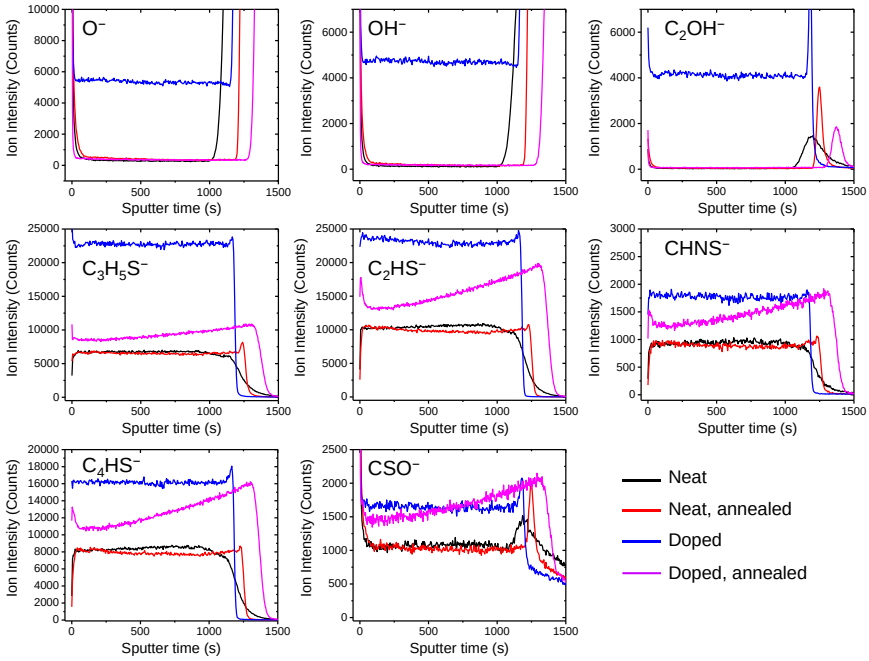

Figure 4.37. ToF-SIMS results of neat PCPDTTBTT and chiral doped polymeric films before and after thermal annealing.

Table 4.1. X-ray photoelectron spectroscopy measurements results of neat and chiral doped polymeric active layers before and after thermal annealing.

	Neat		Doped	
	As cast	**Annealed**	**As cast**	**Annealed**
C	86.3	86.47	89.38	84.95
N	3.36	3.61	1.83	3.61
S	8.66	8.82	4.46	8.77
O	1.67	1.11	4.33	2.67

4.2.7. Characterization of CP Photodetectors

CP photodetectors were fabricated using a chiral-templated *p*-type polymer and a fullerene derivative. Differential absorption of photons and photon-derived carriers led to a large difference in photocurrent according to the SAM of the light. The photocurrent *g* values (g_{Ph}) reached a significant level of 1.2 at −1 V and remained > 1.0 throughout the reverse bias region (**Fig. 4.38a**). To our knowledge, this is the highest reported *g* value for an intrinsic homogeneous organic photodiode. The observed electrical readouts exceeded the state-of-the-art for chiroptical films (**Table 4.2**) demonstrating excellent absorbance−photocurrent correlation (**Fig. 4.38b**). This indicated that they were not affected by the unintentional charge carrier contribution in the photocurrent, which is commonly observed in low-speed sensor operation and voltage sweeps because of hysteresis by trap filling and remnant polarization or bias stress in semiconductors. Stable SAM detection was confirmed by monitoring photocurrent as a function of time under stepwise modulation of the incident beam (**Figure 4.39**); excellent agreement of g_{Ph} with the results of a consecutive voltage sweep was observed. The CP photodetectors showed repeatable SAM detection over 1 h (**Figure 4.40**). The unattenuated dissymmetric values and stable SAM sensitivity in the dynamic studies are expected to be useful for real-time spin visualization in high-frequency circuits.

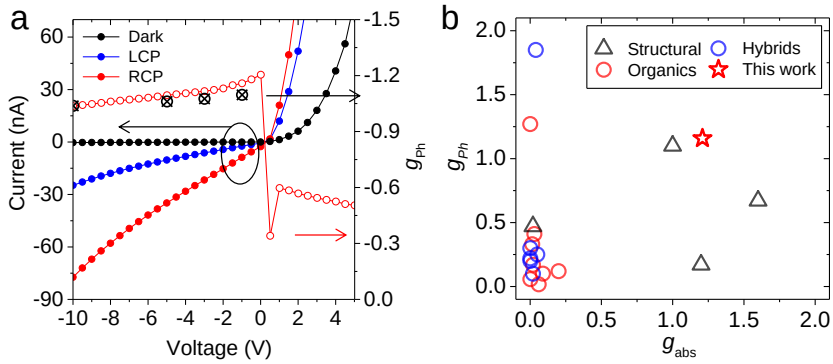

Figure 4.38. Device performances of CP photodetectors based on chiral doped polymeric films. a, Current–voltage (*I*–*V*) characteristics and corresponding g_{ph} values of the optimized CP photodetectors. The g_{ph} values recorded in time-dependent SAM detection are marked as dots. **b**, Correlation between dissymmetric factors in photocurrent and absorption in reported studies. Related references are provided in **Table 4.2**.

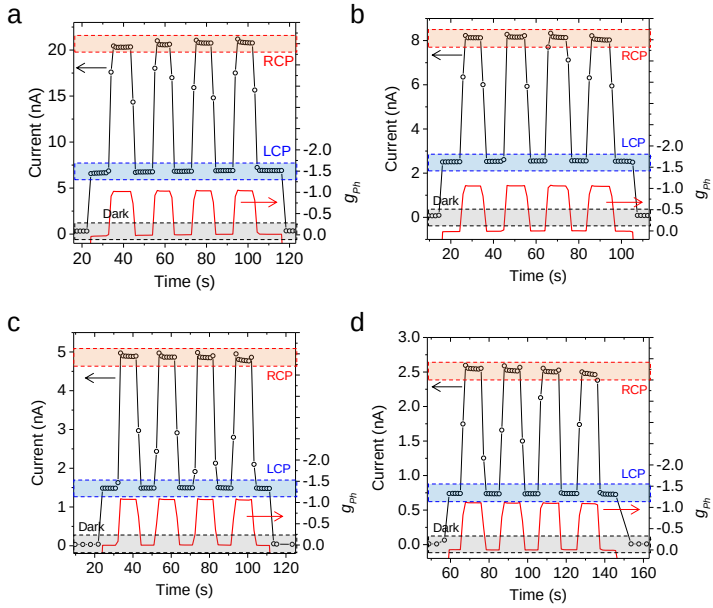

Figure 4.39. Time-dependent spin angular momentum detection and the corresponding g_{Ph} values. a–d, −10 V (**a**), −5 V (**b**), −3 V (**c**), and −1 V (**d**).

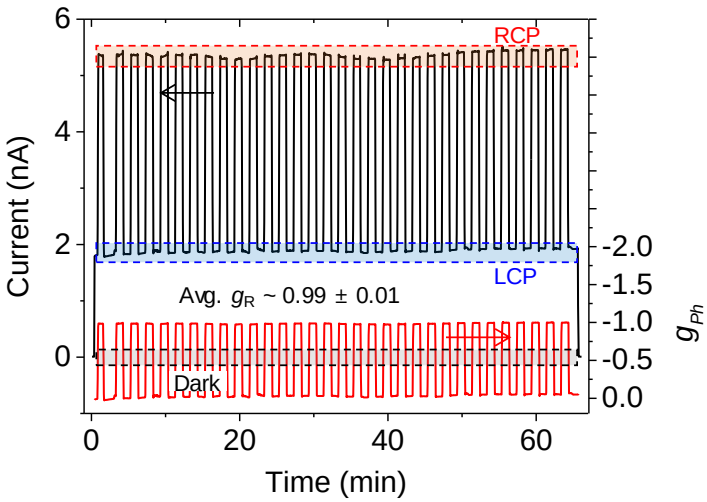

Figure 4.40. Long-term stability test results of CP photodetectors.

Table 4.2. Summarized chiroptical and optoelectronic performances of electronic devices in reported studies.

Number (Ref)	Article	CD type	Operation	Voltage(V)	Wave length(nm)	g_{abs}	g_{ph}	EQE (%)
1[38]	*Adv. Mater.* **22**, E131 (2010)	Organic	Photovoltaic	0	543	0.06	0.017	
2[39]	*Nat. Photonics*, **7**, 634 (2013)	Organic	Phototransistor	$V_D = -60$ $V_G = -5$	365		1.8	0.1
3[4]	*Nat. Commun.* **6**, 8379 (2015)	Plasmonic	Photovoltaic	0	1340	1	1.1	0.2
4[40]	*Sci. Rep.* **6**, 19580 (2016)	Chiral mirror	Photoconductor	0.1	635	1.2	0.17	30
5[41]	*Adv. Mater.* **29**, 1605828 (2017)	Organic	Phototransistor	$V_D = 70$ $V_G = 70$	460	0.015	0.33	88100
6[7]	*Adv. Funct. Mater.* **29**, 1805279 (2019)	Chiral mirror	Phototransistor	$V_D = 1.5$ $V_G = -2$	405	1.6	0.67	
7[20]	*Adv. Funct. Mater.* **29**, 1808668 (2019)	Organic	Photoconductor	5	375		0.1	0.15
8[42]	*Adv. Funct. Mater.* **29**, 1900684 (2019)	Organic	Photovoltaic	0	543	0.09	0.1	50
9[12]	*Nat. Commun.* **10**, 1927 (2019)	Hybrid	Photoconductor	10	395	0.02	0.1	39
10[43]	*Opt. Lett.* **44**, 2998 (2019)	Plasmonic	Photovoltaic	0	3800		1.3	1.1e-05
11[44]	*ACS Nano* **13**, 3659-3665 (2019)	Hybrid	Photoconductor	3	518		0.1	108
12[45]	*Angew. Chem. Int. Ed.* **59**,6442–6450 (2020)	Hybrid	Photoconductor	10	532	0.002	0.2	9.1
13[11]	*Science Advances* **6**, 3274–3285 (2020)	Hybrid	Photoconductor	−0.5	395	0.04	1.85	87.5
14[46]	*J. Mater. Chem. C* **8**, 9271-9275 (2020)	Organic	Phototransistor	$V_D = -60$ $V_G = -60$	450		1.94	0.016
15[47]	*ACS Nano* **14**, 14146-14156 (2020)	Organic	Phototransistor	$V_D = 10$ $V_G = 10$	495		0.129	3e5

Number (Ref)	Article	CD type	Operation	Voltage(V)	Wave length(nm)	gabs	gph	EQE (%)
16[8]	Adv. Funct. Mater. 30, 2006236 (2020)	Chiral mirror	Phototransistor	VD = −60 VG = −3	830		1.9	4.5e4
17[9]	Adv. Mater. 33, 2004115 (2021)	Organic	Phototransistor	VD = 20 VG = 10	405	0.0006	1.27	
18[18]	Adv. Optical Mater. 10, 2101044 (2021)	Organic	Photoconductor	−0.5 −1	510 455	0.03 0.2	0.41 0.12	8.4 5.2
19[10]	Nat. Commun. 12, 142 (2021)	Organic	Phototransistor	VD = −80 VG = −40	730	0.002	0.057	89
20[48]	ACS Nano 15, 7608-7617 (2021)	Hybrid	Phototransistor	VD = −2 VG = 0	405	0.056	0.25	1.38e5
21[49]	Angew. Chem. Int. Ed. 60, 8415-8418 (2021)	Hybrid	Photovoltaic Photoconductor	0 5	520	0.0015	0.3 0.22	 0.005
22[50]	ACS Materials Lett. 4, 401−409 (2022)	Organic	Photovoltaic	0	606	0.02	0.17	57
23[51]	Adv. Sci. 9, 2104598 (2022)	Plasmonic	Photovoltaic	0	808	0.02	0.47	77.7
24	(This work)	Organic	Photoconductor	−10	405 532 670	0.84 0.38 1.21	1.02 0.44 1.16	120 19 11

4.2.8. Effect of Device Structure on Dissymmetric Properties

Spin-current conversion was systematically investigated to understand the chiroptical activities and the mechanisms of signal transduction. Unlike optical properties, high-performance SAM detection requires electronic sensors with a delicate device configuration design. The g_{ph} values and D^* as functions of the chiral additive concentration and film thickness were investigated to determine the impact of the chiral templating phenomenon on chiroptical properties (**Figure 4.41**). Chiroptical activities increased as the dopant concentration increased, with saturated g_{Ph} values in equivalent weight blends; this finding indicated that extensive dopant loading would be necessary to maximize the chiral templating effect via noncovalent bonding with the polymer backbone. Notably, the chiral insulators did not affect photocurrent conversion performance because of efficient sublimation in the thermally activated chiral templating process. Therefore, it was decided to incorporate 50 wt% dopant to maximize the spin detection capabilities without reducing electrical readout performances.

By comparison, spin-to-photocurrent conversion performances were substantially affected by the active layer thickness. The D^* decreased with increasing active layer thickness because thick active layers limited charge carrier mobility and led to the recombination of photogenerated charge carriers before they reached the relevant electrodes.[52-53] g_{Ph} values increased with increasing active layer thickness; they reached a maximum at ~400 nm but were not saturated, in contrast to the dissymmetric factors in the absorption spectra. The observed mismatch of optimal thickness in CD and CP photoresponsivity (**Figure 4.14b**, and **4.41b**) presumably occurred because the incident photon-to-photocurrent conversion process was strongly dependent on photodetector device configuration.

Spin-electronic signal conversion properties were investigated for different device configurations to better understand the chiroptical activities and the photocurrent conversion principle. Modulation of the effective photoconversion area and fast

carrier transport without recombination is critical for the high dissymmetric factor in SAM detection. Photodetectors with symmetric gold electrodes configuration displayed weak parabolically shaped *I–V* curves that resulted from the two small Schottky barriers connecting the symmetric electrodes (**Figure 4.42**). Strong dissymmetry in the photocurrent *g* factors occurred as a function of applied voltage; this finding was not observed under normal light or dark current. The effective absorption area for the photocurrent contribution was a narrow depletion region at each electrode–semiconductor interface, which was caused by exciton formation with high binding energy, limited carrier mobility, and fast recombination before collection. Under the reverse electric field, the effective photocurrent conversion area was localized on the top electrode; this resulted in higher selectivity toward spin direction because of the enhanced chiroptical activities on the free surface produced by the strong surface anchoring effect.

Asymmetric structures were studied to better understand control of the depletion region (**Figure 4.43**). They exhibited rectifying diode behavior with a rectification ratio of 10^2, which resulted in leakage-current suppression and photocurrent enhancement. The dissymmetric factors were significantly increased (g_{ph} ~1) in the reverse bias region which is attributed to several factors: (i) more effective photon absorption into the chiral active layer−MoO_3/Au interface because of an asymmetric Schottky barrier at a negative bias,[54-55] ii) efficient electron−hole pair dissociation and fast removal of photogenerated minor carriers in-channel because of prolonged photoexcited carrier lifetime and low carrier trapping rate in the broadened depletion regions,[54, 56-57] and iii) dark current suppression through the use of rectifying diodes to block electrode current. The different photocurrent conversion multiplication factors in the reverse and forward directions resulted in differential exponents with exponential dependencies on the absorbed number of photons; this led to enhanced dissymmetric spin detection in the reverse photoconductive mode.[54, 58-59] Under a high negative bias condition, the dissymmetric behavior dramatically diminished,

which originated from excessively wide interfacial barriers under high reverse bias and resulted in unclear photocurrent because the dark current was a more dominant component of the current flow.[55]

Introduction of zinc oxide layers, which are efficient hole blockers, sharply increased the rectification ratio (> 10^3) (**Figure 4.44**). The dark current decreased by approximately one order of magnitude, leading to better specific detectivities. Furthermore, the enhancement of rectifying properties led to increased *g* values throughout the bias region, especially in the high negative biased condition. The increased energy barrier suppressed charge injection under the strong bias, while maintaining the energy cascade to facilitate extraction of photogenerated carriers. In addition, chiroptical properties were enhanced in a self-powered condition because no external bias was needed to promote exciton dissociation due to sufficient built-in potential.

A fullerene derivative was introduced into the chiral active layer for interfacial trap-assisted hole tunneling injection because the chiral templating for the formation of helical structures decreased with increasing addition of fullerene derivative (**Figure 4.45**). This behavior was attributed to the absence of long-range ordering of polymer chains caused by the presence of the immiscible solid-state fullerene within the polymeric phase, which prohibited the formation of helical ordering through interactions with chiral dopants.[60] To intensify photomultiplication, a small amount (1 wt%) of phenyl-C71-butyric acid methyl ester ($PC_{70}BM$) was blended in the optimized devices. The trapped electrons induced interfacial band bending, which resulted in efficient hole tunneling injection from the external circuit under light illumination; this led to a photomultiplication (**Figure 4.46**).[61] The optimized structures displayed excellent photodetection properties without decreasing the *g* value (*g* value remained at 1.2 and D^* over 10^{11}) throughout the negative voltage sweep region (**Figure 4.47**). Importantly, dramatic enhancement of dissymmetric photodetection was observed under the forward bias condition, rather than under the

reverse bias condition. Distinct interfacial band bending according to the spin direction of incident photons occurred at the chiral active layer−MoO_3/Au interface because of the surface anchoring effect; this led to increased hole tunneling injection from the anode source and subsequent photocurrent conversion. Thus, the chiroptical activities could be modulated by systematic design of the photodetector configurations, thereby broadening the highly dissymmetric region for SAM detection in both photoconductive mode and photovoltaic photodiode operations (**Figure 4.48**).

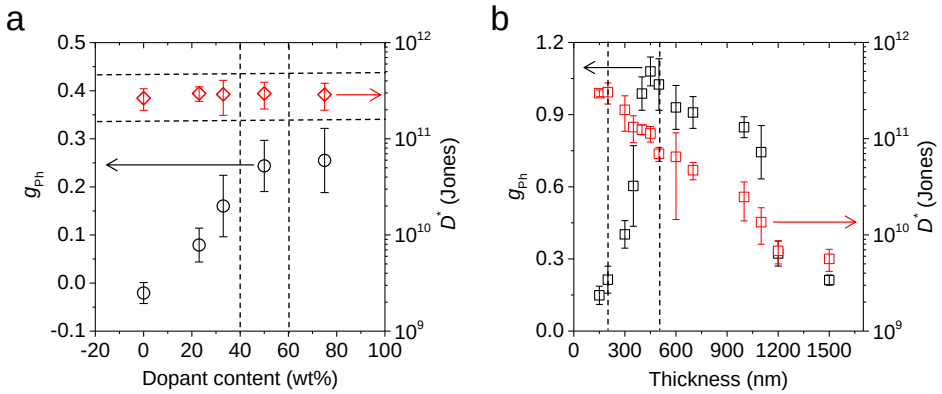

Figure 4.41. Specific detectivity and g_{Ph} values of CP photodetectors. a, b, Specific detectivity and g_{ph} values of CP photodetectors as a function of chiral dopant concentration (**a**) and chiral film thickness (**b**).

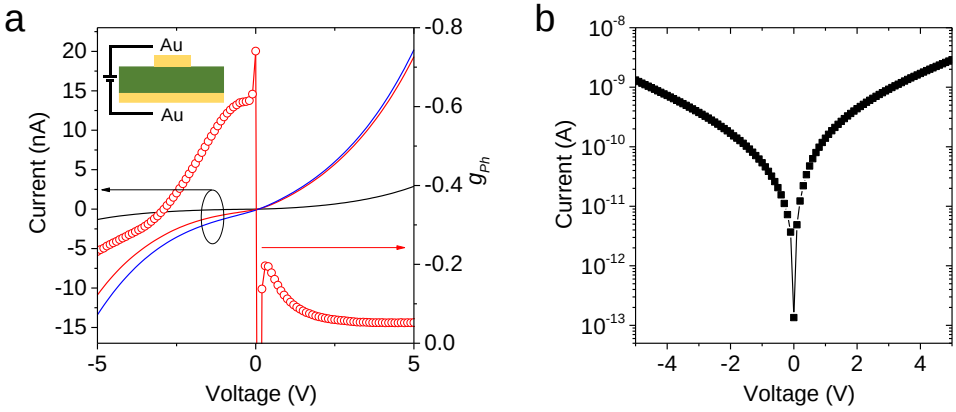

Figure 4.42. Device characteristics of the symmetric gold/active layer/gold configuration. a, Current–voltage (*I–V*) characteristics and corresponding g_{Ph} values upon circular polarization detection. **b**, *I–V* characteristics (log scale) of photodetectors in the dark condition.

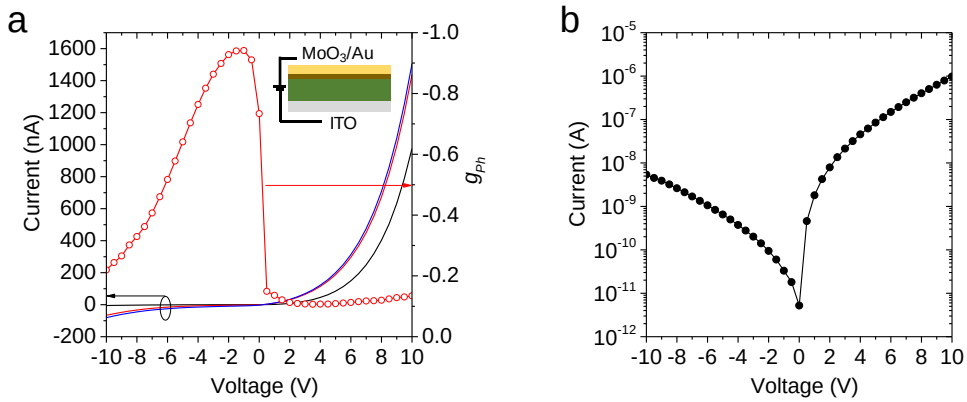

Figure 4.43. Device characteristics of the asymmetric ITO/active layer/gold configuration. a, Current–voltage (*I*–*V*) characteristics and corresponding g_{Ph} values upon circular polarization detection. **b**, *I*–*V* characteristics (log scale) of photodetectors in the dark condition.

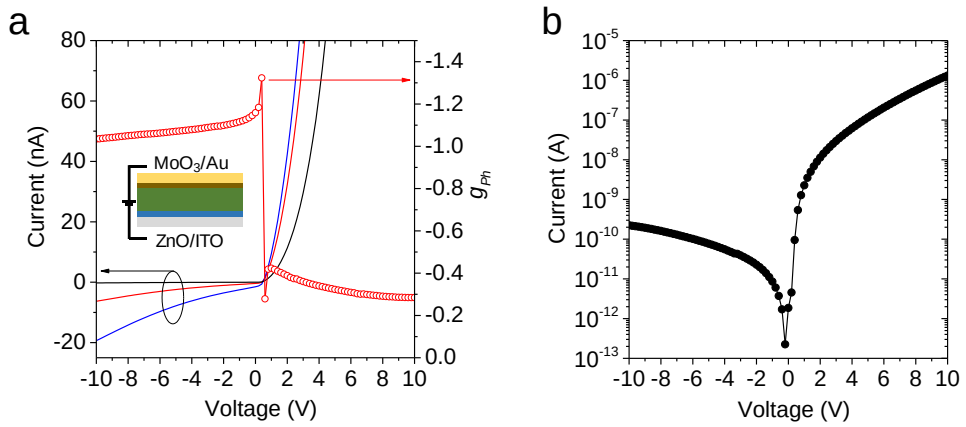

Figure 4.44. Device characteristics of the asymmetric ITO/ZnO/active layer/gold configuration. a, Current–voltage (*I*–*V*) characteristics and corresponding g_{Ph} values upon circular polarization detection. **b**, *I*–*V* characteristics (log scale) of photodetectors in the dark condition.

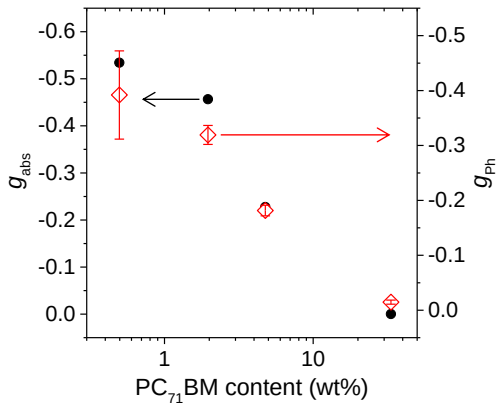

Figure 4.45. g_{abs} and g_{Ph} values of circular polarization photodetectors as a function of blended $PC_{70}BM$ ratio.

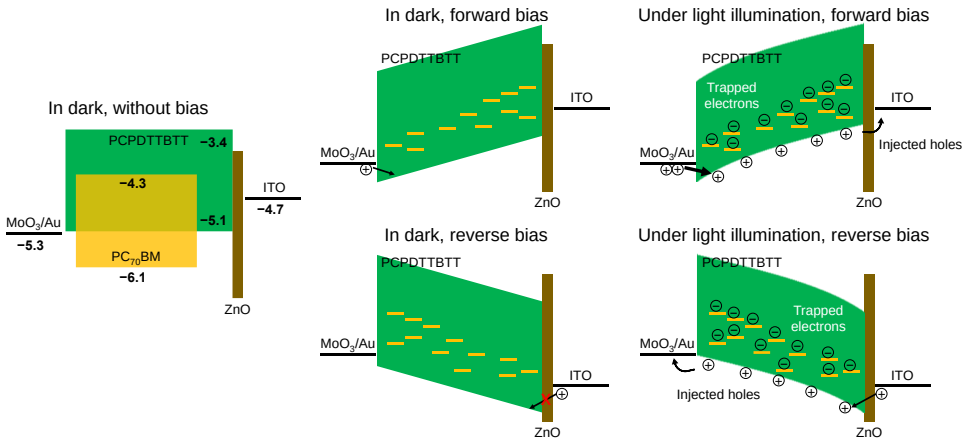

Figure 4.46. Schematic illustrations of the photomultiplication of charge carriers in the polymer film. Schematic illustrations of the working principles of the photomultiplication effect by interfacial trap-assisted hole tunneling injection according to the applied voltage and light illumination.

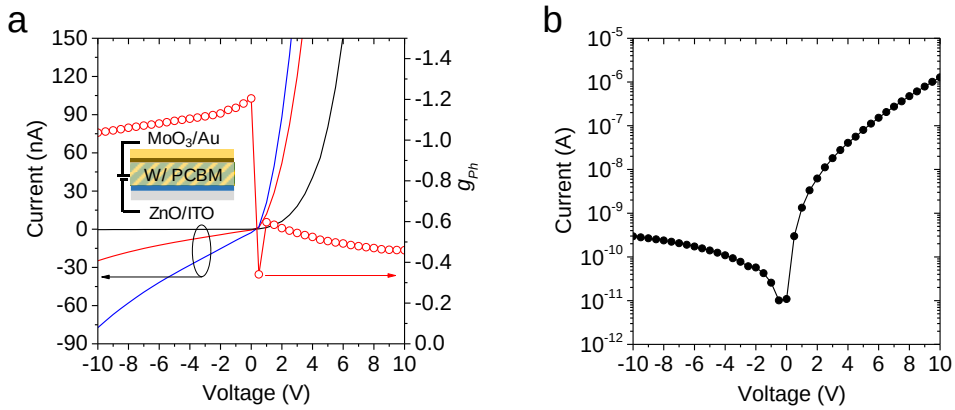

Figure 4.47. Device characteristics of the asymmetric ITO/ZnO/active layer (with 1 wt% $PC_{70}BM$)/gold configuration. a, Current–voltage (*I–V*) characteristics and corresponding g_{Ph} values upon circularly polarized light detection. **b**, *I–V* characteristics (log scale) of photodetectors in the dark condition.

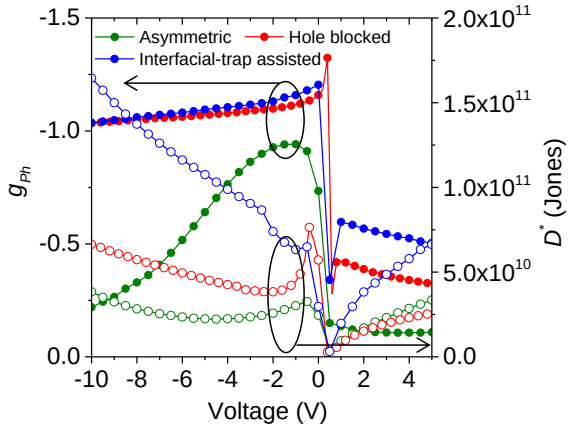

Figure 4.48. g_{Ph} and specific detectivity of circularly polarized photodetectors with various device configurations. Device configuration was as follows: green, ITO/active layer/MoO_3/Au; red, ITO/ZnO/active layer/MoO_3/Au; blue, ITO/ZnO/active layer (with 1 wt% $PC_{70}BM$)/MoO_3/Au.

4.2.9. Optical Activities of Chiral Doped Polymeric Films

The photodetectors exhibited highly selective broadband SAM detection at the peak position of the bisignate CD spectra because of excitonic coupling in both π–π* and charge-transfer transitions, indicating efficient conversion from CD absorption to electronic signals in the photon excitation mode (**Figure 4.49**).

SAM detection using the homogeneous system enabled delicate extraction of helicity information regarding unknown elliptically polarized beams, rather than a simple linearly or circularly polarized state (i.e., S_3 Stokes parameter or degree of circular polarization (DoCP); **Figure 4.50**). The photocurrent as a function of DoCP was fitted with theoretical estimates for the helicity-resolved component of the incident beam. Thus, in addition to the previously reported detection of CP in the presence of linear anisotropy derived from electrode geometry,[5-6] our homogeneous chiral system can measure the DoCP of elliptically polarized light.

To further understand the optical activities, I investigated chiroptical properties by considering the conditions of light–matter interaction (**Figure 4.51**). Upon rotation of the azimuthal angle and reversal of the angle of incident light, I observed no difference in chiroptical properties, indicating that they did not originate from the product of linear dichroism and birefringence.[14, 62] Furthermore, the optical information inferred from M_{14} and M_{41} recorded by Mueller matrix spectroscopic ellipsometry (MMSE) revealed that the CD in transmission mainly contributed to the CD in absorption, but the CD in reflection was almost negligible at all oblique incidences (**Figure 4.52−63**). These results indicated that our chiroptical properties were caused by true optical activity, rather than inhomogeneous structural chirality-based Bragg reflection.[17, 63] The electrical readouts of both circularly and elliptically polarized light were tested by varying the horizontal axis of the CP beam. Indeed, the CP photodetectors showed highly sensitive DoCP detection in arbitrary azimuthal orientation, enabling circular polarization imaging for targets of which the anisotropic axis is invisible or unknown (**Figure 4.64a**). The incident angle of

polarized beam could be a dominant factor for SAM detection. In an inhomogeneous system, the operating range and DoCP sensitivity are seriously limited by the oblique incident conditions of both circularly and partially polarized light.[8, 63] However, our CP photodetectors showed uniform D^* and g values when the angle of incident light varied from 0° to 32° (**Figure 4.64b**).

Such optical properties and sensitive detection of circular polarization with g_{Ph} ~0.67 maximize the signal transduction for three-state optical signals exhibited 67% faster information transfer, compared with conventional binary notation-based information transfer (**Figure 4.65**), which make these polymers promising for optical communication and computing. It was demonstrated that dissymmetric optical sensors can effectively transfer the spin information of elliptically polarized beams into clearly discriminated 21-multibit electrical signals (**Figure. 4.66**).

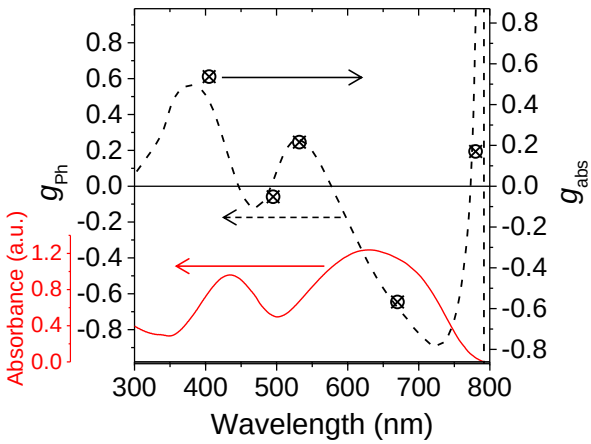

Figure 4.49. Comparison graph g_{ph} of CP photodetector and g_{abs} of chiral doped polymeric layer. CP beam detection characteristics (dots) and CD spectrum (dashed line) in the ultraviolet-visible absorption region (red line).

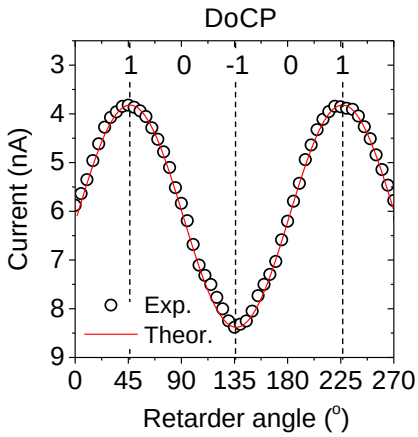

Figure 4.50. Experimentally measured photocurrent values and fitting results. Fitting was calculated according to the equation $I_{PC} = Csin(2\theta + \varphi_c)$.

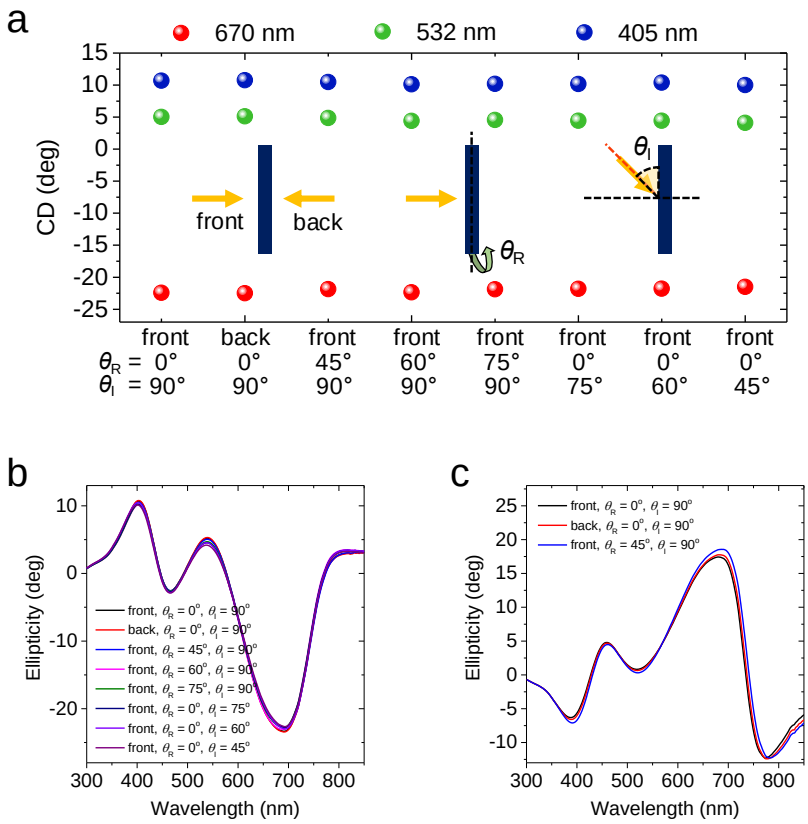

Figure 4.51. Optical activities of chiral doped polymeric films. a, Chiroptical properties considering the azimuthal rotation and flipping of samples and the angle of incident light. **b**, **c**, S5011-doped (**b**) and R5011-doped (**c**) PCPDTTBTT films considering the azimuthal sample rotation, sample flipping, and incidence angle modulation (θ_R: rotation angle of the sample; θ_I: incidence angle of the beam).

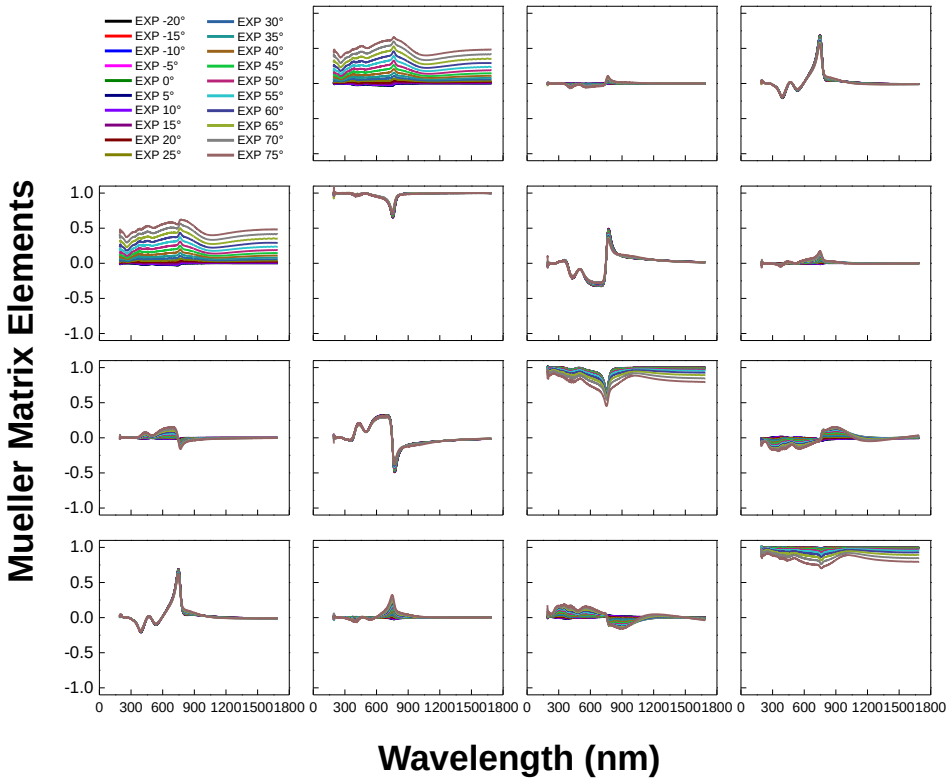

Figure 4.52. Mueller matrix spectroscopic ellipsometry data of the R5011-doped PCPDTTBTT film. MMSE data were recorded in transmission mode with 0° azimuthal sample rotation. EXP indicates the installation angle between the incident light path and the normal light path to the substrate surface.

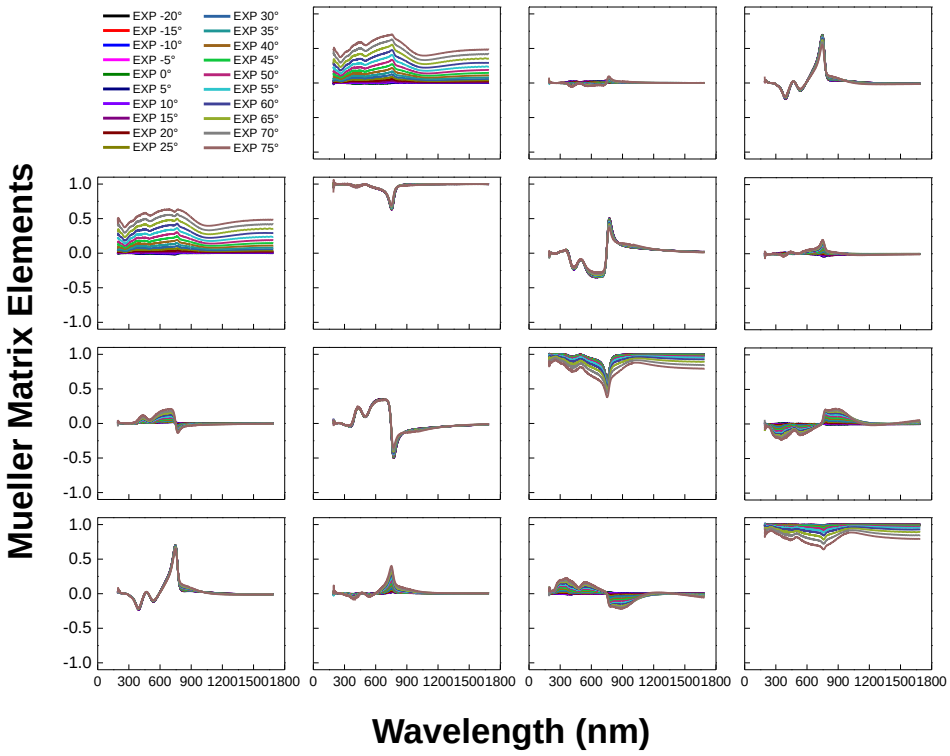

Figure 4.53. Mueller matrix spectroscopic ellipsometry data of the R5011-doped PCPDTTBTT film. MMSE data were recorded in transmission mode with 45° azimuthal sample rotation. EXP indicates the installation angle between the incident light path and the normal light path to the substrate surface.

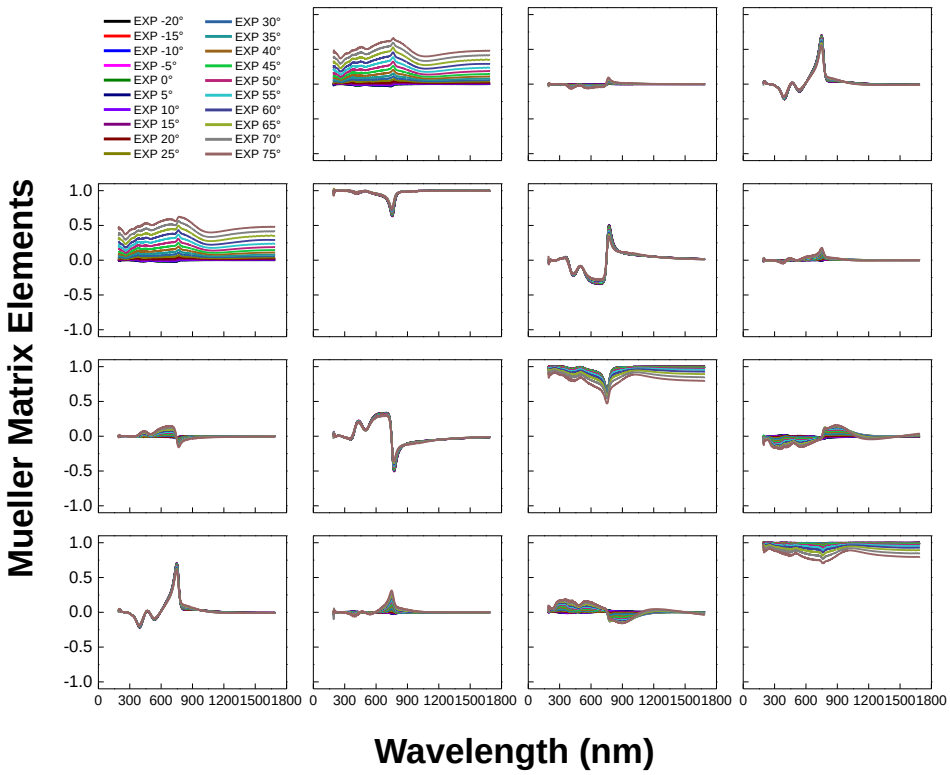

Figure 4.54. Mueller matrix spectroscopic ellipsometry data of the R5011-doped PCPDTTBTT film. MMSE data were recorded in transmission mode with 90° azimuthal sample rotation. EXP indicates the installation angle between the incident light path and the normal light path to the substrate surface.

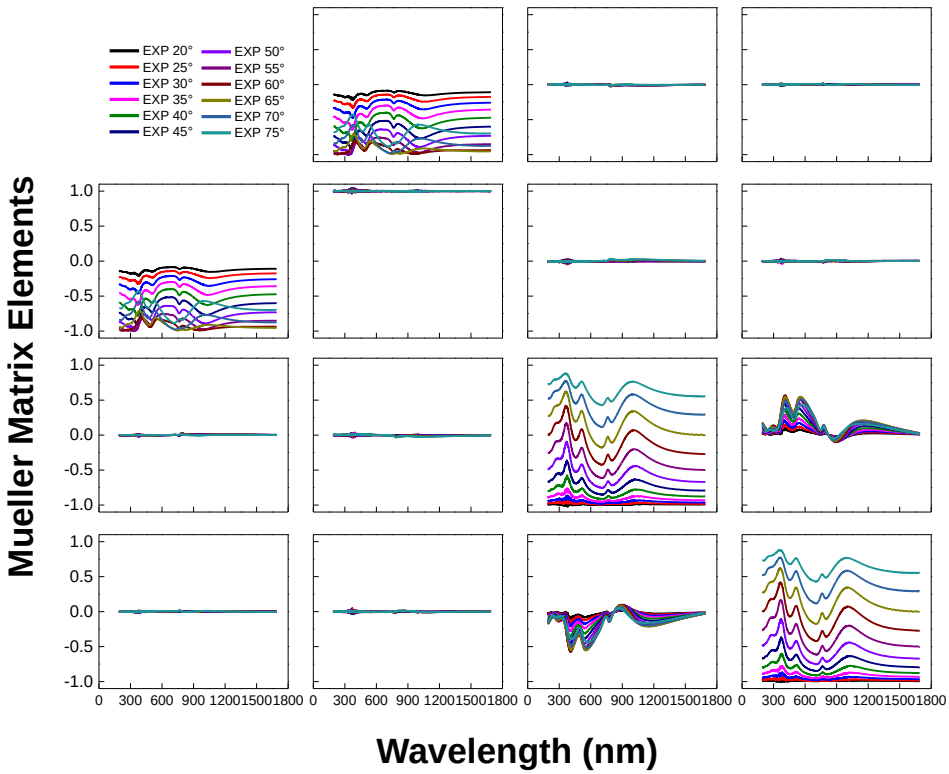

Figure 4.55. Mueller matrix spectroscopic ellipsometry data of the R5011-doped PCPDTTBTT film. MMSE data were recorded in reflection mode with 0° azimuthal sample rotation. EXP indicates the installation angle between the incident light path and the normal light path to the substrate surface.

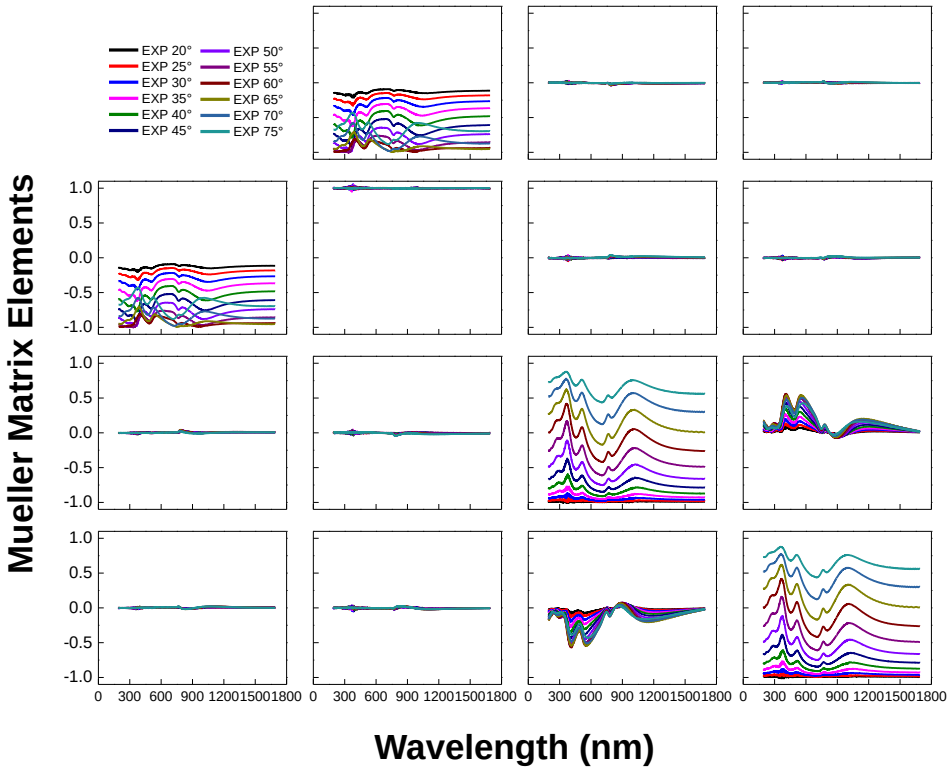

Figure 4.56. Mueller matrix spectroscopic ellipsometry data of the R5011-doped PCPDTTBTT film. MMSE data were recorded in reflection mode with 45° azimuthal sample rotation. EXP indicates the installation angle between the incident light path and the normal light path to the substrate surface.

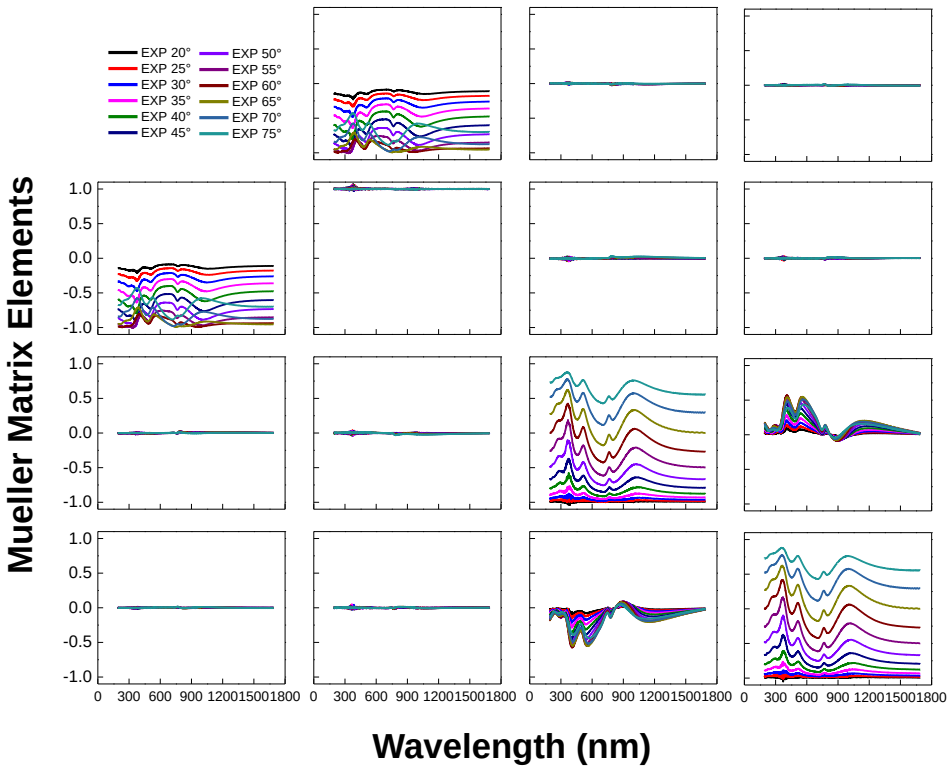

Figure 4.57. Mueller matrix spectroscopic ellipsometry data of the R5011-doped PCPDTTBTT film. MMSE data were recorded in reflection mode with 90° azimuthal sample rotation. EXP indicates the installation angle between the incident light path and the normal light path to the substrate surface.

\

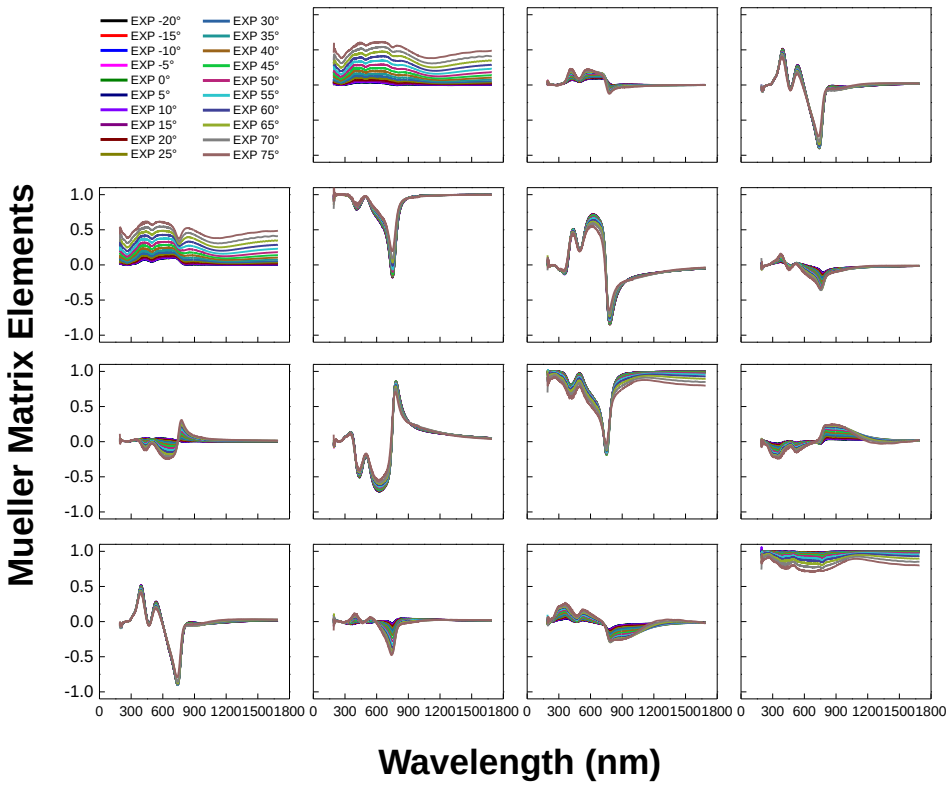

Figure 4.58. Mueller matrix spectroscopic ellipsometry data of the S5011-doped PCPDTTBTT film. MMSE data were recorded in transmission mode with 0° azimuthal sample rotation. EXP indicates the installation angle between the incident light path and the normal light path to the substrate surface.

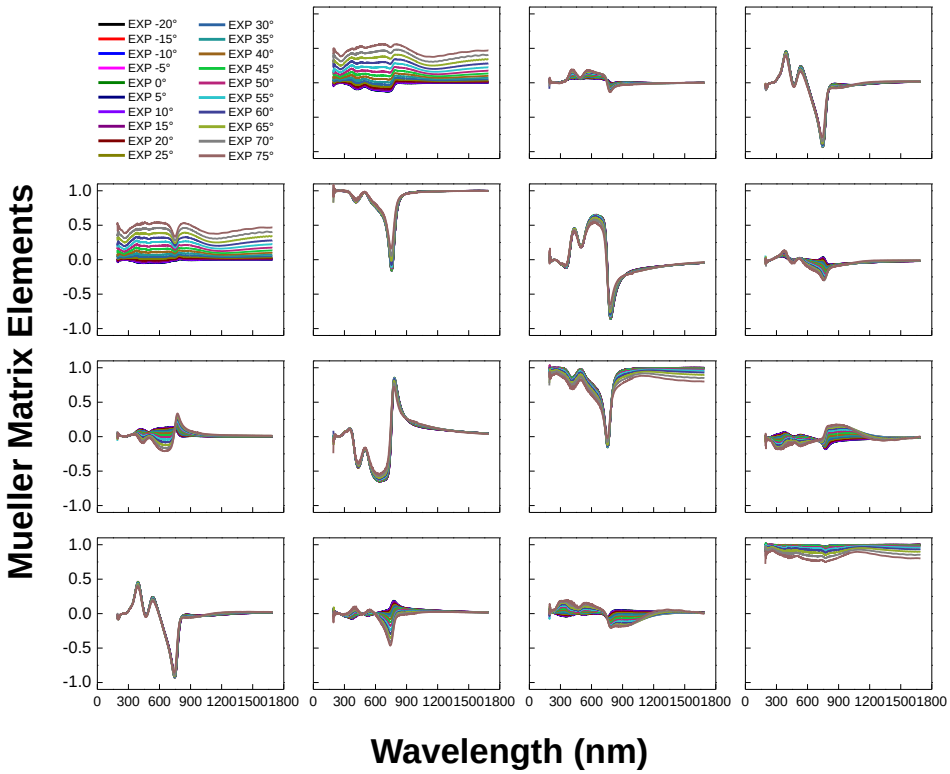

Figure 4.59. Mueller matrix spectroscopic ellipsometry data of the S5011-doped PCPDTTBTT film. MMSE data were recorded in transmission mode with 45° azimuthal sample rotation. EXP indicates the installation angle between the incident light path and the normal light path to the substrate surface.

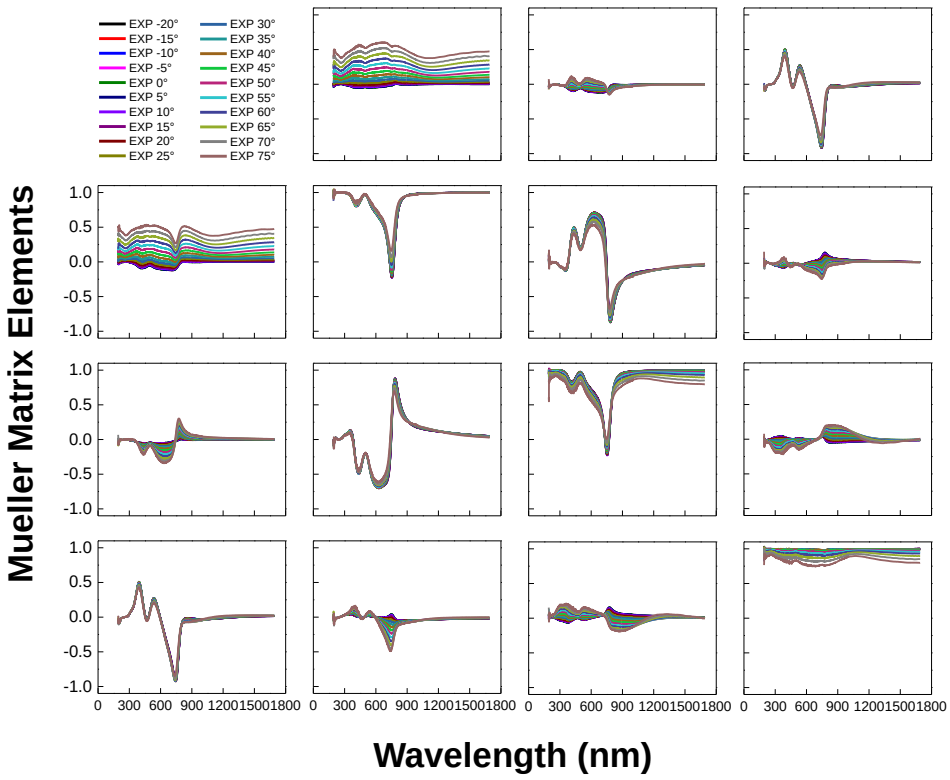

Figure 4.60. Mueller matrix spectroscopic ellipsometry data of the S5011-doped PCPDTTBTT film. MMSE data were recorded in transmission mode with 90° azimuthal sample rotation. EXP indicates the installation angle between the incident light path and the normal light path to the substrate surface.

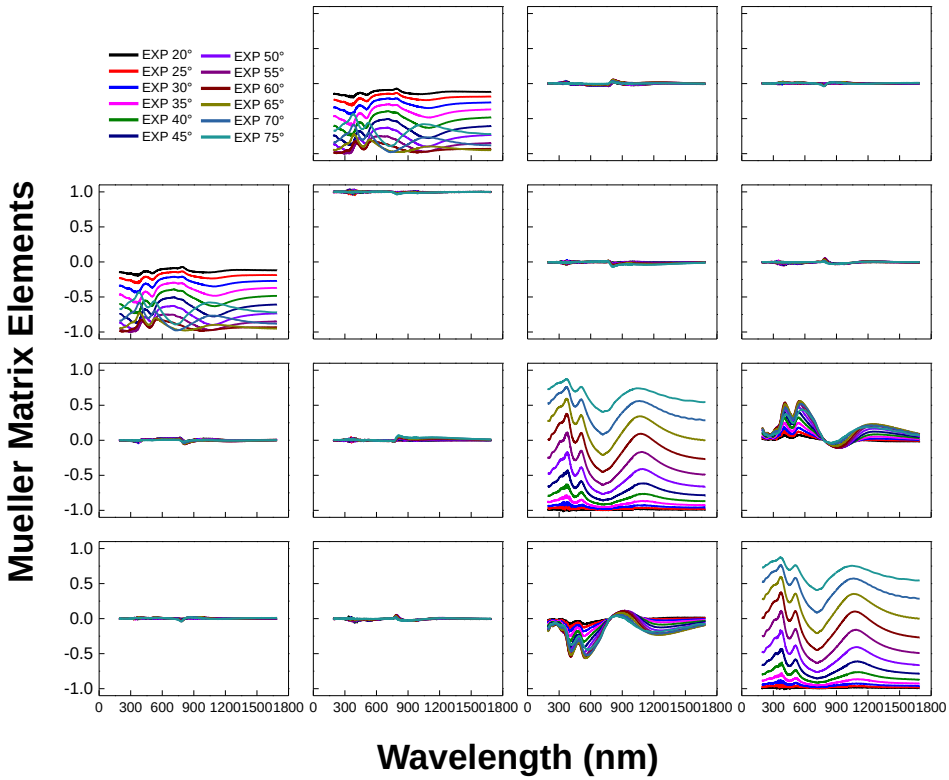

Figure 4.61. Mueller matrix spectroscopic ellipsometry data of the S5011-doped PCPDTTBTT film. MMSE data were recorded in reflection mode with 0° azimuthal sample rotation. EXP indicates the installation angle between the incident light path and the normal light path to the substrate surface.

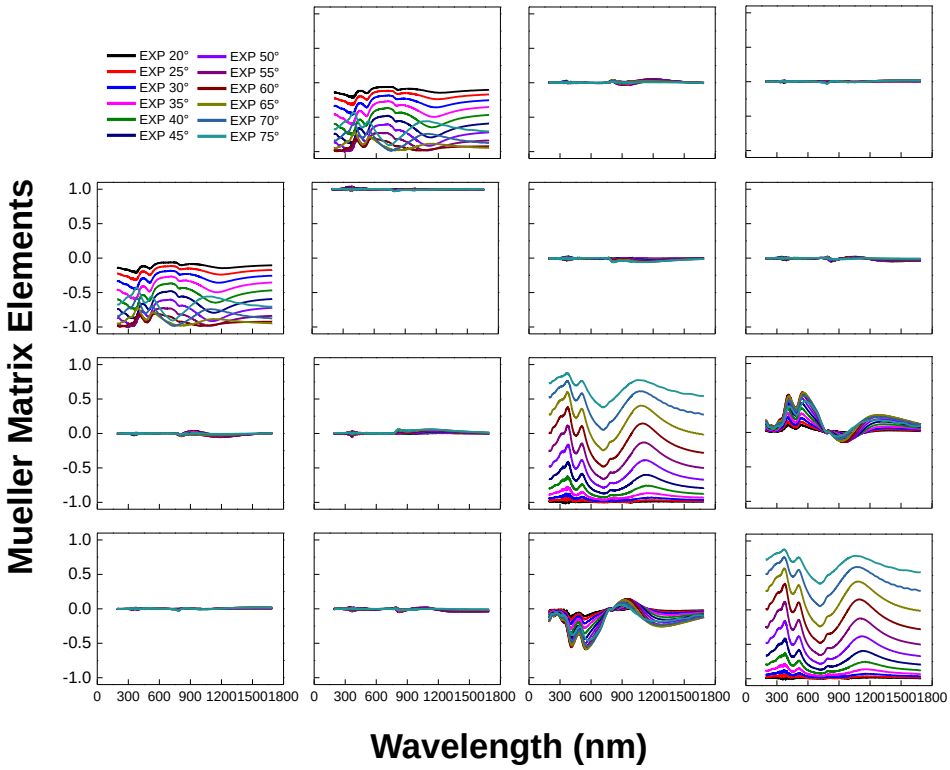

Figure 4.62. Mueller matrix spectroscopic ellipsometry data of the S5011-doped PCPDTTBTT film. MMSE data were recorded in reflection mode with 45° azimuthal sample rotation. EXP indicates the installation angle between the incident light path and the normal light path to the substrate surface.

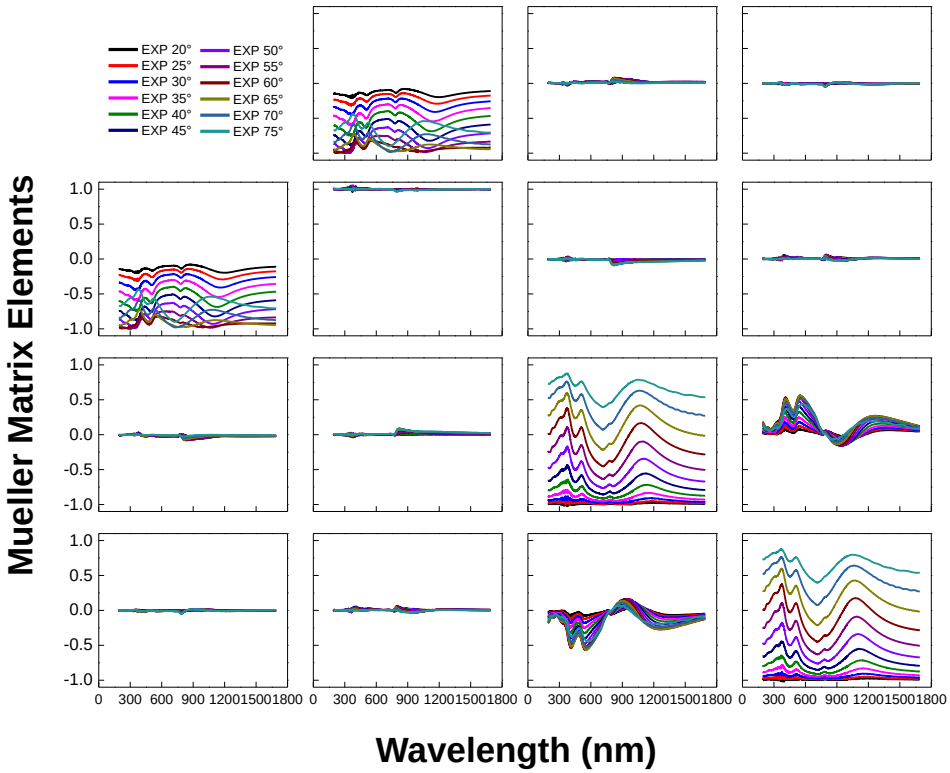

Figure 4.63. Mueller matrix spectroscopic ellipsometry data of the S5011-doped PCPDTTBTT film. MMSE data were recorded in reflection mode with 90° azimuthal sample rotation. EXP indicates the installation angle between the incident light path and the normal light path to the substrate surface.

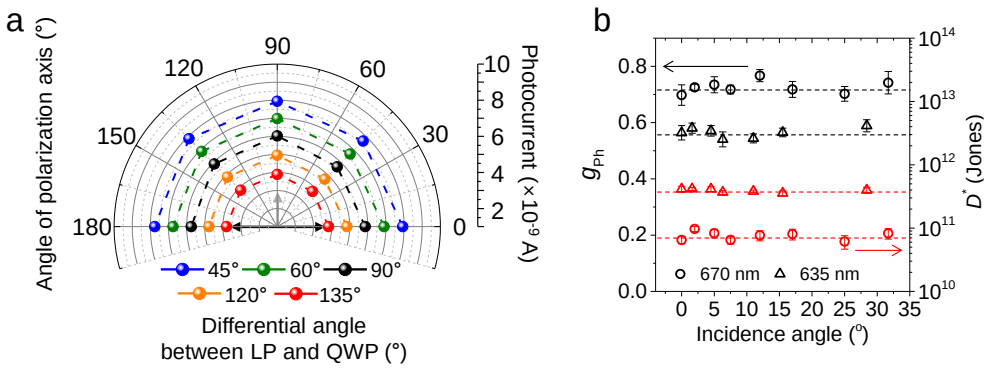

Figure 4.64. Highly sensitive and uniform CP beam detection in various incident beam condition. a, Electrical readout according to linear polarization axis and retarder angle. **b**, D^* and g_{Ph} values at light wavelengths of 635 and 670 nm as a function of incidence angle.

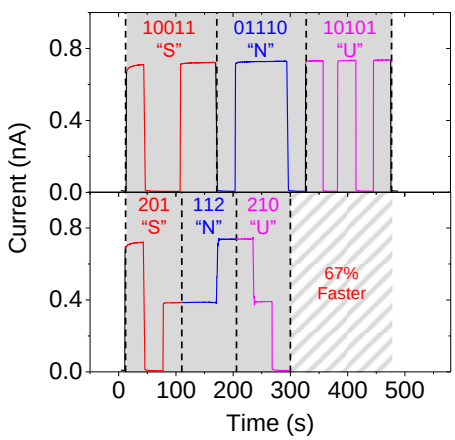

	A	B	C	D	E	F
Binary	00001	00010	00011	00100	00101	00110
Ternary	001	002	010	011	012	020
	N	O	P	Q	R	S
Binary	01110	01111	10000	10001	010010	10011
Ternary	112	120	121	122	200	201

G	H	I	J	K	L	M
00111	01000	01001	01010	01011	01100	01101
021	022	100	101	102	110	111
T	U	V	X	X	Y	Z
10100	10101	10110	10111	11000	11001	11010
202	210	211	212	220	221	222

Figure 4.65. Ternary notation application of CP photodetectors. Current was recorded in the CP photodetectors under three incident light conditions (dark, left-handed circularly polarized [LCP], and right-handed circularly polarized [RCP]) for ternary notation-based information transfer (bottom); it was recorded using conventional binary notation as a comparison (top). Binary and ternary notations are described in the table on the right.

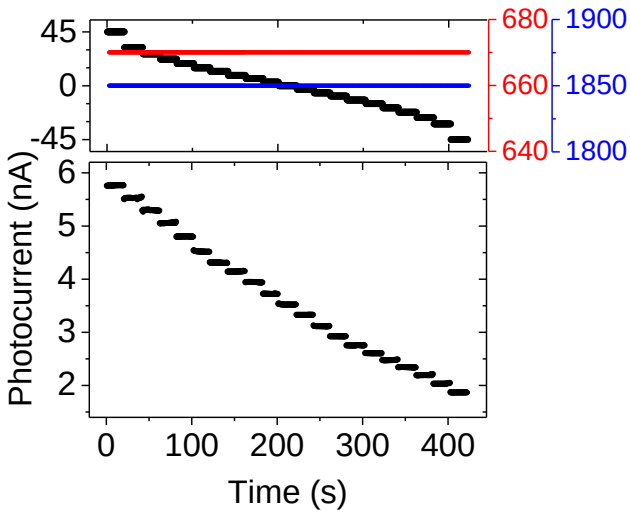

Figure 4.66. 21-Multibit electrical readout according to optical helicity information. In the top graph, the black line corresponds to the angle between the linear polarizer and the quarter-wave plate (°), the red line corresponds to the wavelength (nm), and the blue line corresponds to the light intensity (μW cm^{-2}).

4.2.10. Spin Angular Momentum Sensing and Spin Helicity Trajectory Visualization

Furthermore, the homochiral active layers could be incorporated into a large-scale spin-electric imaging system. A 30 × 30 matrix of CP photodetectors was demonstrated at the 3 × 3 cm^2 scale without additional optical set-up; the light-exposed region was expressed in recorded 2D photocurrent maps (**Figure 4.67a–c**, **Figure 4.68**). The differential 2D patterns, which constituted simple "heart-shaped" images under conventional detection, were clearly detected in the recorded photocurrent under the CP detection mode. The CP photodetector arrays efficiently and uniformly distinguished spin helicity, regardless of the exposed area and incident angle.

High sensitivity and robustness of polarization imaging and information processing by large-area homogeneous films was verified using a customized software-controlled multichannel data acquisition system (**Figure 4.67d**). An 8 × 8 passive matrix array was fabricated to demonstrate multiple signal imaging. When a pixel was illuminated with CP light, the resistance of the chiral active layer decreased compared with the external reference resistors, leading to the enhancement of terminal conversion values. Optimization of the resistance and dissymmetry factors of the chiral media provided a three-state electrical readout (digital conversion value: 0 for the dark state, 1 for the LCP beam, and 2 for the RCP beam). The light trajectory and spin helicity detection in real-time imaging were demonstrated by irradiation with a red CP beam (**Figure 4.69**). As the beam spot was moved, the digital readout exhibited well-resolved real-time spatiotemporal imaging of the SAM trajectory. The imaging speed was mainly determined by addressing units for 16 pins in our passive matrix systems, leading to a terminal capture rate of 23.9 Hz for a single frame and 1.53 kHz for a single node (**Figure 4.70**). Moreover, the spin helicity conversion of CP beams was clearly visualized by the changes in digital conversion values

according to the handedness of incident CP beams (**Figure 4.67e**). The developed prototype large-area CP photodetector array enabled real-time SAM detection and imaging over a large area; this is expected to be useful in next-generation optoelectronics, such as polarization imaging and cryptographic communication.

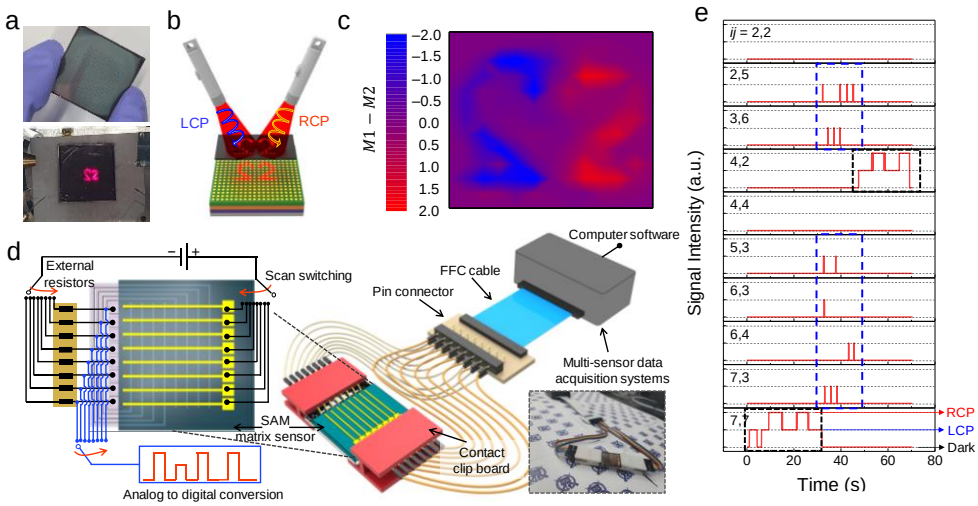

Figure 4.67. SAM sensing and spin helicity trajectory visualization. a, b, Photographs (**a**) and schematic illustration (**b**) of 30 × 30 photodiode arrays. **C**, Two-dimensional photocurrent mapping recorded in circularly polarized (CP) photodetection mode. As CP beams with opposite directions were alternately irradiated in "S" and "2" patterns, $\frac{I_{LCP}-I_{RCP}}{I_{dark}}$ became negative on the "S" pattern and thus $\frac{I_{RCP}-I_{LCP}}{I_{dark}}$ became positive on the "2" pattern. **d**, Schematic illustration and photograph of the passive matrix-based real-time imaging system. The respective pixels were selected with the row and column multiplexer. **e**, Recorded pixel-by-pixel digital signals upon moving and changing the CP state. Black dotted squares correspond to spin helicity trajectory and blue squares correspond to beam spot migration.

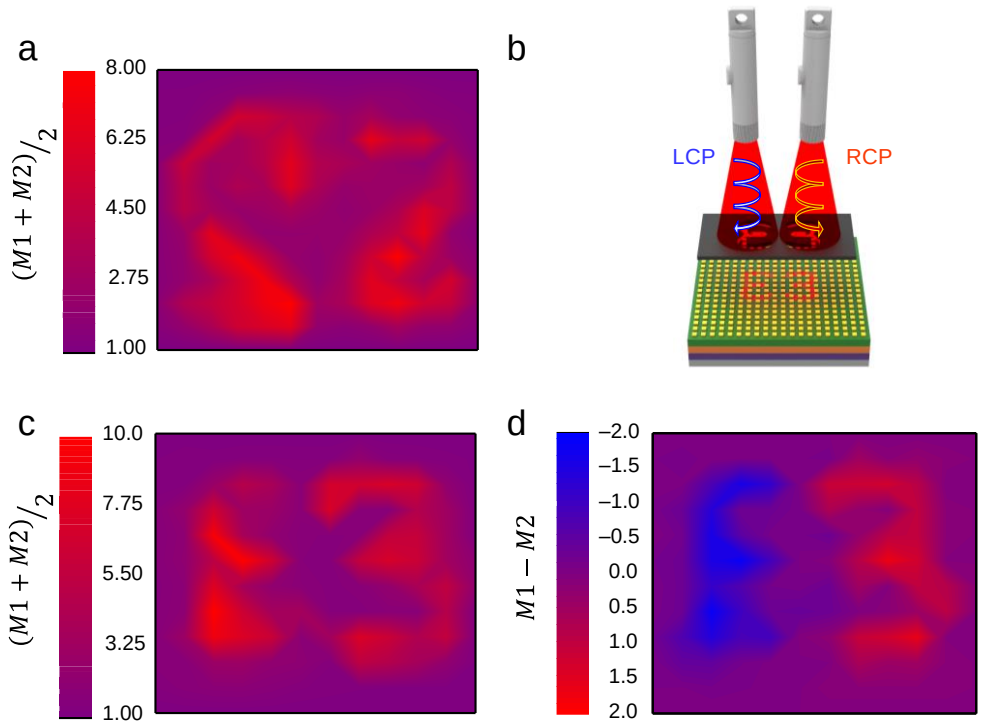

Figure 4.68. CP 30 × 30 matrix photodetector irradiated with the opposite handedness of the CP beam and corresponding photocurrent mapping. a, Two-dimensional (2D) photocurrent map recorded in conventional photodetection mode with oblique irradiation incident angle of 10°. **b**, Schematic illustration of 30 × 30 photodiode arrays with normal angle of incident light shaped "Ɛ" or "3". **c, d**, Corresponding comparison 2D histograms in conventional photodetection mode exhibiting simple "clover" shape (**c**) and in CP detection mode representing distinguishable "Ɛ" and "3" (**d**).

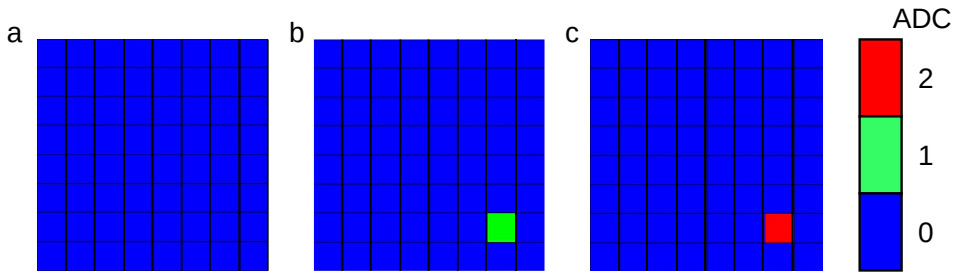

Figure 4.69. Real-time spin helicity detection and imaging results. a–c, Polarization imaging results of the passive matrix array represented in customized software in the dark condition (**a**), under LCP (**b**), and RCP (**c**) light irradiation.

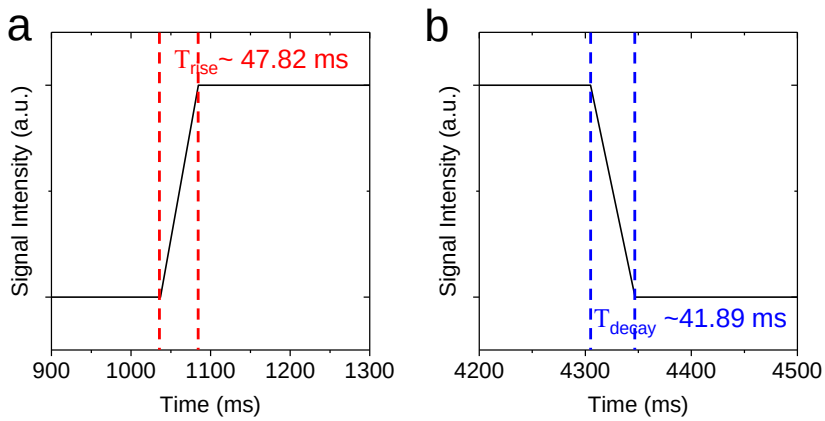

Figure 4.70. Time-dependent signal intensity of the passive matrix arrays. a, **b**, Recorded signal intensity of the passive matrix arrays as a function of time with the circularly irradiating polarized beam on (**a**) and off (**b**).

4.3. Conclusion

In conclusion, it was shown that chiral transient templating using volatile chiral additives is a powerful tool for the preparation of a homochiral CP-active medium via helical columnar ordering of submicron-sized nanofibrils; it can achieve strong, long-range, inter-chromophore chiral communication due to highly polarizability of conjugated polymers. The chiroptical layers from such polymers enabled ultraviolet-visible–near infrared (UV-vis–NIR) broadband spin-to-current conversion regardless of the incident angle of the CP beam and highly sensitive measurement of the SAM of incident photons with a *g* factor as high as ~1.2. The polymer-based CP photodetector enabled real-time spatiotemporal visualization of the spin state of light over a large area demonstrating the possibility to utilize of the spin state of light for optical communication and SAM-based next-generation quantum computation/networking with on-chip integrated spin-quantum optoelectronics.

4.4. Experimental Details

4.4.1. Materials

Anhydrous toluene, diethyl zinc solution (15 wt% in toluene), tetrahydrofuran, and chiral additives ((*R*)- or (*S*)-BN, *L*- or *D*-cysteine) were obtained from Sigma–Aldrich. Most other chiral additives ((*R*, *R*)- or (*S*, *S*)-TADDOL, R811 and S811, and CB15) were purchased from TCI. The chiral additives R5011 and S5011 were supplied by Daken Chemical. The conjugated polymers P3HT and PTB7-Th were purchased from EM Index and Solarmer Materials, respectively. F8T2 and MEH-PPV were supplied by Ossila. PCPDTTBTT and PDBT-co-TT were provided by Lumtec. All materials were used as received unless otherwise stated.

4.4.2. Characterization

All solutions were spin-coated on quartz plates without further treatment for CD and UV-vis spectroscopic examination, in which the active layers were thermally annealed for molecular rearrangements or not annealed for comparison. Differential scanning calorimetry (DSC) was conducted under a nitrogen atmosphere at a ramping rate of 10°C min^{-1} using a Discovery DSC instrument (TA Instruments). Thermogravimetric analysis (TGA) was conducted using a Discovery TGA instrument (TA Instruments). POM images were obtained using an Olympus BX53F microscope equipped with polarizers oriented in a perpendicular (crossed) arrangement. Film morphology, thickness, and roughness were analyzed via AFM (NX10; Park Systems) in True Non-Contact™ mode. AFM topography images were analyzed using Gwyddion software. SEM images were captured after 1 min of Pt sputtering using MERLIN Compact (Zeiss) and JSM-7800F Prime (JEOL) field-emission microscopes. Transmission electron microscopy images were obtained using a JEM-ARM200F instrument equipped with a cold field-emission gun (JEOL) operating at 80 kV. Absorption spectra were recorded using a V-770 UV-vis–NIR

spectrophotometer (JASCO). CD spectra were collected using J-815 and J-1500 spectropolarimeters (JASCO) at 298 K under a nitrogen atmosphere. ToF-SIMS (TOF.SIMS-5; ION-TOF) was performed in spectral mode using a 30-keV Bi^{3+} primary ion source at a current of 0.7 pA. Depth profiling was carried out under negative polarity. XPS and FTIR data were obtained using AXIS-His (KRATOS) and Frontier (PerkinElmer) instruments, respectively. Raman and scattered circular polarization ROA spectra were measured by Raman spectrometer (LabRam Aramis; Horiba Jobin Yvon) customized with linear polarizer and quarter-wave plate, using 514 nm wavelength laser excitation, <1 μW laser power at the sample, and 30 s acquisition times.

4.4.3. Analysis of Crystal Structure

GIWAXD measurements were conducted on the PLS-II 9A U-SAXS beamline at the Pohang Accelerator Laboratory in Korea. X-rays emitted from the in-vacuum undulator were monochromated at 11.025 keV (λ = 1.12454 Å) using a double-crystal monochromator, then focused both horizontally and vertically (450 μm (H) × 60 μm (V) in the full-width at half-maximum sample position) using K–B-type mirrors. The sample stage was equipped with a seven-axis motorized stage for fine alignment of the sample, and the incidence angle of the X-ray beam was set to a range of 0.12°, which was close to the critical angle of the samples. The patterns were recorded with a 2D charge-coupled device detector (SX165; Rayonix); the X-ray irradiation time ranged from 30 to 60 s according to the saturation level of the detector. Diffraction angles were calibrated using precalibrated sucrose (monoclinic, $P2_1$, a = 10.8631 Å, b = 8.7044 Å, c = 7.7624 Å, β = 102.938°) and the sample-to-detector distance was ~220.8 mm.

4.4.4. Device Fabrication

Indium–tin oxide (ITO)-coated glass substrates were sequentially sonicated in water with 1% (v/v) detergent, deionized water, acetone, and isopropyl alcohol for 15 min per step. The ZnO layer was prepared by spin-coating a diethyl zinc solution (obtained by mixing 15 wt% diethyl zinc in toluene with tetrahydrofuran at a ratio of 1:2) on the precleaned ITO substrate, then baking at 110°C for 10 min. Subsequently, the optimized CP-sensitive layer was prepared by spin-coating a PCPDTTBTT:chiral dopants:$PC_{70}BM$ blended solution (30 mg mL^{-1} PCPDTTBTT in toluene) at 300–2,000 rpm to obtain the desired film thickness. The prepared films were annealed at 250°C for 5 min to induce strong chiroptical activity. MoO_3 (4 nm)/Au (20 nm) electrodes were continuously thermally evaporated through a shadow mask in a high-vacuum chamber (< 5.0×10^{-6} Torr) at a rate of 0.1 Å s^{-1}. Passive matrix arrays were fabricated via the method described above using patterned ITO-coated glass.

4.4.5. Optoelectrical Measurements

The current–voltage (*I–V*) characteristics of the organic photodiodes were measured inside a vacuum chamber (< 5.0×10^{-5} Torr) using a Keithley 4200-SCS semiconductor parametric analyzer. Circularly polarized illumination was created by passing the beam through a linear polarizer and a quarter-wave plate (Thorlabs), which were installed between the light source and samples. DoCP was estimated using Stokes vector elements as follows:

$$\mathrm{DoCP} = \frac{2E_{0,x}E_{0,y}}{{E_{0,x}}^2+{E_{0,y}}^2}\sin\delta.$$

where $E_{0,x}$ and $E_{0,x}$ are the respective amplitudes of the *x* and *y* fields, and δ is the phase difference between the two orthogonal components of the light wave. To validate the direct measurement of spin information (i.e., DoCP measurements), the photoresponse was measured while rotating the retarder angle (θ) by 5°. The overall

photocurrent, I_{PC}, involving both circular and linear polarizations as a function of retarder rotation angle, was described by the following expression:

$$I_{PC} = Csin(2\theta + \varphi_c) + Lsin(4\theta + \varphi_l) + D$$

where θ is the rotation angle of the retarder, C is the amplitude of the CP light, φ_c is the phase of the CP light, L is the amplitude of the linearly polarized light, φ_l is the phase of the linearly polarized light, and D is a polarization-independent constant background response.

4.4.6. Mueller Matrix Spectroscopic Ellipsometry

In the Mueller–Stokes description, the light–sample interaction is described by a linear relationship between the Stokes vectors of incident (S_i) and outgoing (S_o) light through a 4 × 4 Mueller matrix (M) that implies the following sample characteristics:

$$\begin{bmatrix} s_0 \\ s_1' \\ s_2' \\ s_3' \end{bmatrix}_{out} = \begin{bmatrix} M_{11} & M_{12} & M_{13} & M_{14} \\ M_{21} & M_{22} & M_{23} & M_{24} \\ M_{31} & M_{32} & M_{33} & M_{34} \\ M_{41} & M_{42} & M_{43} & M_{44} \end{bmatrix} \begin{bmatrix} s_0 \\ s_1 \\ s_2 \\ s_3 \end{bmatrix}_{in}$$

To analyze the optical properties, the Mueller matrix must be reduced to its basic six optical properties. This is accomplished via matrix logarithm:

$$m = -\ln(M)$$

$$m = \begin{bmatrix} \alpha & \beta & \gamma & \xi \\ \beta & \alpha & \mu & \nu \\ \gamma & -\mu & \alpha & \eta \\ \xi & -\nu & -\eta & \alpha \end{bmatrix}$$

where α is the isotropic absorption; β, γ, and ξ are the linear dichroism at 0°/90°, linear dichroism at 45°/135°, and circular dichroism, respectively; and η, ν, and μ are the linear birefringence at 0°/90°, linear birefringence at 45°/135°, and circular birefringence, respectively[64].

I mainly investigated the Mueller matrix elements of m_{14}/m_{41} to quantify CD of the films comparing it for transmission and reflection modes. In the transmission

mode, the CD spectra inferred from M_{14} and M_{41} exhibited signals similar to the signals observed in conventional CD measurements. Conversely, in the reflection mode, the CD components were almost negligible at all oblique incidences.

All normalized Mueller matrix elements were measured using a dual rotating compensator ellipsometer (RC2; J. A. Woollam) in the wavelength range of 193–1,690 nm. Measurements were collected at various incidence angles (5° intervals) ranging from −20° to 75° for transmission mode and from 20° to 75° for reflection mode.

4.4.7. Selective CP Detection in Arrays.

A 30 × 30 array of photodiodes was irradiated with a CP beam of opposite handedness. Circularly polarized beams with opposite polarization helicities were alternately irradiated at the oblique incident angle of 10° and normal incident angle. Mode 1 was defined as the irradiation of the first pattern with LCP and the second pattern with RCP, while Mode 2 was defined as the irradiation of the second pattern with LCP and the first pattern with RCP. The corresponding M1 and M2 were defined as follows:

$$\mathrm{M1} = \frac{I_{light}}{I_{dark}} \quad at \;\; Mode \;\; 1$$

$$\mathrm{M2} = \frac{I_{light}}{I_{dark}} \quad at \;\; Mode \;\; 2$$

In the CP detection mode, $\mathrm{M1} - \mathrm{M2}$ was considered representative of distinguishing properties upon circular polarization handedness. However, in the conventional photodetection mode, assuming that the photodetectors could not distinguish LCP and RCP light, the mean photocurrent value, namely, $\frac{\mathrm{M1}+\mathrm{M2}}{2}$, was plotted and imaged.

4.4.8. Passive Matrix CP Real-Time Detection

Passive matrix-based devices, which consisted of two lined, gridded electrodes and the optimized chiral media, were driven by the passive matrix driving method using 5 V of input voltage with multiplexing in the grid structures. The analog-to-digital conversion (*ADC*) values were determined according to the resistance of our sensor device and external reference resistors in the signal addressing unit as follows:

$$ADC_{ij} = R_{ext}/(R_{ext} + R_{ij}) \cdot A$$

where ADC_{ij} is each pixel device of the matrix sensor, R_{ext} is the resistance of the external resistors, R_{ij} is the resistance of each pixel device, and A is a constant for signal addressing. When a pixel was illuminated by a CP beam, the resistance of the chiral active layers decreased compared with the reference resistors, leading to enhancement of the terminal conversion values. Optimization of the resistance and dissymmetric factors of the chiral media provided a three-state electrical readout as demonstrated in ternary quantum application experiments (final digital conversion value: 0 for the dark state, 1 for the LCP beam, and 2 for the RCP beam).

4.5. References

(1) Wiesner, S. Conjugate Coding. *ACM Sigact News* **1983,** *15*, 78-88.

(2) Bliokh, K. Y.; Rodríguez-Fortuño, F. J.; Nori, F.; Zayats, A. V. Spin–Orbit Interactions of Light. *Nat. Photon.* **2015,** *9*, 796-808.

(3) Lodahl, P.; Mahmoodian, S.; Stobbe, S.; Rauschenbeutel, A.; Schneeweiss, P.; Volz, J.; Pichler, H.; Zoller, P. Chiral Quantum Optics. *Nature* **2017,** *541*, 473-480.

(4) Li, W.; Coppens, Z. J.; Besteiro, L. V.; Wang, W.; Govorov, A. O.; Valentine, J. Circularly Polarized Light Detection with Hot Electrons in Chiral Plasmonic Metamaterials. *Nat. Commun.* **2015,** *6*, 8379.

(5) Ji, Z.; Liu, W.; Krylyuk, S.; Fan, X.; Zhang, Z.; Pan, A.; Feng, L.; Davydov, A.; Agarwal, R. Photocurrent Detection of the Orbital Angular Momentum of Light. *Science* **2020,** *368*, 763-767.

(6) Li, L.; Wang, J.; Kang, L.; Liu, W.; Yu, L.; Zheng, B.; Brongersma, M. L.; Werner, D. H.; Lan, S.; Shi, Y.; Xu, Y.; Wang, X. Monolithic Full-Stokes near-Infrared Polarimetry with Chiral Plasmonic Metasurface Integrated Graphene–Silicon Photodetector. *ACS Nano* **2020,** *14*, 16634-16642.

(7) Grey, P.; Fernandes, S. N.; Gaspar, D.; Fortunato, E.; Martins, R.; Godinho, M. H.; Pereira, L. Field-Effect Transistors on Photonic Cellulose Nanocrystal Solid Electrolyte for Circular Polarized Light Sensing. *Adv. Funct. Mater.* **2019,** *29*, 1805279.

(8) Han, H.; Lee, Y. J.; Kyhm, J.; Jeong, J. S.; Han, J.-H.; Yang, M. K.; Lee, K. M.; Choi, Y.; Yoon, T.-H.; Ju, H.; Ahn, S.-k.; Lim, J. A. High-Performance Circularly Polarized Light-Sensing near-Infrared Organic Phototransistors for Optoelectronic Cryptographic Primitives. *Adv. Funct. Mater.* **2020,** *30*, 2006236.

(9) Shi, W.; Salerno, F.; Ward, M. D.; Santana-Bonilla, A.; Wade, J.; Hou, X.; Liu, T.; Dennis, T. J. S.; Campbell, A. J.; Jelfs, K. E.; Fuchter, M. J. Fullerene Desymmetrization as a Means to Achieve Single-Enantiomer Electron Acceptors with Maximized Chiroptical Responsiveness. *Adv. Mater.* **2021,** *33*, 2004115.

(10) Zhang, L.; Song, I.; Ahn, J.; Han, M.; Linares, M.; Surin, M.; Zhang, H.-J.; Oh, J. H.; Lin, J. Π-Extended Perylene Diimide Double-Heterohelicenes as Ambipolar Organic Semiconductors for Broadband Circularly Polarized Light Detection. *Nat. Commun.* **2021,** *12*, 142.

(11) Ishii, A.; Miyasaka, T. Direct Detection of Circular Polarized Light in Helical 1d Perovskite-Based Photodiode. *Sci. Adv.* **2020,** *6*, eabd3274.

(12) Chen, C.; Gao, L.; Gao, W.; Ge, C.; Du, X.; Li, Z.; Yang, Y.; Niu, G.; Tang, J. Circularly Polarized Light Detection Using Chiral Hybrid Perovskite. *Nat. Commun.* **2019,** *10*, 1927.

(13) Cai, J.; Zhang, W.; Xu, L.; Hao, C.; Ma, W.; Sun, M.; Wu, X.; Qin, X.; Colombari, F. M.; de Moura, A. F.; Xu, J.; Silva, M. C.; Carneiro-Neto, E. B.; Gomes, W. R.; Vallée, R. A. L.; Pereira, E. C.; Liu, X.; Xu, C.; Klajn, R.; Kotov, N. A.; Kuang, H. Polarization-Sensitive Optoionic Membranes from Chiral Plasmonic Nanoparticles. *Nat. Nanotechnol.* **2022,** *17*, 408-416.

(14) Berova, N.; Bari, L. D.; Pescitelli, G. Application of Electronic Circular Dichroism in Configurational and Conformational Analysis of Organic Compounds. *Chem. Soc. Rev.* **2007,** *36*, 914-931.

(15) Greenfield, J. L.; Wade, J.; Brandt, J. R.; Shi, X.; Penfold, T. J.; Fuchter, M. J. Pathways to Increase the Dissymmetry in the Interaction of Chiral Light and Chiral Molecules. *Chem. Sci.* **2021,** *12*, 8589-8602.

(16) Schippers, P. H.; Dekkers, H. P. J. M. Circular Polarization of Luminescence as a Probe for Intramolecular 1nπ* Energy Transfer in Meso-Diketones. *J. Am. Chem. Soc.* **1983,** *105*, 145-146.

(17) Wade, J.; Hilfiker, J. N.; Brandt, J. R.; Liirò-Peluso, L.; Wan, L.; Shi, X.; Salerno, F.; Ryan, S. T. J.; Schöche, S.; Arteaga, O.; Jávorfi, T.; Siligardi, G.; Wang, C.; Amabilino, D. B.; Beton, P. H.; Campbell, A. J.; Fuchter, M. J. Natural Optical Activity as the Origin of the Large Chiroptical Properties in Π-Conjugated Polymer Thin Films. *Nat. Commun.* **2020,** *11*, 6137.

(18) Ward, M. D.; Wade, J.; Shi, X.; Nelson, J.; Campbell, A. J.; Fuchter, M. J. Highly Selective High-Speed Circularly Polarized Photodiodes Based on Π-Conjugated Polymers. *Adv. Opt. Mater.* **2022,** *10*, 2101044.

(19) Xu, L.; Wang, C.; Li, Y.-X.; Xu, X.-H.; Zhou, L.; Liu, N.; Wu, Z.-Q. Crystallization-Driven Asymmetric Helical Assembly of Conjugated Block Copolymers and the Aggregation Induced White-Light Emission and Circularly Polarized Luminescence. *Angew. Chem. Int. Ed.* **2020,** *59*, 16675-16682.

(20) Kim, N. Y.; Kyhm, J.; Han, H.; Kim, S. J.; Ahn, J.; Hwang, D. K.; Jang, H. W.; Ju, B.-K.; Lim, J. A. Chiroptical-Conjugated Polymer/Chiral Small Molecule Hybrid Thin Films for Circularly Polarized Light-Detecting Heterojunction Devices. *Adv. Funct. Mater.* **2019,** *29*, 1808668.

(21) Maity, S.; Bedi, A.; Patil, S. Side-Chain Induced Chirality in Diketopyrrolopyrrole Based Polymers. *J. Polym. Sci.* **2021,** *59*, 3181-3188.

(22) Lee, D.-M.; Song, J.-W.; Lee, Y.-J.; Yu, C.-J.; Kim, J.-H. Control of Circularly Polarized Electroluminescence in Induced Twist Structure of Conjugate Polymer. *Adv. Mater.* **2017,** *29*, 1700907.

(23) Yang, Y.; da Costa, R. C.; Smilgies, D.-M.; Campbell, A. J.; Fuchter, M. J. Induction of Circularly Polarized Electroluminescence from an Achiral Light-Emitting Polymer Via a Chiral Small-Molecule Dopant. *Adv. Mater.* **2013,** *25*, 2624-2628.

(24) Di Nuzzo, D.; Kulkarni, C.; Zhao, B.; Smolinsky, E.; Tassinari, F.; Meskers, S. C. J.; Naaman, R.; Meijer, E. W.; Friend, R. H. High Circular Polarization of Electroluminescence Achieved Via Self-Assembly of a Light-Emitting Chiral Conjugated Polymer into Multidomain Cholesteric Films. *ACS Nano* **2017,** *11*, 12713-12722.

(25) Wan, L.; Wade, J.; Salerno, F.; Arteaga, O.; Laidlaw, B.; Wang, X.; Penfold, T.; Fuchter, M. J.; Campbell, A. J. Inverting the Handedness of Circularly Polarized

Luminescence from Light-Emitting Polymers Using Film Thickness. *ACS Nano* **2019,** *13*, 8099-8105.

(26) Xu, X.; Li, Y.; Peng, Q. Recent Advances toward Highly Efficient Tandem Organic Solar Cells. *Small Struct.* **2020,** *1*, 2000016.

(27) Huo, L.; Chen, H.-Y.; Hou, J.; Chen, T. L.; Yang, Y. Low Band Gap Dithieno[3,2-B:2′,3′-D]Silole-Containing Polymers, Synthesis, Characterization and Photovoltaic Application. *Chem. Commun.* **2009**, 5570-5572.

(28) Moulé, A. J.; Tsami, A.; Bünnagel, T. W.; Forster, M.; Kronenberg, N. M.; Scharber, M.; Koppe, M.; Morana, M.; Brabec, C. J.; Meerholz, K.; Scherf, U. Two Novel Cyclopentadithiophene-Based Alternating Copolymers as Potential Donor Components for High-Efficiency Bulk-Heterojunction-Type Solar Cells. *Chem. Mater.* **2008,** *20*, 4045-4050.

(29) Damas, G.; Marchiori, C. F. N.; Araujo, C. M. On the Design of Donor–Acceptor Conjugated Polymers for Photocatalytic Hydrogen Evolution Reaction: First-Principles Theory-Based Assessment. *J. Phys. Chem. C* **2018,** *122*, 26876-26888.

(30) Jespersen, K. G.; Beenken, W. J. D.; Zaushitsyn, Y.; Yartsev, A.; Andersson, M.; Pullerits, T.; Sundström, V. The Electronic States of Polyfluorene Copolymers with Alternating Donor-Acceptor Units. *J. Chem. Phys.* **2004,** *121*, 12613-12617.

(31) Geng, Y.; Trajkovska, A.; Culligan, S. W.; Ou, J. J.; Chen, H. M. P.; Katsis, D.; Chen, S. H. Origin of Strong Chiroptical Activities in Films of Nonafluorenes with a Varying Extent of Pendant Chirality. *J. Am. Chem. Soc.* **2003,** *125*, 14032-14038.

(32) San Jose, B. A.; Matsushita, S.; Akagi, K. Lyotropic Chiral Nematic Liquid Crystalline Aliphatic Conjugated Polymers Based on Disubstituted Polyacetylene Derivatives That Exhibit High Dissymmetry Factors in Circularly Polarized Luminescence. *J. Am. Chem. Soc.* **2012,** *134*, 19795-19807.

(33) Lu, J.; Xue, Y.; Bernardino, K.; Zhang, N.-N.; Gomes, W. R.; Ramesar, N. S.; Liu, S.; Hu, Z.; Sun, T.; de Moura, A. F.; Kotov, N. A.; Liu, K. Enhanced Optical

Asymmetry in Supramolecular Chiroplasmonic Assemblies with Long-Range Order. *Science* **2021,** *371*, 1368-1374.

(34) Basel, B. S.; Hetzer, C.; Zirzlmeier, J.; Thiel, D.; Guldi, R.; Hampel, F.; Kahnt, A.; Clark, T.; Guldi, D. M.; Tykwinski, R. R. Davydov Splitting and Singlet Fission in Excitonically Coupled Pentacene Dimers. *Chem. Sci.* **2019,** *10*, 3854-3863.

(35) Castro-Fernández, S.; Peña-Gallego, Á.; Mosquera, R. A.; Alonso-Gómez, J. L. Chiroptical Symmetry Analysis: Exciton Chirality-Based Formulae to Understand the Chiroptical Responses of Cn and Dn Symmetric Systems. *Molecules* **2019,** *24*, 141.

(36) Kettle, J.; Waters, H.; Ding, Z.; Horie, M.; Smith, G. C. Chemical Changes in Pcpdtbt:Pcbm Solar Cells Using Xps and Tof-Sims and Use of Inverted Device Structure for Improving Lifetime Performance. *Sol. Energy Mater. Sol. Cells* **2015,** *141*, 139-147.

(37) Seo, H. O.; Jeong, M.-G.; Kim, K.-D.; Kim, D. H.; Kim, Y. D.; Lim, D. C. Studies of Degradation Behaviors of Poly (3-Hexylthiophene) Layers by X-Ray Photoelectron Spectroscopy. *Surf. Interface Anal.* **2014,** *46*, 544-549.

(38) Gilot, J.; Abbel, R.; Lakhwani, G.; Meijer, E. W.; Schenning, A. P. H. J.; Meskers, S. C. J. Polymer Photovoltaic Cells Sensitive to the Circular Polarization of Light. *Adv. Mater.* **2010,** *22*, E131-E134.

(39) Yang, Y.; da Costa, R. C.; Fuchter, M. J.; Campbell, A. J. Circularly Polarized Light Detection by a Chiral Organic Semiconductor Transistor. *Nat. Photon.* **2013,** *7*, 634-638.

(40) Lee, S. H.; Singh, D. P.; Sung, J. H.; Jo, M.-H.; Kwon, K. C.; Kim, S. Y.; Jang, H. W.; Kim, J. K. Highly Photoresponsive and Wavelength-Selective Circularly-Polarized-Light Detector Based on Metal-Oxides Hetero-Chiral Thin Film. *Sci. Rep.* **2016,** *6*, 19580.

(41) Shang, X.; Song, I.; Ohtsu, H.; Lee, Y. H.; Zhao, T.; Kojima, T.; Jung, J. H.; Kawano, M.; Oh, J. H. Supramolecular Nanostructures of Chiral Perylene Diimides

with Amplified Chirality for High-Performance Chiroptical Sensing. *Adv. Mater.* **2017,** *29*, 1605828.

(42) Schulz, M.; Balzer, F.; Scheunemann, D.; Arteaga, O.; Lützen, A.; Meskers, S. C. J.; Schiek, M. Chiral Excitonic Organic Photodiodes for Direct Detection of Circular Polarized Light. *Adv. Funct. Mater.* **2019,** *29*, 1900684.

(43) Peng, J.; Cumming, B. P.; Gu, M. Direct Detection of Photon Spin Angular Momentum by a Chiral Graphene Mid-Infrared Photodetector. *Opt. Lett.* **2019,** *44*, 2998-3001.

(44) Ma, J.; Fang, C.; Chen, C.; Jin, L.; Wang, J.; Wang, S.; Tang, J.; Li, D. Chiral 2d Perovskites with a High Degree of Circularly Polarized Photoluminescence. *ACS Nano* **2019,** *13*, 3659-3665.

(45) Wang, L.; Xue, Y.; Cui, M.; Huang, Y.; Xu, H.; Qin, C.; Yang, J.; Dai, H.; Yuan, M. A Chiral Reduced-Dimension Perovskite for an Efficient Flexible Circularly Polarized Light Photodetector. *Angew. Chem. Int. Ed.* **2020,** *59*, 6442-6450.

(46) Cheng, J.; Ge, F.; Zhang, C.; Kuai, Y.; Hou, P.; Xiang, Y.; Zhang, D.; Qiu, L.; Zhang, Q.; Zou, G. Enabling Discrimination Capability in an Achiral F6bt-Based Organic Semiconductor Transistor Via Circularly Polarized Light Induction. *J. Mater. Chem. C* **2020,** *8*, 9271-9275.

(47) Shang, X.; Song, I.; Lee, J. H.; Choi, W.; Ahn, J.; Ohtsu, H.; Kim, J. C.; Koo, J. Y.; Kwak, S. K.; Oh, J. H. Surface-Doped Quasi-2d Chiral Organic Single Crystals for Chiroptical Sensing. *ACS Nano* **2020,** *14*, 14146-14156.

(48) Hao, J.; Lu, H.; Mao, L.; Chen, X.; Beard, M. C.; Blackburn, J. L. Direct Detection of Circularly Polarized Light Using Chiral Copper Chloride–Carbon Nanotube Heterostructures. *ACS Nano* **2021,** *15*, 7608-7617.

(49) Li, D.; Liu, X.; Wu, W.; Peng, Y.; Zhao, S.; Li, L.; Hong, M.; Luo, J. Chiral Lead-Free Hybrid Perovskites for Self-Powered Circularly Polarized Light Detection. *Angew. Chem. Int. Ed.* **2021,** *60*, 8415-8418.

(50) Liu, L.; Yang, Y.; Wang, Y.; Adil, M. A.; Zhao, Y.; Zhang, J.; Chen, K.; Deng, D.; Zhang, H.; Amin, K.; Wu, Y.; Zhang, Y.; Wei, Z. Building Supramolecular Chirality in Bulk Heterojunctions Enables Amplified Dissymmetry Current for High-Performing Circularly Polarized Light Detection. *ACS Mater. Lett.* **2022,** *4*, 401-409.

(51) Kim, H.; Kim, R. M.; Namgung, S. D.; Cho, N. H.; Son, J. B.; Bang, K.; Choi, M.; Kim, S. K.; Nam, K. T.; Lee, J. W.; Oh, J. H. Ultrasensitive near-Infrared Circularly Polarized Light Detection Using 3d Perovskite Embedded with Chiral Plasmonic Nanoparticles. *Adv. Sci.* **2022,** *9*, 2104598.

(52) Stolterfoht, M.; Armin, A.; Philippa, B.; White, R. D.; Burn, P. L.; Meredith, P.; Juška, G.; Pivrikas, A. Photocarrier Drift Distance in Organic Solar Cells and Photodetectors. *Sci. Rep.* **2015,** *5*, 9949.

(53) Armin, A.; Chen, Z.; Jin, Y.; Zhang, K.; Huang, F.; Shoaee, S. A Shockley-Type Polymer: Fullerene Solar Cell. *Adv. Energy Mater.* **2018,** *8*, 1701450.

(54) Zhao, Q.; Jie, W.; Wang, T.; Castellanos-Gomez, A.; Frisenda, R. Inse Schottky Diodes Based on Van Der Waals Contacts. *Adv. Funct. Mater.* **2020,** *30*, 2001307.

(55) Zhang, J.; Xi, N.; Chen, H.; Lai, K. W. C.; Li, G.; Wejinya, U. Photovoltaic Effect in Single Carbon Nanotube-Based Schottky Diodes. *Int. J. Nanopart.* **2008,** *1*, 108-118.

(56) Periyanagounder, D.; Gnanasekar, P.; Varadhan, P.; He, J.-H.; Kulandaivel, J. High Performance, Self-Powered Photodetectors Based on a Graphene/Silicon Schottky Junction Diode. *J. Mater. Chem. C* **2018,** *6*, 9545-9551.

(57) Kim, J.; Joo, S. S.; Lee, K. W.; Kim, J. H.; Shin, D. H.; Kim, S.; Choi, S.-H. Near-Ultraviolet-Sensitive Graphene/Porous Silicon Photodetectors. *ACS Appl. Mater. Interfaces* **2014,** *6*, 20880-20886.

(58) Buscema, M.; Island, J. O.; Groenendijk, D. J.; Blanter, S. I.; Steele, G. A.; van der Zant, H. S. J.; Castellanos-Gomez, A. Photocurrent Generation with Two-Dimensional Van Der Waals Semiconductors. *Chem. Soc. Rev.* **2015,** *44*, 3691-3718.

(59) Zhao, Q.; Wang, W.; Carrascoso-Plana, F.; Jie, W.; Wang, T.; Castellanos-Gomez, A.; Frisenda, R. The Role of Traps in the Photocurrent Generation Mechanism in Thin Inse Photodetectors. *Mater. Horiz.* **2020,** *7*, 252-262.

(60) Müller, C.; Bergqvist, J.; Vandewal, K.; Tvingstedt, K.; Anselmo, A. S.; Magnusson, R.; Alonso, M. I.; Moons, E.; Arwin, H.; Campoy-Quiles, M.; Inganäs, O. Phase Behaviour of Liquid-Crystalline Polymer/Fullerene Organic Photovoltaic Blends: Thermal Stability and Miscibility. *J. Mater. Chem.* **2011,** *21*, 10676-10684.

(61) Miao, J.; Zhang, F. Recent Progress on Photomultiplication Type Organic Photodetectors. *Laser Photonics Rev.* **2019,** *13*, 1800204.

(62) Snatzke, G. Circular Dichroism and Absolute Conformation: Application of Qualitative Mo Theory to Chiroptical Phenomena. *Angew. Chem. Int. Ed. Engl.* **1979,** *18*, 363-377.

(63) Arteaga, O. Natural Optical Activity Vs Circular Bragg Reflection Studied by Mueller Matrix Ellipsometry. *Thin Solid Films* **2016,** *617*, 14-19.

(64) Azzam, R. M. A. Propagation of Partially Polarized Light through Anisotropic Media with or without Depolarization: A Differential 4 × 4 Matrix Calculus. *J. Opt. Soc. Am.* **1978,** *68*, 1756-1767.

요 약 문

키랄성은 대상의 거울상과 겹쳐질 수 없는 비대칭성을 의미하는 것으로, 자연과 생명체를 구성하는 요소들의 보편적인 특성이다. 원편광은 전자기파의 벡터의 회전 방향에 따른 키랄성을 지니고 있으며, 3 차원 디스플레이, 편광 이미징, 암호화된 광통신, 양자 계산 등에 다양한 활용이 가능하기에 학술적인 측면과 산업적 측면 모두에서 큰 관심을 받아왔다. 이러한 원편광을 발광, 혹은 감지하기 위해서 기존에는 선편광판, 위상지연판 등의 여러 광학 기구들을 이용하였으나 이는 장치의 성능을 감소시키고, 소형화 및 공정 간소화 면에서 큰 제약을 지니고 있다. 이 때문에 직접적인 키랄성의 부여가 가능하며, 조절성, 경량성, 공정 용이성, 유연성 등을 장점으로 하는 유기물을 활용하여 원편광을 직접 감지할 수 있는 소자에 관한 연구들이 진행되고 있다. 그러나 유기물 기반 키랄 광전자 소자에 대한 연구는 아직까지 초기 단계로, 현재까지 보고된 연구들은 대부분 낮은 성능으로 인해 상용화에 어려움을 겪고 있다. 초분자 키랄성은 분자수준을 넘어서는 키랄성의 범위를 나타내며 분자간의 자가 조립 혹은 정렬을 통해 대부분 분자수준 대비 증폭된 키랄성을 보인다. 이에 앞선 문제를 해결하기 위하여 이 논문에서는 유기 반도체의 초분자 키랄성에 대한 연구 및 그의 광전자적 응용에 관한 연구에 중점을 두고있다.

1 장에서는 유기 전자 소자, 초분자 키랄성 및 키랄 광전자에 대한 기본 정보를 포함한 연구 배경과 본 논문의 목적을 간략히 소개하였다.

2 장에서는 신규 베이 위치가 치환된 키랄성 페릴렌 다이이미드를 개발하고, 용액 공정을 통해 자가 조립을 유도하여 일 차원 나노 와이어 구조체를 제조하였다. 제조된 나노 와이어 구조체들의 원형 이색성

스펙트럼 분석을 통해, 베이 위치의 치환이 초분자 키랄성의 조절에 효과적임을 확인하였다. 또한 나노 와이어를 기반으로 한 전계 효과 트랜지스터 구조의 광 감지기를 제작하여 베이 위치 치환 효과에 따른 광전자 소자의 성능을 조사하였다. 이 때, 사이아노기가 치환된 나노 구조체 기반 소자가 가장 우수한 성능을 나타내었고, 결정 구조 분석과 이를 바탕으로 한 이론적 계산을 통해 사이아노기 치환에 따른 전하 주입성 및 파이 겹침 면적의 향상이 우수한 성능의 요인임을 확인하였다.

3 장에서는 신규 키랄성 페릴렌 다이이미드와 절연 고분자 폴리락타이드를 혼합하여 유기 전계효과 트랜지스터 기반 광 감지기의 활성층으로 활용하였다. 이 때, 키랄성 페릴렌 다이이미드 만이 사용된 박막에 비해 고분자가 혼합된 박막에서 증폭된 초분자 키랄성이 나타나는 것을 확인하였다. 또한 제작된 혼합물 박막 기반 광 감지기 소자에서 키랄성 페릴렌 다이이미드와 폴리락타이드 간의 혼합 비율에 따른 광 전자소자의 성능을 비교하여 폴리락타이드의 혼합으로 유도한 전하 트랩 효과가 소자의 유의미한 광 감지 성능 향상을 이끌어냈음을 확인하였다. 또한, 키랄성 페릴렌 다이이미드에서 반대 방향 키랄성 분자를 절반씩 혼합하여 라세미체로 활용한 경우와, 순수 거울상 이성질체를 활용한 경우에서의 광전자 소자 성능 비교를 통해, 키랄성이 광전자 소자에 미치는 영향 및 그 원인을 분석하였다.

4 장에서는 앞선 연구를 바탕으로 하여 키랄성 도펀트와 유기 반도체 고분자를 혼합하고 정렬을 유도하여 증폭된 키랄성을 갖는 활성층을 제작하였고, 이 때의 키랄성 증폭 원리를 연구하였다. 활성층의 구조, 형태, 조성, 작용기의 분석을 통해 제작된 활성층은 키랄성 도펀트로 인해 열처리 과정에서 초분자 나선 구조체를 이루고, 도펀트는 해당 작용 이후 승화되어 사라지며, 이로 인해 형성된 나선 구조체

발색단에서의 엑시톤 커플링이 발생하는 것으로 키랄성의 증폭 원리를 제시하였다. 또한 제작된 활성층을 바탕으로 다이오드 기반 광 감지 소자를 제작하였고, 소자 구조의 최적화 및 메커니즘 연구를 통해 약 1.2 에 달하는 우수한 g factor 수치와 함께 높은 광전자적 특성을 보고하였다. 이밖에도 활성층의 광학 활성들을 분석하여 개발된 광 감지기가 선형 편광의 축 방향 및 입사 각도에 영향을 받지 않으며, 이에 따라 원형 편광의 정도의 세밀한 탐지가 가능함을 확인하였다. 최종적으로는 어레이 소자로 활용하여 보안 및 전송 속도가 강화된 광통신 및 이미징에 활용이 가능함을 보고하였다.

주요어: 반도체, 유기 전자 소자, 초분자 키랄성, 원편광, 광 감지기

학 번: 2019-30718

Acknowledgements

감사의 글

돌이켜보면 시간이 참 빠른 것 같습니다. 2017 년에 연구실에 처음 들어왔을 때가 불과 얼마 전 같은데, 어느덧 시간이 흘러 2023 년 박사과정을 마치고 졸업 논문을 제출하게 되었습니다. 그동안의 학위과정이 제게는 소중한 사람들을 만나고 생활하면서 많은 것을 경험하고 배울 수 있었던 정말 뜻 깊은 시간이었습니다. 그렇기에 학위과정을 마치면서, 그동안 도움 주셨던 분들께 감사의 글을 남기고자 합니다.

가장 먼저 학위 과정 동안 아낌없는 열정으로 저를 지도해주신 오준학 교수님께 진심으로 감사드립니다. 여전히 부족한 점이 많지만, 교수님의 훌륭한 지도 덕분에 지금까지 발전해올 수 있었습니다. 그동안 교수님께서 해주셨던 많은 조언들을 마음에 새기고, 앞으로도 교수님의 자랑스러운 제자가 될 수 있도록 정진하겠습니다. 또한 바쁘신 와중에도 박사 학위 심사위원으로 자리해 주시어 귀중한 조언들을 해주신 이종찬 교수님, 유동원 교수님, 김소연 교수님, 그리고 박종혁 박사님께도 정말 감사드립니다.

다음으로 항상 제 편이 되어 주시는 부모님께 감사드립니다. 부모님의 응원과 지지 덕분에 길다면 긴 학위과정을 문제없이 잘 마칠 수 있었습니다. 이렇게 부모님의 품에서 벗어나 한 걸음씩 성장해 나가는 것이 부모님과 점점 멀어지는 것 같아 때로는 아쉽기도, 두렵기도 합니다. 그럼에도 표현이 서툴러 항상 마음 속에만 지니고 이를 나타내지를 못했던 것 같습니다. 엄마, 아빠, 항상 사랑합니다.

그동안 동고동락해온 연구실 멤버들께도 감사드립니다. 먼저 연구실을 떠나 각자의 자리에서 열심히 활동중인 은광이 형, 문정 누나, 무열이 형, 윤호 형, 오영이 형, 철희 형, 해랑 누나, 윤기 형, 홍기 형, 상진이 형, 종현이 형, 재환, 아영, 슬기, 한빛, 명근, 종민, 정훈이 모두 자랑스럽습니다. 함께 했던 시간들은 정말 좋은 추억으로 제게 남아있습니다. 많이 부족했던 저를 잘 챙겨주셔서 고맙습니다.

그동안 저와 함께 연구를 진행해온 인호 형, 샤보 박사님, 상혁이, 태수 에게도 감사를 전합니다. 연구에 관해 문외한이던 제게 처음부터 끝까지 많은 것을 알려주신 인호 형, 형으로부터 정말 많은 것을 배웠고, 덕분에 함께 좋은 연구를 할 수 있었습니다. 감사합니다. 앞으로도 동료 연구자로서 서로에게 도움이 되는 사이가 되면 좋겠습니다. 내가 배웠던 것들을 후배들에게 잘 전해주고 싶었는데, 마음먹은대로 되질 않았던 것 같습니다. 그럼에도 묵묵히 나를 도와 연구했던 상혁, 태수에게 고마운 마음을 전합니다. 상혁이는 앞으로도 함께 연구들을 잘 마무리 해보면 좋을 것 같습니다. 태수에게는 외국에 나가 있느라 사수로서 많은 도움이 되지 못한 것 같아 항상 미안하고, 그럼에도 적극적으로 잘 도와주어서 정말 고맙습니다.

랩장을 맡아 지난 2 년간 고생한 도영이, 앞으로 고생할 문기 형, 그리고 연구실 내에 애매한 문제가 있을 때마다 중심을 잡아주었던 현규 형, 유상이 형 덕분에 연구실이 보다 지내기 즐거운 곳이 되었던 것 같습니다. 좋은 방향으로 연구실을 이끌어 주셔서 정말 고맙습니다. 멀리서 연구를 위해 연구실에 오신 퐁팍 박사님과, 항상 열심히 하는 현우를 볼 때마다 연구에 대한 열정을 되새길 수 있었습니다. 고맙습니다. 노력한 만큼 좋은 결실을 이루면 좋겠습니다. 이제 연구실의 주축이 될 하영이, 현욱이, 원빈이 덕분에 연구실 생활이

즐거웠습니다. 앞으로도 지금처럼 동기들끼리 서로 도와가며 잘 헤쳐 나가면 좋겠습니다. 저를 이어서 연구실 업적 정리를 하게 된 민성이는 일이 있을 때마다 싫은 내색 한번 안하고 열심히 도와주어서 항상 고마웠습니다. 그리고 해니 누나와 예진이, 보성이, 보람이 상욱이는 짧은 기간에 벌써 본인들 각자의 연구방향을 잡고, 잘 해나가고 있는 것 같아 대단하다고 생각합니다. 이번에 연구실에 들어온 민상이, 호리, 종현이도 연구실 생활 잘 적응하고, 다들 본인들이 바라는 바를 이뤘으면 좋겠습니다. 되짚어보니 정말 많은 멤버들이 한 연구실의 구성원으로 만나 좋은 관계를 이룬 것 같습니다. 다들 각자의 자리에서 원하는 목표를 이루고, 같은 연구실 출신으로 계속 이러한 인연이 이어졌으면 좋겠습니다.

방문 학생이었던 저를 성심성의로 지도 해주셨던 이대연 교수님과, 타국에서 잘 적응할 수 있도록 도움주신 재현이 형, 민철이 형, 민준이 형, 혜중 누나, 소현이에게도 감사의 마음을 전합니다. 덕분에 새로운 경험들을 하면서 많은 것을 배울 수 있었습니다.

그동안의 학위과정동안 배운 것을 바탕으로 인생에서의 새로운 도전을 잘 시작할 수 있도록 노력하겠습니다. 마지막으로 이 논문을 작성하고 완성하는 데 도움을 주신 모든 분들께 다시 한번 감사의 마음을 전합니다. 감사합니다.